Convective motions in the scrape-off layer of magnetically confined plasmas

Fryderyk Wilczyński

Submitted in accordance with the requirements for the degree of

Doctor of Philosophy

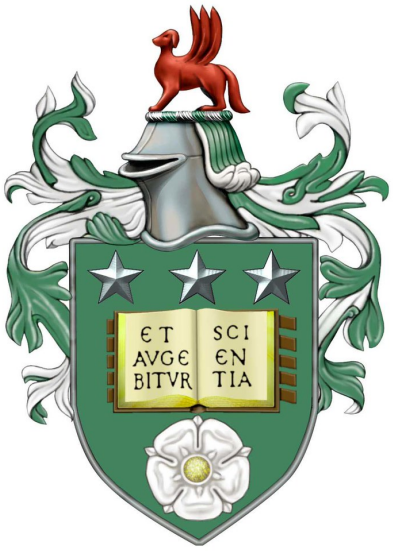

University of Leeds

Centre for Doctoral Training in Fluid Dynamics

September 2019

To my parents

Intellectual Property Statement

The candidate confirms that the work submitted is their own, except where work which has formed part of jointly authored publications has been included. The contribution of the candidate and the other authors to this work has been explicitly indicated below. The candidate confirms that appropriate credit has been given within the thesis where reference has been made to the work of others.

Chapter 3 contains material from the jointly authored publication:

Wilczynski, F., Hughes, D. W., Van Loo, S., Arter, W., and Militello, F. (2019). Stability of scrape-off layer plasma: A modified Rayleigh–Bénard problem. *Physics of Plasmas*, 26(2):022510

Chapter 4 contains material from the jointly authored publication:

Wilczynski, F. and Hughes, D. W. (2019). Stability of two-layer miscible convection. *Physical Review Fluids*, 4(10):103502

The co-authors provided ideas and guidance surrounding this work and aided with the writing of the paper. All mathematical and scientific research contained in this work was undertaken by the candidate himself.

Acknowledgements

First and foremost, I want to thank David Hughes, a charismatic and inspiring supervisor, for his guidance, insight, patience and encouragement throughout the duration of my doctorate studies. I thank Sven Van Loo for valuable discussions and helpful advice. I would like to extend my gratitude to the Culham Centre for Fusion Energy for partially funding this project, and to Wayne Arter and Fulvio Militello for introducing me to the world of fusion plasma physics.

I am grateful to the EPSRC Centre for Doctoral Training for affording me the opportunity to study here, and to my peers for creating a stimulating environment to work in and for their support along the way to the thesis.

It has been a privilege to be a student at the University of Leeds, a place with a great culture of fluid dynamics research. I want to acknowledge the Astrophysical and Geophysical Fluid Dynamics group and the Fluids and MHD seminars for exposing me to the vastness of the field, and for broadening my interests and understanding of fluid dynamics.

Thank you Caitlin, for your love and kindness, for being by my side through times good and bad.

Finally, I want to thank my parents, Beata and Rafał, for the sacrifices they have made to provide with opportunities, and for their unwavering support of my academic pursuit.

This work was supported by the Engineering and Physical Sciences Research Council (EPSRC) Centre for Doctoral Training in Fluid Dynamics at the University of Leeds under Grant No. EP/L01615X/1.

Abstract

Magnetic confinement devices utilize magnetic fields to confine hot plasma with the aim of generating thermonuclear fusion. At the plasma edge, in the so-called scrape-off layer (SOL), turbulent motions are responsible for transporting plasma from the core confinement region towards the material surfaces. It has been universally observed that SOL turbulence is characterised by large, intermittent fluctuations, often called filaments or blobs, which dominate the particle transport and enhance the plasma interaction with the surrounding material boundaries. This is problematic as plasma-wall interaction can potentially damage plasma-facing components and shorten the life-time of the device. A full understanding of filament dynamics is therefore essential for the successful operation of future fusion experiments and reactors.

The dominant mechanism behind the generation of turbulent motions at the plasma edge is thought to be the interchange instability, due to pressure gradients and magnetic field curvature. In this thesis we study a two-dimensional interchange model based on the Braginskii fluid equations, in an effort to shed light on the fundamental properties of the onset of instability. We study interchange dynamics in two different settings: first, we restrict our attention solely to the dynamics in the SOL; next, we extend our considerations to the coupled interaction between the core plasma and the SOL. In both cases we characterise the onset of instability and perform an extensive analysis to describe how the behaviour of the system varies as a function of plasma parameters.

Contents

List of Figures

List of Tables

Chapter 1

Introduction

Chen (1984) defines plasma as a quasineutral gas of charged and neutral particles that exhibits collective behaviour. In a plasma state, gases have so much energy that electrons are freed from their atomic nuclei. The resulting mixture of atomic ions and free electrons in a plasma is a good conductor of electricity and reacts strongly to electric and magnetic fields. Much of the understanding of plasma behaviour has come from the pursuit of controlled thermonuclear fusion, for which plasma physics provides the scientific foundation. The thesis contained in this report is motivated by the observations of plasma instabilities inside nuclear fusion devices.

Nuclear fusion is a reaction in which two (or more) light atomic nuclei join to form a heavier nucleus (and by-products). In a nuclear fusion reaction, energy is released as a result of a difference in mass between products and reactants. A mass of any atomic nucleus is lower that the total mass of its constituent nucleons. This 'missing mass' is known as the mass defect and it represents the energy that was released when the nucleus was formed. The amount of energy released is known as the nuclear binding energy, and it is equal to the amount of energy required to separate the nucleus into its constituents. In a fusion reaction, the mass defect, and therefore the binding energy, of the resulting nucleus is greater than that of the reactants and the excess energy is released as the kinetic energy of the products. This kinetic energy can potentially be harnessed to produce usable energy output.

In order for a fusion reaction to occur the fuel species must collide together with sufficient kinetic energy to overcome the repelling forces and come close enough for the strong nuclear force to fuse the nuclei together. Current fusion experiments use Deuterium and Tritium (isotopes of hydrogen) as fuel materials. This combination of reactants has been selected to be most promising for the purposes of energy generation based on its high reactivity and energy yields, at sustainable temperatures (Hazeltine and Meiss, 2003). In a nuclear reaction, deuterium and tritium fuse to produce helium and high-speed neutrons, releasing 17.6 megaelectron volts of energy per reaction

$$\mathrm{D} + \mathrm{T} \longrightarrow \mathrm{He}^4 + \mathrm{n} + 17.6 \ \ \mathrm{MeV}. \tag{1.1}$$

The resulting neutron carries approximately 80% of the energy as kinetic energy. In fusion

reactors the energy carried by neutrons will be used to generate electricity. The neutrons will heat a blanket of denser material surrounding the fuel, and this heat will drive a steam turbine to generate electricity.

To achieve viable reaction rates, the D–T fuel needs to be heated to a temperature of the order of 100 million degrees Kelvin. At such high temperatures all atoms become ionised and the fuel exists in the plasma state. The key challenge in achieving thermonuclear fusion is confinement of the hot plasma. The extreme temperatures required prevent the use of any solid material containers to confine the fusion reactants: plasma has to be located in a vacuum. Additionally, high temperatures imply high pressures, which cause the plasma to expand, thus necessitating use of external forces to act against the plasma expansion. Magnetic confinement fusion exploits the electrically conducting nature of plasma and uses a strong magnetic field to confine the plasma to circulate perpetually within a ring shaped vessel.

In the presence of magnetic and electric fields, charged particles are subject to the Lorentz force

$$\boldsymbol{F} = q\left(\boldsymbol{E} + \boldsymbol{v} \times \boldsymbol{B}\right). \tag{1.2}$$

Plasma particles are allowed to move freely in the direction parallel to the magnetic field, but their motion perpendicular to $\boldsymbol{B}$ is restricted to movement on orbits about the magnetic field lines. The orbits' radii are inversely proportional to the strength of the magnetic field. Consequently, fusion plasma can be confined in a vacuum permeated by strong magnetic field with appropriate topology.

The structure of the confining magnetic field is governed by two theorems:

1. The Virial theorem, which, in the context of electromagnetic configurations, states that any finite configuration of magnetic fields and plasma will expand indefinitely if not confined by external forces. Therefore the confinement of plasma requires externally applied pressure via magnetic coils.

2. The "hairy ball" theorem states that there exists no non-vanishing continuous tangent vector field on the surface of a sphere. This means that all magnetic geometries topologically equivalent to a sphere possess at least one null point through which plasma would be able to escape confinement.

A geometry that is uninhibited by the hairy ball theorem and allows for magnetic field lines with no magnetic null points is a torus. For that reason, the majority of magnetic confinement devices utilise toroidal geometry, out of which the most mature and widely studied is the tokamak.

Figure 1.1 shows a pictorial representation of a tokamak device. A modern tokamak consists of a toroidally shaped vacuum vessel, around which magnetic coils are wound. These external coils generate the toroidal magnetic field in the tokamak. Purely toroidal field however is not enough to confine the particles. The effects of curvature and magnetic field gradients inside the torus cause the centres about which charged particles orbit to slowly drift across the magnetic field, hence escaping confinement. To remedy this problem an additional poloidal magnetic field component is induced via transformer action on the

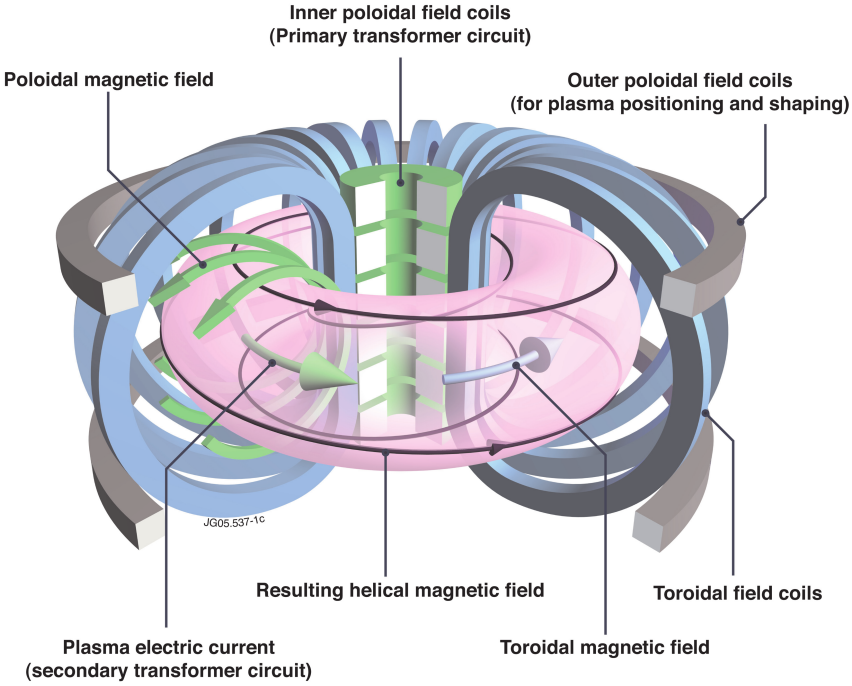

Figure 1.1: Schematic diagram of a tokamak showing the arrangement of magnetic coils and the resulting helical magnetic field, courtesy of EUROfusion (2011).

plasma itself. The primary winding of the transformer is provided by a solenoid placed in the middle of the device. Ramping up a current in the solenoid produces an increasing magnetic flux, which in turn drives the toroidal current in a plasma, which act as the secondary winding. This current then produces a poloidal magnetic field around the plasma. The resulting total magnetic field winds helically around the torus and forms closed surfaces, called "flux surfaces", on which the flux of poloidal magnetic field is constant. The surfaces form nested toroids in the vacuum vessel. Perfect confinement would be achieved if the plasma remained on these surfaces indefinitely.

In reality, various turbulent processes and plasma drifts move plasma from surface to surface, outwards towards the walls of the tokamak, despite the presence of the confining magnetic field. This drift, if uninterrupted, will eventually result in plasma impacting on the walls of the tokamak chamber, potentially damaging the device's components. To reduce the plasma–surface interaction, modern tokamaks utilise a configuration that produces a diverted plasma. The poloidal magnetic field is shaped to create distinct regions of plasma inside the tokamak — the core and the scrape-off layer (SOL) — and thus to divert the escaping plasma into a specifically designed structure known as the divertor (see Figure 1.2). The two regions are separated by a magnetic separatrix and are topologically distinct. In the core, the magnetic field lines close back upon themselves and do not come in contact with material surfaces. By contrast, the scrape-off layer is the region of open field lines situated between the separatrix and the vessel wall; the magnetic field lines are open in the sense that they penetrate a solid surface. The topological distinction between the core and SOL regions has profound consequences on plasma dynamics in the direction parallel to the magnetic field. Since every field line in the SOL is connected to a material

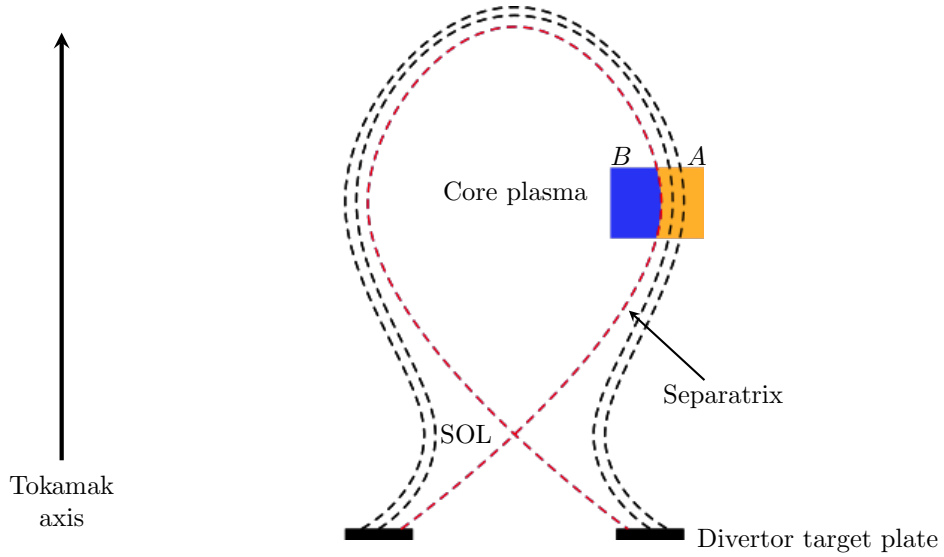

Figure 1.2: Schematic of the poloidal field configuration in a divertor tokamak.

surface, the SOL plasma is always subject to parallel losses of particles and energy.

The classical picture of edge plasma dynamics assumes that parallel transport processes are dominant in the SOL, whereas radial transport is weak and diffusive. As such, a plasma particle that drifts out of the core into the SOL is transported along the magnetic field and deposited onto the target surfaces before it reaches the chamber wall. This classical picture of edge plasma transport was reassessed when analysis of experimental data from Alcator C–Mod demonstrated that the majority of particles entering the SOL for the core plasma interacted with the main chamber walls rather than flow to the divertor plates (Umansky et al., 1998). This contradicted the assumption that parallel transport processes dominate over radial transport and challenged the view that radial transport is diffusive in nature. To overcome the fast parallel transport along field lines, the observed large radial flux to the main chamber wall would require an unphysically large effective diffusion coefficient. Furthermore to match the experimental data, this diffusion coefficient would have to be strongly increasing with radial position. These results changed the community's overall understanding of SOL transport, and seemed to suggest that radial plasma transport is more convective than diffusive. Indeed, further studies of edge plasma revealed that cross-field transport in the SOL is dominated by intermittent, radially outward motion of dense coherent plasma structures, often called filaments or blobs (D'Ippolito et al., 2011; Krasheninnikov et al., 2008). Figure 1.3 contains a series of images, obtained using high speed cameras, depicting an ejection of a single filament from the core plasma and its subsequent fast radial motion in the SOL. These filaments have been shown to contribute to around 50% of the total radial particle flux, in a number of different machines, and as such play a major part in transporting plasma and energy from the well-confined region towards the material surfaces.

One of the biggest challenges facing future generation magnetic confinement devices (such as ITER and DEMO) is the control of the high heat and particle fluxes onto the divertor and main chamber wall. These fluxes are determined by the balance between

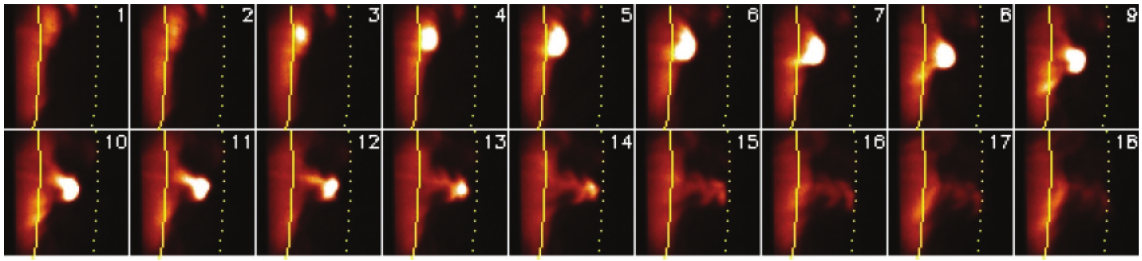

Figure 1.3: Filament ejection in NSTX, visualised through a Gas Puff Imaging diagnostic. Images show the outboard mid-plane region, with the yellow line representing the separatrix; the time between frames is 7.5μs. Figure taken from Maqueda et al. (2011).

transport across and parallel to the magnetic field in the scrape-off layer (SOL). Filaments enhance perpendicular transport, leading to a broader SOL and hence reduced loads to the divertor; at the same time, however, this results in larger fluxes to the main chamber wall. As discussed above, this is problematic, since plasma-wall interaction can potentially cause significant erosion and hence shorten the lifetime of the machine. Furthermore, large fluxes of plasma impinging on material walls can cause surface particles to become liberated from the material and enter the core of the plasma as impurities. Once there, they radiate energy, thus reducing the temperature of the plasma and the performance of the tokamak. A full understanding of filament dynamics is therefore essential for the successful operation of future fusion experiments and reactors.

Over the last two decades, significant experimental and theoretical work has been devoted to understanding the fundamental mechanisms governing the dynamics in the scrape-off layer of magnetic fusion devices. An extensive body of experimental studies of edge plasma turbulence has shown that filaments are an almost ubiquitous phenomena in the edge of plasmas across magnetic confinement devices with regions of open field lines (D'Ippolito et al., 2011). Their presence is reflected by the strong intermittency in edge plasma measurements. In particular, measurements of plasma density in the SOL are characterized by irregular large amplitude bursts with a peak value significantly higher than the surrounding root mean square fluctuations of the background plasma. Furthermore, the bursts in the density signal recorded by probes at different radial locations in the SOL are correlated in a way that indicates radial outward motion of high density plasma structures. This intermittent nature of fluctuations is usually characterized by constructing a probability density function (PDF) of probe signals. Figure 1.4 shows PDFs of ion saturation current measurements taken on four different devices (Antar et al., 2003). A universal feature of the turbulent fluctuations, among magnetically confined plasmas, is positive skewness of PDFs, reflecting the dominance of positive fluctuations in the SOL.

Optical imaging measurements indicate that the preferential location of filament activity is at the outermost part of the torus, where the plasma is susceptible to interchange instability. Interchange instability at the plasma edge arises from pressure gradients in a plasma constrained by an inhomogeneous magnetic field. In the simple picture in Fig. 1.2, plasma pressure on the inner (left) boundary of the shaded region is significantly higher than that on the outer (right) boundary. The curvature and gradient of the magnetic

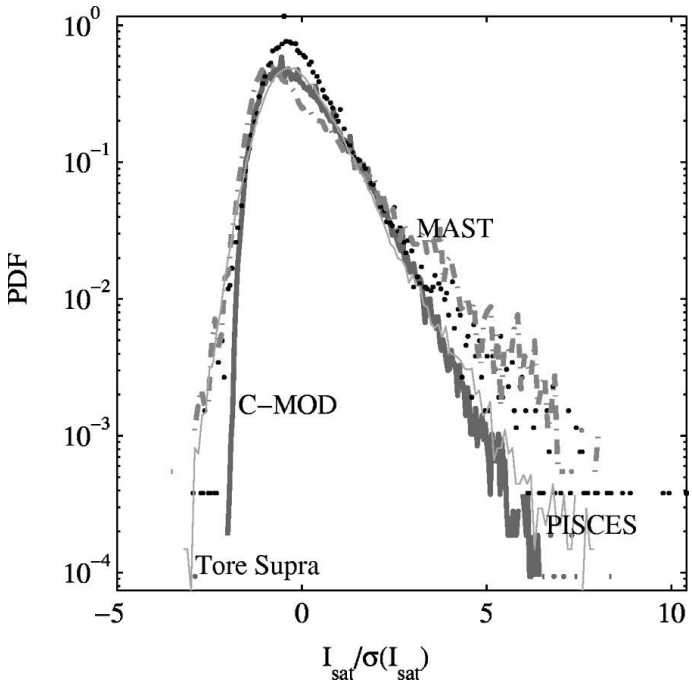

Figure 1.4: A semilogarithmic plot of the PDF of the ion saturation current in the Tore Supra (solid line), Alcator C-Mod (thick solid line), MAST (dashed–dotted line), and PISCES (dots). The ion saturation current was normalised to the standard deviation and the integral of the four PDF is set equal to 1. Image taken from Antar et al. (2003).

field result in an effective gravitational force acting radially outwards from the axis of the tokamak (i.e. to the right here). Thus, the equilibrium pressure gradient force points in the same direction as the effective gravitational acceleration, thereby leading to unstable stratification. The plasma is thus susceptible to interchange instability in which high pressure plasma is interchanged with neighbouring lower pressure regions in an overturning motion. This mechanism is analogous to that of Rayleigh-Bénard convection, in which overturning motions arise owing to the presence of a temperature gradient aligned with gravity — this analogy will be explored in Chapter 3. Experimental observations indicate that blobs are born in a region where the edge pressure gradient peaks (Myra et al., 2006). Thus, interchange dynamics is thought to play a dominant role in generating turbulent motions in the SOL.

State-of-the-art numerical models which incorporate a comprehensive description of the dynamics of plasma in a tokamak are the holy grail for the success of fusion experiments. In the long term, such models would offer predictive capabilities for the heat and particle loads on tokamak plasma-facing components. Reaching such modelling capabilities is extremely challenging. Tokamak plasmas exhibit abundant complex nonlinear turbulent phenomena on a wide range of spatial and temporal scales. The problem is further complicated by the complex magnetic geometry involved at the periphery of tokamak devices and by the presence of plasma sheaths at the divertor targets. Such simulations however, especially ones containing vast arrays of effects including full magnetic geometry, electrodynamics,

and parallel ion and electron dynamics, are difficult to interpret and analyse owing to the complex entanglement of various effects.

As a consequence, reduced models are used to shed light on the fundamental processes underlying specific plasma phenomena, such as turbulent transport and filament formation at the plasma edge. Reduced models are derived from the Braginskii fluid equations under the assumption that typical fluid velocities are much smaller than the thermal speed of the plasma, and that the evolution timescale is much slower compared to the timescale of particle gyration around the field lines. These reduced models can be used to study plasma dynamics in a realistic geometry, or further reduced to focus on the dynamics in the outboard midplane region of plasma. In the latter case, a so-called slab geometry approximation is invoked, whereby the magnetic field is considered straight and constant, and the effects of curvature are reintroduced through effective gravity terms. Furthermore, two-dimensional models can be constructed, under the slab approximation, by invoking *ad hoc* closures for the dynamics in the parallel direction. Over the years, various numerical models have been developed and used to study boundary turbulence and filament dynamics, both in 2D and 3D; some of the notable examples include STORM (Easy et al., 2014), HESEL (Nielsen et al., 2015), GBS (Ricci et al., 2012) and TOKAM3X (Tamain et al., 2010). Although, in general, these models differ in the details and approximations (for an in-depth discussion of key differences between the models, see Militello et al. (2016); Riva et al. (2016)), their essential features remain the same, and good agreement has been found between the different models (Militello et al., 2016).

There are, in general, two types of simulation strategies commonly employed to study SOL filaments: turbulence simulations and seeded blob simulations. Seeded blob simulations consider the evolution of a single blob that constitutes the initial condition for the simulations. The plasma density profile of seeded blobs is usually taken to be Gaussian with the magnitude of plasma density in the blob significantly higher than the background plasma density. Seeded blobs simulations were successful in demonstrating self-consistent evolution of density blobs in an initially uniform plasma at rest. These models confirmed the physical arguments laid out by Krasheninnikov (2001): i.e. that the radial motion of the blobs can be an effect of plasma polarization, caused by curvature and $\boldsymbol{\nabla} B$ effects, which results in $\boldsymbol{E} \times \boldsymbol{B}$ radial plasma flow. Isolated filament simulations allow for the propagation mechanism to be studied in detail. Numerous studies of isolated filaments were conducted both in slab geometries, two-dimensional (e.g. Olsen et al., 2016; Yu et al., 2006) and three-dimensional (e.g. Angus et al., 2012; Easy et al., 2016), and realistic tokamak geometries (e.g. Walkden et al., 2013), using models of various levels of complexity. The goal of these studies is to deduce scaling laws for the radial velocity of blobs, and the associated particle flux due to filaments. The relative low computational cost of seeded blob simulations, especially in 2D, allows for extensive parameter studies assessing how different plasma conditions affect the filament evolution. Complete control of initial conditions allows for direct investigation of effects of filament geometry (Omotani et al., 2015), as well interaction of multiple filaments (Militello et al., 2017). Additionally, seeded blob simulations are used to examine the impact of different physical effects on the motion of

filaments. Over the years, as more and more physical effects are included in the models – building towards a comprehensive picture of SOL plasma transport – seeded blob simulations have become the test bed for new physics, whereby the influence of new physics has been measured principally through changes in blob dynamics.

Turbulence simulations aim to provide a comprehensive picture of plasma trasport in the SOL, which includes self-consistent generation of filaments. While 3D turbulence simulations have emerged as the new standard in recent years (Riva et al., 2019), 2D codes are still commonly employed, as they have the advantage of greatly simplifying the analysis of cross-field SOL transport, while still retaining the fundamental properties of the underlying physics. Two-dimensional interchange models successfully capture several statistical properties of plasma turbulence and intermittent events in the tokamak SOL, such as the positively skewed ion saturation current PDFs universally observed in magnetic confinement fusion devices, the shape and duration of the bursts in the time traces, and the time-separation between them.

Despite the success of 2D models and their extensive and continued use in modelling edge plasma transport, there has been surprisingly little work on exploring their linear stability properties. Stability properties of complicated fluid systems can be studied using a technique of *linear stability analysis*. The method begins with identification of an equilibrium state, which may be spatially dependent. Next, this equilibrium state is augmented by the addition of small perturbations. These perturbations are small in the sense that any product of perturbations may be neglected, thus resulting in a linear system governing the dynamics of perturbations around the equilibrium state. This linear system constitutes a generalised eigenvalue problem, and the stability of the equilibrium state is governed by the eigenvalue, the real part of which denotes the growth rate of the perturbations. Accordingly, when the growth rate is negative, disturbances decay away in time and the equilibrium is stable. By contrast, when the growth rate is positive, disturbances grow in time and the system departs from the equilibrium state. The aim of linear stability analysis is to identify the region in the parameter space where the equilibrium state of the system becomes unstable to small disturbances. Stability is usually defined in terms of a key parameter that describes the forcing in the system. When the value of this parameter exceeds the critical threshold the system becomes unstable. Knowledge of the critical threshold is key to characterising the conditions at the onset of instability. In particular, it provides insight of the underlying mechanism for the instability, and how the physical effects in the system affect its stability. Additionally, the eigenfunctions of the linearized system shed light on the flow pattern that emerges post instability. As such, understanding of linear stability properties forms a basis for the analysis of the subsequent nonlinear evolution of the system and plays a key role in understanding the transition to turbulent flow.

In this thesis we perform a systematic analysis of transport models (of increasing complexity) relevant to dynamics of plasma at the edge of magnetic confinement devices. The outline of the thesis is as follows. In Chapter 2 we introduce the theoretical framework

necessary to study the dynamics of magnetically confined plasmas. We introduce the Braginskii fluid plasma equations, and outline the derivation of the reduced drift-fluid model describing interchange motions at the plasma edge. We distinguish between two types of modelling approach: single region models, which focus solely on the dynamics in the SOL (the solid shaded region A in Figure 1.2); and two region models, which consider a configuration composed of both the core and SOL regions (labelled B and A in Figure 1.2). The single region problem will be studied in Chapter 3, whereas Chapters 4 and 5 will focus on the two region problem. The overarching theme in this thesis is the analogy between interchange motions in magnetised plasma and thermal convection in neutral fluids. In Chapter 3 we study the linear stability of the derived model, in a single region context, and explore in detail the analogy between the model and Rayleigh-Bénard convection. Chapter 4 concerns a two-layer miscible convection problem as an idealised model for the interaction between the core plasma and the scrape-off layer. Owing to differences in magnetic field topology, properties of plasma, such as particle diffusion (analogous to thermal diffusivity) and viscosity, can potentially vary between the two regions. This results in complicated coupling between the two regions, with the ensuing model being analogous to two-layer convection. We explore the implications of the variation in the values of the diffusion coefficients between the two regions via a linear stability analysis of the purely hydrodynamic two-layer convection problem. In Chapter 5 we extend the analysis of Chapter 3 and study the onset of instability in the full two region plasma model. In Chapter 6 we summarise and discuss possible avenues for further work.

Chapter 2

The dynamics of plasma

2.1 Introduction

In this chapter we introduce basic ideas about plasma dynamics and derive a set of equations used to study interchange dynamics at the plasma edge. The technical content of this chapter has been heavily inspired by the textbooks of Hazeltine and Waelbroeck (2004), Hazeltine and Meiss (2003), and Bellan (2008). We begin by establishing some fundamental properties of magnetized plasma. We then outline the equations governing the dynamics of plasma. Specifically, we introduce the fluid description of plasma. We then apply a sequence of successive reductions to derive a model suitable for studying interchange motions at the edge of tokamak plasma. Finally, we close the chapter with a short description of Rayleigh-Bénard convection.

2.2 Fundamentals

2.2.1 Properties of magnetised plasma

A magnetised plasma is one in which the ambient magnetic field is strong enough to affect fluid behaviour. In particular, magnetised plasma is anisotropic, meaning it responds in different ways to forces that are parallel or perpendicular to the directions of $\boldsymbol{B}$. This can be illustrated most simply by considering the properties of the magnetic force,

$$\boldsymbol{F} = q\boldsymbol{v} \times \boldsymbol{B}, \tag{2.1}$$

where q is the particle charge and $\boldsymbol{v}$ its velocity. While the magnetic force is unable to affect particle speeds, it radically affects their trajectories. Plasma particles are allowed to stream freely in the direction parallel to $\boldsymbol{B}$, but their motion perpendicular to $\boldsymbol{B}$ is restricted to movement (gyration) on helical orbits around the magnetic field lines, called Larmor orbits. The orbits' radii are inversely proportional to the strength of the magnetic field: as the magnetic field increases, the helical orbits become tightly wound, effectively tying particles to the field lines. The gyration radius of a charged particle subject to magnetic force is given by

$$\rho = \frac{v_\perp}{\Omega}, \tag{2.2}$$

where $v_\perp$ is the component of the particle's velocity in the direction perpendicular to $\boldsymbol{B}$ and

$$\Omega = \frac{eB}{m} \tag{2.3}$$

is the cyclotron frequency, or *gyrofrequency*, associated with gyration. For practical purposes we are interested in the thermal gyroradius

$$\rho_t = \frac{v_t}{\Omega}, \tag{2.4}$$

where the thermal speed v_t is the estimate of typical particle speeds in the system,

$$v_{ts} \equiv \sqrt{\frac{2T_s}{m_s}}. \tag{2.5}$$

Assuming that both ions and electrons are characterized by the same temperature T, the thermal speed for ion and electron species differ by a substantial factor:

$$v_{ti} \sim \sqrt{\frac{m_e}{m_i}}\, v_{te} \ll v_{te}. \tag{2.6}$$

Similarly, there is a distinct gyroradius for each species; when species temperatures are comparable, the electron gyroradius is distinctly smaller than any ion gyroradius:

$$\rho_e \sim \left(\frac{m_e}{m_i}\right)^{1/2} \rho_i. \tag{2.7}$$

A plasma system or process is magnetised if its characteristic scale length L is large compared to the gyroradii of constituent charged particles. The magnetization parameter, δ, is the ratio of the thermal gyroradius to the plasma scale length

$$\delta \equiv \frac{\rho}{L}, \tag{2.8}$$

and is the fundamental measure of the effect of a magnetic field on a plasma. For a magnetised plasma, δ is much less than one. Since the electron gyroradius is much smaller than the ion gyroradius according to (2.7), the same distinction pertains to the parameter δ:

$$\delta_e \sim \left(\frac{m_e}{m_i}\right)^{1/2} \delta_i \ll \delta_i. \tag{2.9}$$

We shall only call a plasma magnetised if its ions are magnetised, i.e. $\delta_i \ll 1$. Magnetization can also be measured through the ratio of transit frequency ω_t to gyrofrequency:

$$\delta = \frac{\omega_t}{\Omega}, \tag{2.10}$$

where the transit frequency

$$\omega_t \equiv \frac{v_t}{L} \tag{2.11}$$

measures the rate at which particles traverse the system.

2.2.2 Kinetic description of plasma

To describe the dynamics of plasma exactly we must follow the motion of all of its particles as well as the dynamics of the electric and magnetic fields themselves. The electric and magnetic fields obey Maxwell's equations

$$\begin{aligned} \boldsymbol{\nabla}\cdot\boldsymbol{B} &= 0, & \boldsymbol{\nabla}\times\boldsymbol{E} &= -\frac{\partial \boldsymbol{B}}{\partial t}, \\ \boldsymbol{\nabla}\cdot\boldsymbol{E} &= \frac{\rho_c}{\varepsilon_0}, & \boldsymbol{\nabla}\times\boldsymbol{B} &= \mu_0\boldsymbol{J} + \frac{1}{c^2}\frac{\partial \boldsymbol{E}}{\partial t}, \end{aligned} \tag{2.12}$$

where ε_0 is the permittivity, μ_0 is the permeability, and $c = (\varepsilon_0\mu_0)^{-1/2}$ is the speed of light in vacuum.

Maxwell's equations become a closed, predictive system for the electrodynamic field only once the constitutive relations specifying the electric charge ρ_c, and current density $\boldsymbol{J}$, in terms of the remaining fields

$$\rho = \hat{\rho}\left[\boldsymbol{E}, \boldsymbol{B}, \boldsymbol{x}, t\right], \qquad \boldsymbol{J} = \hat{\boldsymbol{J}}\left[\boldsymbol{E}, \boldsymbol{B}, \boldsymbol{x}, t\right],$$

are determined.

In kinetic theory, the state of a plasma is specified by the distribution function $\mathcal{F}_\sigma(\boldsymbol{r}, \mathbf{v}, t)$, prescribing the instantaneous density of particles in phase space. Thus, $\mathcal{F}_\sigma(\boldsymbol{r}, \mathbf{v}, t)\,\mathrm{d}\boldsymbol{r}\,\mathrm{d}\mathbf{v}$ represents the number of particles at time t having positions in the range between $\boldsymbol{r}$ and $\boldsymbol{r}+\mathrm{d}\boldsymbol{r}$ and velocities in the range between $\mathbf{v}$ and $\mathbf{v}+\mathrm{d}\mathbf{v}$. Knowing the distribution function, we can form the following constitutive relations

$$\rho_c = \sum_\sigma e_\sigma \int \mathcal{F}_\sigma(\boldsymbol{r}, \mathbf{v}, t)\,\mathrm{d}\mathbf{v}, \tag{2.13}$$

$$\boldsymbol{J} = \sum_\sigma e_\sigma \int \mathbf{v}\mathcal{F}_\sigma(\boldsymbol{r}, \mathbf{v}, t)\,\mathrm{d}\mathbf{v}, \tag{2.14}$$

which provide closure to Maxwell's equations.

Now, closure in principle is accomplished once we know the kinetic equation that specifies the evolution of each distribution function in terms of given fields. The distribution function evolves according to phase–space conservation,

$$\frac{\partial \mathcal{F}_\sigma}{\partial t} + (\mathbf{v}\cdot\nabla)\,\mathcal{F}_\sigma + (\boldsymbol{a}_\sigma\cdot\nabla_v)\,\mathcal{F}_\sigma = 0, \tag{2.15}$$

where $\boldsymbol{a}_\sigma$ is the species–σ particle acceleration due to the Lorenz force

$$\boldsymbol{a}_\sigma = \frac{\mathrm{d}\mathbf{v}}{\mathrm{d}t} = \frac{e_\sigma}{m_\sigma}\left(\boldsymbol{E} + \mathbf{v}\times\boldsymbol{B}\right). \tag{2.16}$$

Although appearing simple, equation (2.15) is not tractable. The equation takes into account all scales from microscopic to macroscopic. Since there has been no statistical averaging involved in deriving it, the exact distribution function $\mathcal{F}_\sigma$ is essentially a sum of Dirac delta-functions, each following the detailed trajectory of a single particle.

Similarly, forces in (2.16) include not only externally imposed forces, but the complete electromagnetic interactions between all particle trajectories in the system. Thus the resulting distribution function and acceleration fields are horribly spiky and chaotic on the microscopic scales, and essentially not tractable.

A much more useful and tractable equation is obtained from (2.15) by ensemble averaging. Each quantity is separated into a smooth, averaged part and a fluctuating part: $\mathcal{A} = \bar{\mathcal{A}} + \mathcal{A}'$, with

$$\langle \mathcal{A} \rangle_{ens} = \bar{\mathcal{A}}, \qquad \langle \mathcal{A}' \rangle_{ens} = 0, \tag{2.17}$$

where $\langle \cdots \rangle_{ens}$ denotes the ensemble average. Averaged distribution function and electromagnetic fields are sensibly smooth and closely related to experimental measurements. The ensemble average of (2.15) yields the plasma kinetic equation

$$\frac{\partial f_\sigma}{\partial t} + (\mathbf{v} \cdot \nabla) f_\sigma + (\bar{\boldsymbol{a}}_\sigma \cdot \nabla_v) f_\sigma = \mathcal{C}_\sigma (f), \tag{2.18}$$

where $f_\sigma \equiv \bar{\mathcal{F}}_\sigma$. Because $\boldsymbol{E}$ and $\boldsymbol{B}$ are not statistically independent of $\mathcal{F}_\sigma$ (since the exact electromagnetic fields depend of particle trajectories), ensemble average of the nonlinear acceleration term $\boldsymbol{a}_\sigma \cdot \nabla_v \mathcal{F}_\sigma$ gives rise to two terms in (2.18): $(\bar{\boldsymbol{a}}_\sigma \cdot \nabla_v) f_\sigma$, which contains only statistically independent parts of $\boldsymbol{a}_\sigma$ and $\mathcal{F}_\sigma$, and the collision operator $\mathcal{C}_\sigma (f)$, which accounts for the residual effects of particle correlations

$$\mathcal{C}_\sigma (f) = (\bar{\boldsymbol{a}}_\sigma \cdot \nabla_v) f_\sigma - \langle (\boldsymbol{a}_\sigma \cdot \nabla_v) \mathcal{F}_\sigma \rangle . \tag{2.19}$$

The collision operator is an extremely complicated operator that accounts for the correlations resulting from close encounters between particles and it usually involves distribution functions of all plasma species. Thus $\mathcal{C}_\sigma(f)$ denotes the rate of change of f_σ due to collisions of species σ with other species,

$$\mathcal{C}_\sigma(f) = \sum_\alpha \mathcal{C}_{\sigma\alpha}(f_\sigma, f_\alpha). \tag{2.20}$$

The exact version of the collision operator is not known, but there are certain constraints on it that need to be satisfied:

- **Particle conservation**
  Collisions cannot change the total number of particles in a particular volume element:

$$\int \mathcal{C}_{\sigma\alpha} (f_\sigma) \, \mathrm{d}\mathbf{v} = 0. \tag{2.21}$$

- **Momentum conservation**
  Collisions between particles of the same species cannot change the total momentum of that species:

$$\int m_\sigma \mathbf{v} \, \mathcal{C}_{\sigma\sigma} (f_\sigma) \, \mathrm{d}\mathbf{v} = 0. \tag{2.22}$$

  Collisions between different species must conserve the total momentum of both

species together:

$$\int m_i \mathbf{v}\, \mathcal{C}_{ie}\left(f_i\right)\, \mathrm{d}\mathbf{v} + \int m_e \mathbf{v}\, \mathcal{C}_{ei}\left(f_e\right)\, \mathrm{d}\mathbf{v} = 0. \tag{2.23}$$

- **Energy conservation**
  Collisions between particles of the same species cannot change the total energy of that species:
  $$\int \frac{1}{2} m_\sigma v^2\, \mathcal{C}_{\sigma\sigma}\left(f_\sigma\right)\, \mathrm{d}\mathbf{v} = 0. \tag{2.24}$$
  Collisions between different species must conserve the total energy of both species together:
  $$\int m_i v^2\, \mathcal{C}_{ie}\left(f_i\right)\, \mathrm{d}\mathbf{v} + \int m_e v^2\, \mathcal{C}_{ei}\left(f_e\right)\, \mathrm{d}\mathbf{v} = 0. \tag{2.25}$$

Given the collision operator $C_\sigma(f)$, the kinetic equation (2.18) together with (ensemble-averaged) Maxwell's equations (2.12) constitutes the most rigorous and complete description of plasma dynamics. However, extracting $C_\sigma(f)$ is an extremely challenging mathematical exercise which always requires severe approximation. Furthermore, set in the six dimensional phase space, equation (2.18) is difficult to solve analytically and expensive to solve numerically. This is one of the reasons why closure strategy based solely on the kinetic equation (2.18) is rarely effective. Further approximations are necessary to reduce the kinetic equation into a practically usable form (e.g. drift-kinetic, gyro-kinetic equation).

Since closure of the Maxwell's equations requires the two lowest order moments of f_σ, namely the density and the flow velocity, the solution to (2.15) contains vastly more information than is needed. An alternative closure strategy is obtained by employing a macroscopic fluid description which attempts to express the two necessary moments in terms of other more accessible quantities.

2.2.3 Fluid description of plasma

Plasma fluid theory approximates plasma as a system of mutually interacting electron and ion fluids. The essential advantage of fluid theory is a marked reduction in the number of dimensions involved in the problem; three spatial dimensions instead of six phase-space dimensions. Furthermore, fluid variables, such as density, velocity and pressure, are more immediately significant and meaningful to us, whereas the significance of distribution functions is less obvious. These quantities are advanced in time by means of fluid equations that are analogous to, but usually more complicated than, the equations of ordinary hydrodynamics. Thus the goal of plasma fluid theory is to construct and solve a plasma version of the Navier-Stokes equation.

We obtain fluid equations by taking appropriate moments of the Boltzmann equation, (2.18). The k^{th} moment of the distribution function f_σ is

$$\boldsymbol{M}_k(\boldsymbol{r}, t) = \int \mathbf{v}\mathbf{v}\ldots\mathbf{v} f_\sigma(\boldsymbol{r}, \mathbf{v}, t)\, \mathrm{d}\mathbf{v}, \tag{2.26}$$

with k factors of $\mathbf{v}$.

The set of moments provides an alternative, smooth description of the distribution function. The physical interpretations of the zeroth, first, second and third-order moments are respectively particle density, particle flux density, stress tensor and energy flux density:

$$n_\sigma = \int f_\sigma(\boldsymbol{r}, \mathbf{v}, t)\, \mathrm{d}\mathbf{v}, \tag{2.27}$$

$$n_\sigma \boldsymbol{v}_\sigma = \int \mathbf{v} f_\sigma(\boldsymbol{r}, \mathbf{v}, t)\, \mathrm{d}\mathbf{v}, \tag{2.28}$$

$$\boldsymbol{P}_\sigma = \int m_\sigma \mathbf{v}\mathbf{v} f_\sigma(\boldsymbol{r}, \mathbf{v}, t)\, \mathrm{d}\mathbf{v}, \tag{2.29}$$

$$\boldsymbol{Q}_\sigma = \int \frac{1}{2} m_\sigma v^2 \mathbf{v} f_\sigma(\boldsymbol{r}, \mathbf{v}, t)\, \mathrm{d}\mathbf{v}. \tag{2.30}$$

The governing equations for a simple plasma are comprised of the equations of continuity, momentum and heat balance for electrons and ions. These are, respectively, the first three moments of equation (2.18) ,

$$\frac{\partial n_\sigma}{\partial t} + \nabla \cdot (n_\sigma \boldsymbol{v}_\sigma) = 0, \tag{2.31}$$

$$m_\sigma \left(\frac{\partial}{\partial t} (n_\sigma \boldsymbol{v}_\sigma) + \boldsymbol{\nabla} \cdot \left(n_\sigma \boldsymbol{v}_\sigma \boldsymbol{v}_\sigma + \frac{1}{m_\sigma} \boldsymbol{p}_\sigma \right) \right) = e_\sigma n_\sigma \left(\boldsymbol{E} + \boldsymbol{v}_\sigma \times \boldsymbol{B} \right) + \boldsymbol{F}_\sigma, \tag{2.32}$$

$$\frac{\partial}{\partial t} \left(\frac{N p_\sigma}{2} + \frac{1}{2} m_\sigma n_\sigma u_\sigma^2 \right) + \boldsymbol{\nabla} \cdot \left(\frac{1}{2} m_\sigma n_\sigma u_\sigma^2 \boldsymbol{v}_\sigma + \boldsymbol{v}_\sigma \cdot \boldsymbol{p}_\sigma + \frac{N}{2} p_\sigma \boldsymbol{v}_\sigma + \boldsymbol{q}_\sigma \right) = e_\sigma n_\sigma \boldsymbol{v}_\sigma \cdot \boldsymbol{E} + \boldsymbol{v}_\sigma \cdot \boldsymbol{F}_\sigma + \mathcal{W}_\sigma, \tag{2.33}$$

where (2.31) is the continuity equation, (2.32) is the momentum conservation equation and (2.33) the energy conservation equation for species σ. From equation (2.31) we see that $n_\sigma \boldsymbol{v}_\sigma$ is indeed the species particle flux density, and that there are no local sources or sinks of particles. From equation (2.32), we see that the stress tensor $\boldsymbol{P}_\sigma = \boldsymbol{p}_\sigma / m_\sigma + n_\sigma \boldsymbol{v}_\sigma \boldsymbol{v}_\sigma$, where $\boldsymbol{p}_\sigma$ is the pressure tensor, gives the species momentum flux density, and that the species momentum is changed locally by the Lorentz force, $e_\sigma n_\sigma \left(\boldsymbol{E} + \boldsymbol{v}_\sigma \times \boldsymbol{B} \right)$, and by net frictional drag force due to collisions between species, $\boldsymbol{F}_\sigma$. Finally, in equation (2.33), the energy flux density is written as $\boldsymbol{Q}_\sigma = \frac{1}{2} m_\sigma n_\sigma u_\sigma^2 \boldsymbol{u}_\sigma + \boldsymbol{v}_\sigma \cdot \boldsymbol{p}_\sigma + \frac{N}{2} p_\sigma \boldsymbol{v}_\sigma + \boldsymbol{q}_\sigma$ where $\boldsymbol{q}_\sigma$ is the heat flux density and N denotes the dimension of the velocity space. The species energy is changed locally by electrical work, $e_\sigma n_\sigma \boldsymbol{v}_\sigma \cdot \boldsymbol{E}$, energy exchange between species, $\boldsymbol{v}_\sigma \cdot \boldsymbol{F}_\sigma$, and frictional heating, $\mathcal{W}_\sigma$. A detailed derivation of these equations can be found in Appendix A.

The fluid equations in their present form (2.31) - (2.33) are exact, but incomplete. The evolution of each fluid moment depends on the next higher order moment. As a result any finite set of exact equations will contain more unknowns than equations. We need some

additional information to express quantities such as viscous tensor, $\boldsymbol{\pi}$, heat flux, $\boldsymbol{q}$, and the moments of the collision operator $\boldsymbol{F}$ and $\mathcal{W}$ in terms of lower order moments. The closure can be achieved either through truncation or asymptotic calculation of higher order moments. The asymptotic closure relies on expanding the underlying distribution function $f_\sigma(\mathbf{x}, \mathbf{v}, t)$ in some small parameter and solving the kinetic equation perturbatively to estimate the unknown moments, thus closing the system of equations. Asymptotic closure for the heat flux, viscosity tensor and collision friction terms in equations (2.31) - (2.33) has been provided by Braginskii (1965). The resulting closed set of equations, the *Braginskii equations*, describe the evolution of collisional, magnetised plasma and have frequent and effective applications.

In the next section we reduce the Braginskii equations even further using information about the characteristics of the electric field and typical plasma flow velocities in the magnetic confinement experiments. We thus derive a *drift-fluid* model pertinent to the dynamics of plasma in a tokamak.

2.3 Drift-fluid model

2.3.1 Fundamental concepts

Consider the momentum equation (2.32) in the non-conservative form, suppressing species index for ease of notation:

$$mn\left(\frac{\partial}{\partial t} + \boldsymbol{v}\cdot\boldsymbol{\nabla}\right)\boldsymbol{v} + \boldsymbol{\nabla}p + \boldsymbol{\nabla}\cdot\boldsymbol{\pi} - en\left(\boldsymbol{E} + \boldsymbol{v}\times\boldsymbol{B}\right) = \boldsymbol{F}. \tag{2.34}$$

Each term in the equation of motion has the form of a momentum multiplied by a certain frequency. The frequency of the acceleration term is the dynamical frequency, $\frac{\mathrm{d}}{\mathrm{d}t} \sim \omega$, which characterizes the process under consideration. The frequency of the pressure gradient force and the viscous stress is the transit frequency ω_t. The magnetic force term is associated with the gyrofrequency Ω, and the friction term is associated with the collision frequency ν. The term involving the electric field appears without a definite frequency.

The key observation is that the gyrofrequency Ω associated with the $\boldsymbol{v}\times\boldsymbol{B}$ term dominates all other frequencies in a magnetised plasma. By taking the cross product of the momentum equation with $\hat{\boldsymbol{b}}$ we obtain an implicit expression for the perpendicular velocity:

$$\boldsymbol{v}_\perp = \boldsymbol{v}_E + \frac{1}{mn\Omega}\hat{\boldsymbol{b}}\times\left(mn\frac{\mathrm{d}\boldsymbol{v}}{\mathrm{d}t} + \boldsymbol{\nabla}p + \boldsymbol{\nabla}\cdot\boldsymbol{\pi} - \boldsymbol{F}\right), \tag{2.35}$$

where $\boldsymbol{v}_E = (\boldsymbol{E}\times\boldsymbol{B})/B^2$ is the $\boldsymbol{E}\times\boldsymbol{B}$, or electric, drift velocity. Thus, the perpendicular velocity is expressed as a sum of *drift* velocities. The key feature of (2.35) is the $1/\Omega$ factor outside the bracket. Since the frequencies of the terms inside the bracket in are much smaller than the gyrofrequency, the $1/\Omega$ plays the role of δ, giving (2.35) the form $\boldsymbol{v}_\perp = \boldsymbol{v}_E + \delta(\ldots)$. Thus, the bracketed drifts contribute at most $\mathcal{O}(\delta)$ to the perpendicular plasma flow. The electric drift is exceptional because small δ does not restrict the magnitude of the electric field $\boldsymbol{E}$; it is up to us to decide on its ordering depending on the

process under consideration.

There are two main ordering schemes for magnetised plasma dynamics: the magneto-hydrodynamic (MHD) ordering and the drift ordering. These orderings refer to the relative strength of the transverse electric field, and hence the electric drift $\boldsymbol{v}_E$, compared with the ion thermal speed v_{ti}, or plasma sound speed. In MHD the perpendicular electric field is large and thus plasma can move quickly across the magnetic field, with flow velocities near the thermal speed, i.e.

$$\boldsymbol{v}_E \sim \frac{E_\perp}{B} \sim v_t. \tag{2.36}$$

MHD is designed to study phenomena that occur on fast time scales (given by the transit frequency ω_t): rapid, even violent, motions of magnetised plasma. In contrast plasma phenomena in modern confinement devices evolve on much slower timescales and are more accurately described by drift ordering.

The drift ordering describes the evolution of magnetised plasma in the case of moderate electric fields: i.e. when electric forces are comparable to the pressure gradient. In particular

$$\boldsymbol{v}_E \sim \frac{E_\perp}{B} \sim \delta v_t. \tag{2.37}$$

Thus, unlike in the MHD-ordered case where electric drifts dominate the dynamics, in the drift ordering the electric drift enters only in concert with other slow motions, such as the curvature and gradient-B drifts. The time evolution is relatively slow i.e.

$$\frac{\mathrm{d}}{\mathrm{d}t} \sim \delta\omega_t \sim \delta^2\Omega, \tag{2.38}$$

otherwise the induced electric field from Faraday's law could contradict $E/B \sim \delta v_t$. Furthermore, $\boldsymbol{E}$ is primarily electrostatic in the drift ordering $\boldsymbol{E} = -\boldsymbol{\nabla}\varphi[1+\mathcal{O}(\delta)]$ (Hazeltine and Meiss, 2003). Below, we apply the drift ordering assumptions to derive a reduced model from the Braginskii equations.

2.3.2 Drift-ordering

Over the years, a number of drift-fluid models have been derived by several authors (e.g. Drake and Antonsen Jr, 1984; Hazeltine et al., 1985; Hinton and Horton Jr, 1971; Madsen et al., 2016; Simakov and Catto, 2003; Zeiler et al., 1997). Although the starting assumptions are common between all models, they are unfortunately insufficient to provide a system of equations that is both closed and physically interesting. Thus, the differences between models arise on account of additional assumptions and approximations which are guided not necessarily by mathematical rigour but physical intuition and experimental insight, as well as motivated by the desire to retain computational practicability and conservation properties in the resulting model. On the whole, constructing meaningful reduced models is somewhat of an art form.

The drift model presented here is drawn from Easy et al. (2014, 2016). We begin by introducing a number of further simplifications. We consider the reduced case of fully ionised plasma consisting of electrons and singly charged ions (simple plasma; $\sigma \in \{e, i\}$).

The electric field is considered to be purely electrostatic, i.e. $\boldsymbol{E} = -\boldsymbol{\nabla}\varphi$, where φ is the plasma potential. Furthermore, we make the assumption of isothermal electrons (constant T_e) and cold ions (negligible ion temperature $T_i = 0$). In the cold ion limit, the Braginskii equations for an isothermal simple plasma in non-conservative form become:

$$\frac{\partial n_e}{\partial t} + \boldsymbol{\nabla}\cdot(n_e\boldsymbol{v}_e) = s_n, \tag{2.39}$$

$$\frac{\partial n_i}{\partial t} + \boldsymbol{\nabla}\cdot(n_i\boldsymbol{v}_i) = s_n, \tag{2.40}$$

$$m_e n_e\left(\frac{\partial}{\partial t} + \boldsymbol{v}_e\cdot\boldsymbol{\nabla}\right)\boldsymbol{v}_e + \boldsymbol{\nabla}p_e + \boldsymbol{\nabla}\cdot\boldsymbol{\pi}_e + en_e\left(\boldsymbol{E} + \boldsymbol{v}_e\times\boldsymbol{B}\right) = \boldsymbol{F}_{ei} - m_e s_n\boldsymbol{v}_e, \tag{2.41}$$

$$m_i n_e\left(\frac{\partial}{\partial t} + \boldsymbol{v}_i\cdot\boldsymbol{\nabla}\right)\boldsymbol{v}_i + \boldsymbol{\nabla}\cdot\boldsymbol{\pi}_i - en_e\left(\boldsymbol{E} + \boldsymbol{v}_i\times\boldsymbol{B}\right) = -\boldsymbol{F}_{ei} - m_i s_n\boldsymbol{v}_i. \tag{2.42}$$

Here, n_σ is particle density, $\boldsymbol{u}_\sigma$ is the fluid velocity, $p_\sigma = n_\sigma T_\sigma$ is the isotropic pressure, $\boldsymbol{\pi}_\sigma$ is the viscous stress tensor, e is the elementary charge, $\boldsymbol{E}$ and $\boldsymbol{B}$ denote the electric and magnetic field respectively; $\boldsymbol{F}_{ei}$ is the effective frictional force due to collisions between electrons and ions (Braginskii, 1965)

$$\boldsymbol{F}_{ei} = en_e\left(\frac{\boldsymbol{J}_\perp}{\sigma_\perp} + \frac{\boldsymbol{J}_\parallel}{\sigma_\parallel}\right), \tag{2.43}$$

where $\boldsymbol{J}_\perp$ and $\sigma_\perp$ are the perpendicular current density and perpendicular conductivity respectively, while $\boldsymbol{J}_\parallel$ and $\sigma_\parallel$ are the parallel current density and parallel conductivity. The conductivities are:

$$\sigma_\perp = 0.51\sigma_\parallel, \qquad \sigma_\parallel = \frac{n_e e^2}{0.51 m_e \nu_{ei}}. \tag{2.44}$$

The additional term s_n in (2.39) and (2.40) represents sources and sinks of particles due to ionisation or recombination processes. Consequently, the additional term on the right-hand side of (2.41) and (2.42) ensures conservation of momentum in the presence of a particle source. Lastly, note that we have replaced n_i by n_e in equation (2.42) using the quasi-neutrality requirement, i.e. $n_e = n_i$.

Taking the cross product of equations (2.41), (2.42) with $\hat{\boldsymbol{b}}$ gives the electron and ion perpendicular velocities:

$$\boldsymbol{v}_{\perp e} = \boldsymbol{v}_E + \boldsymbol{v}_D + \boldsymbol{v}_{Pe} + \boldsymbol{v}_{\pi e} + \boldsymbol{v}_F + \boldsymbol{v}_{Se}, \tag{2.45}$$

$$\boldsymbol{v}_{\perp i} = \boldsymbol{v}_E + \boldsymbol{v}_{Pi} + \boldsymbol{v}_{\pi i} + \boldsymbol{v}_F + \boldsymbol{v}_{Si}. \tag{2.46}$$

Here, defining each of the drifts in turn we have: the $\boldsymbol{E}\times\boldsymbol{B}$ drift

$$\boldsymbol{v}_E = \frac{\boldsymbol{E}\times\hat{\boldsymbol{b}}}{B} = \frac{\hat{\boldsymbol{b}}\times\nabla\varphi}{B}; \tag{2.47}$$

the diamagnetic drift

$$\boldsymbol{v}_D = -\frac{\hat{\boldsymbol{b}}\times\boldsymbol{\nabla}p_e}{en_e B}; \tag{2.48}$$

the electron and ion polarization drifts

$$\boldsymbol{v}_{Pe} = -\frac{m_e}{eB}\hat{\boldsymbol{b}} \times \left(\frac{\partial \boldsymbol{v}_e}{\partial t} + \boldsymbol{v}_e \cdot \boldsymbol{\nabla}\boldsymbol{v}_e\right), \qquad \boldsymbol{v}_{Pi} = \frac{m_i}{eB}\hat{\boldsymbol{b}} \times \left(\frac{\partial \boldsymbol{v}_i}{\partial t} + \boldsymbol{v}_i \cdot \boldsymbol{\nabla}\boldsymbol{v}_i\right); \tag{2.49}$$

the electron and ion drift velocities due to viscous forces

$$\boldsymbol{v}_{\pi e} = -\frac{\hat{\boldsymbol{b}} \times \boldsymbol{\nabla} \cdot \boldsymbol{\pi}_e}{en_eB}, \qquad \boldsymbol{v}_{\pi i} = \frac{\hat{\boldsymbol{b}} \times \boldsymbol{\nabla} \cdot \boldsymbol{\pi}_i}{en_eB}; \tag{2.50}$$

the drift due to friction between electrons and ions

$$\boldsymbol{v}_F = \frac{\hat{\boldsymbol{b}} \times \boldsymbol{F}_{ei}}{en_eB}; \tag{2.51}$$

and electron and ion drift velocities due to the sources or sinks of particles in the system

$$\boldsymbol{v}_{Se} = \frac{m_e\, s_n}{en_eB}\hat{\boldsymbol{b}} \times \boldsymbol{v}_e, \qquad \boldsymbol{v}_{Si} = -\frac{m_i\, s_n}{en_eB}\hat{\boldsymbol{b}} \times \boldsymbol{v}_i. \tag{2.52}$$

Using drift ordering assumptions we estimate the magnitude of each of the drift velocities in (2.45), (2.46). Note that in the cold ion limit, the plasma sound speed $c_s = (T_e/m_i)^{1/2}$ takes the place of the thermal speed, and the hybrid Larmor radius $\rho_s = c_s/\Omega_i$ takes the place of the gyroradius. Thus we estimate the drift velocities relative to the plasma sound speed c_s.

As described above, under the drift ordering the $\boldsymbol{E} \times \boldsymbol{B}$ drift is $\mathcal{O}(\delta)$ compared to the plasma sound speed. The diamagnetic drift (2.48) is also $\mathcal{O}(\delta)$:

$$\boldsymbol{v}_D \sim \frac{1}{L\Omega_i}\frac{T_e}{m_i} \sim \frac{1}{L}\frac{c_s}{\Omega_i}c_s \sim \frac{\rho_s}{L}c_s \sim \delta c_s. \tag{2.53}$$

Since flow velocities in the drift model are $\mathcal{O}(\delta)$ compared to the thermal speed, and dynamical frequencies are $\mathcal{O}(\delta)$ compared to the transit frequency ($\mathcal{O}(\delta^2)$ compared to the gyrofrequency), the polarisation drifts are $\mathcal{O}(\delta^3)$ compared to the plasma sound speed:

$$\boldsymbol{v}_{Pe} \sim \frac{m_e}{m_i}\frac{1}{\Omega_i}(\delta^2\Omega_i)(\delta c_s) \sim \frac{m_e}{m_i}\delta^3 c_s, \qquad \boldsymbol{v}_{Pi} \sim \delta^3 c_s. \tag{2.54}$$

To order the viscous drifts (2.50) the dominant contribution to the viscosity tensor $\boldsymbol{\pi}_\sigma$ is estimated by $\boldsymbol{\pi}_\sigma \sim (p_\sigma/\Omega_\sigma)\boldsymbol{\nabla}\boldsymbol{v}_\sigma$. Thus

$$\boldsymbol{v}_{\pi e} \sim \frac{n_eT_e}{\Omega_e}\frac{\delta c_s}{en_eBL^2} \sim \frac{m_e}{m_i}\left(\frac{c_s}{\Omega_iL}\right)^2 \delta c_s \sim \frac{m_e}{m_i}\delta^3 c_s, \qquad \boldsymbol{v}_{\pi i} \sim \delta^3 c_s. \tag{2.55}$$

Using (2.43), the friction drift (2.51) is estimated as

$$\boldsymbol{v}_F \sim \frac{m_e\nu_{ei}}{eB}\delta c_s \sim \frac{\nu_{ie}}{\Omega_i}\delta c_s. \tag{2.56}$$

Since $\nu_{ie}/\Omega_i \sim \delta$ almost always pertains in practice, the friction drift is $\boldsymbol{v}_F = \mathcal{O}(\delta^2)$. Finally, the remaining drifts due to sources (2.52) are free for us to order. In the following we assume that these are completely negligible. Formally, this can be accomplished by

assuming that the frequency at which the density is injected by the sources is smaller than the dynamical frequency, i.e. $s_n/n_e \ll \delta^2\Omega_i$; in this case drifts due to sources are $\mathcal{O}(\delta^3)$ for ions, and a factor m_e/m_i smaller for electrons, and as such much smaller than all other drifts.

The leading order electron perpendicular drifts consist of $\boldsymbol{E}\times\boldsymbol{B}$ and diamagnetic drifts. For ions, the sole dominant perpendicular drift is the electric drift — the ion diamagnetic drift has been eliminated on the basis of the cold ion assumption ($T_i = 0$). We retain the remaining formally small drifts with the exception of the mass dependent electron polarisation and viscous drifts, which are a factor $m_e/m_i \ll 1$ smaller than their ion counterparts. Thus, the electron and ion drifts are

$$\boldsymbol{v}_{\perp e} = \boldsymbol{v}_E + \boldsymbol{v}_D + \boldsymbol{v}_F, \tag{2.57}$$

$$\boldsymbol{v}_{\perp i} = \boldsymbol{v}_E + \boldsymbol{v}_{Pi} + \boldsymbol{v}_F + \boldsymbol{v}_{\pi i}. \tag{2.58}$$

The density evolution equation in the drift reduced system is constructed by substituting the sum of the electron drifts (2.57) and the parallel velocity ($v_{\parallel e}\hat{\boldsymbol{b}}$) in the place of the velocity in equation (2.39), yielding

$$\frac{\partial n_e}{\partial t} + \boldsymbol{v}_E\cdot\boldsymbol{\nabla}n_e + n_e\boldsymbol{\nabla}\cdot\left(\frac{\hat{\boldsymbol{b}}\times\boldsymbol{\nabla}\varphi}{B}\right) - \boldsymbol{\nabla}\cdot\left(\frac{\hat{\boldsymbol{b}}\times\boldsymbol{\nabla}p_e}{eB}\right) + \boldsymbol{\nabla}\cdot\left(\boldsymbol{v}_{\parallel e}n_e\right) + \boldsymbol{\nabla}\cdot\left(\boldsymbol{v}_F n_e\right) = s_n. \tag{2.59}$$

In equation (2.59) the drift due to friction accounts for collisional energy exchange between different plasma species and ultimately gives rise to particle density diffusion (Madsen et al., 2016):

$$\boldsymbol{\nabla}\cdot\left(\boldsymbol{v}_F n_e\right) \simeq -D\nabla_\perp^2 n_e, \tag{2.60}$$

where D is the collisional diffusion coefficient (we provide the expression for D in Section 2.3.6).

The momentum equation for plasma is formulated using the current conservation law $\boldsymbol{\nabla}\cdot\boldsymbol{J} = 0$. It follows from (2.57) and (2.58) that the total current density in the drift-reduced system, $\boldsymbol{J} = en_e(\boldsymbol{v}_i - \boldsymbol{v}_e)$, is the sum of the ion polarisation current density, the electron diamagnetic current density, the perpendicular current density due to ion viscosity, and the parallel current density:

$$\begin{aligned}\boldsymbol{J} &= \boldsymbol{J}_P + \boldsymbol{J}_D + \boldsymbol{J}_\pi + \hat{\boldsymbol{b}}J_\parallel \\ &= en_e\boldsymbol{v}_{Pi} - en_e\boldsymbol{v}_D + en_e\boldsymbol{v}_{\pi i} + \hat{\boldsymbol{b}}J_\parallel,\end{aligned} \tag{2.61}$$

where $J_\parallel = en_e\left(v_{\parallel i} - v_{\parallel e}\right)$. To leading order the ion polarization drift in the reduced system is

$$\boldsymbol{v}_{Pi} = \frac{m_i}{eB}\hat{\boldsymbol{b}}\times\left(\frac{\partial}{\partial t} + \boldsymbol{v}_E\cdot\boldsymbol{\nabla}_\perp + v_{\parallel i}\nabla_\parallel\right)\boldsymbol{v}_E = -\frac{m_i}{eB}\frac{\mathrm{d}}{\mathrm{d}t}\boldsymbol{\nabla}_\perp\varphi. \tag{2.62}$$

In the viscous drift, the influence of ion viscosity is approximated as $\boldsymbol{\nabla}\cdot\boldsymbol{\pi}_i = -m_i n_e \nu_i \nabla_\perp^2 \boldsymbol{v}_E$, where ν_i is the effective cross field kinematic viscosity of the ions (Madsen et al., 2016).

Under this simplification the viscous drift velocity $\boldsymbol{v}_{\pi i}$ becomes

$$\boldsymbol{v}_{\pi i} = \frac{m_i \nu_i}{eB^2} \boldsymbol{\nabla}_\perp \nabla_\perp^2 \varphi. \tag{2.63}$$

Using the expression for the current density (2.61) together with drift velocities (2.62), (2.48), (2.63) in the current continuity condition, $\boldsymbol{\nabla} \cdot \boldsymbol{J} = 0$, leads to the *vorticity equation*:

$$\frac{m_i}{B^2} \boldsymbol{\nabla}_\perp \cdot \left(n_e \frac{\mathrm{d}}{\mathrm{d}t} \boldsymbol{\nabla}_\perp \varphi \right) = \nabla_\parallel J_\parallel + T_e \boldsymbol{\nabla} \cdot \left(\frac{\hat{\boldsymbol{b}} \times \boldsymbol{\nabla} n_e}{B} \right) + \boldsymbol{\nabla}_\perp \cdot \left(\frac{n_e m_i \nu_i \boldsymbol{\nabla}_\perp \nabla_\perp^2 \varphi}{B^2} \right), \tag{2.64}$$

where we have also used the assumption of an isothermal plasma $\boldsymbol{\nabla} p_e = T_e \boldsymbol{\nabla} n_e$.

Finally, the parallel dynamics of ions and electrons are obtained by isolating the parallel components of equations (2.41) and (2.42), and retaining leading order terms, which produces

$$m_e n_e \left(\frac{\partial}{\partial t} + \boldsymbol{v}_E \cdot \boldsymbol{\nabla}_\perp + v_{\parallel e} \nabla_\parallel \right) v_{\parallel e} = e n_e \nabla_\parallel \varphi - T_e \nabla_\parallel n_e + e n_e \eta J_\parallel - m_e s_n v_{\parallel e}, \tag{2.65}$$

$$m_i n_e \left(\frac{\partial}{\partial t} + \boldsymbol{v}_E \cdot \boldsymbol{\nabla}_\perp + v_{\parallel i} \nabla_\parallel \right) v_{\parallel i} = -e n_e \nabla_\parallel \varphi - e n_e \eta J_\parallel - m_i s_n v_{\parallel i}, \tag{2.66}$$

where $\eta = 1/\sigma_\parallel$ is the resistivity. In equations (2.65), (2.66) only $\mathcal{O}(\delta)$ perpendicular drifts enter the material derivative for both ions and electrons, out of which the diamagnetic advection terms in (2.65) cancel out with the gyroviscous component of the viscous stress tensor — this result is sometimes referred to as the gyroviscous cancellation (e.g. Hazeltine and Waelbroeck, 2004, p. 132). The remaining viscous terms do not contribute to the leading order balance.

2.3.3 Slab geometry approximation

We shall restrict our attention to the region of plasma located at the outboard midplane of the tokamak, and consider the dynamics under the so-called slab geometry approximation. Under this approximation the geometry is approximated as a local slab with a uniform magnetic field, $\boldsymbol{B} = B\hat{\mathbf{e}}_z$ (Krasheninnikov et al., 2008). In the simplified geometry the forces responsible for interchange motions — magnetic curvature and inhomogeneity of $\boldsymbol{B}$ — disappear, and need to be reintroduced using an effective gravity force acting in the effective radial direction. To restore the influence of both magnetic curvature and magnetic gradients in the slab geometry, the following relation is used in equations (2.59), (2.64) (D'Ippolito et al., 2002):

$$\boldsymbol{\nabla} \cdot \left(\frac{\hat{\boldsymbol{b}} \times \boldsymbol{\nabla} f}{B} \right) = -\frac{2}{R_0 B_0} \frac{\partial f}{\partial y}, \tag{2.67}$$

where B_0 is the magnitude of the toroidal magnetic field, and R_0 is the radius of curvature — usually taken as the major radius of the machine. The influence of magnetic gradients and curvature in any other terms that are not in the form of (2.67) is neglected. Using

(2.67) and (2.60), the particle density equation (2.59) in slab geometry reads

$$\frac{\partial n_e}{\partial t} + \boldsymbol{v}_E \cdot \boldsymbol{\nabla} n_e + \boldsymbol{\nabla} \cdot \left(\boldsymbol{v}_{\parallel e} n_e\right) = \frac{g n_e}{B c_s^2} \frac{\partial \varphi}{\partial y} - \frac{g}{\Omega_i} \frac{\partial n_e}{\partial y} + D \nabla_\perp^2 n_e + s_n, \tag{2.68}$$

where $g = 2c_s^2/R$ is the effective gravitational acceleration. The vorticity equation (2.64) in the slab geometry becomes

$$\frac{m_i}{B^2} \boldsymbol{\nabla}_\perp \cdot \left(n_e \frac{\mathrm{d}}{\mathrm{d}t} \boldsymbol{\nabla}_\perp \varphi \right) = \nabla_\parallel J_\parallel - \frac{eg}{\Omega_i} \frac{\partial n_e}{\partial y} + \boldsymbol{\nabla}_\perp \cdot \left(\frac{n_e m_i \nu_i \boldsymbol{\nabla}_\perp \nabla_\perp^2 \varphi}{B^2} \right). \tag{2.69}$$

At this point, it is common practice to employ what is known as the *Boussinesq approximation* in order to simplify the ion polarisation current and viscous current. In the context of classical fluid dynamics this approximation ignores density variations except where they appear in terms multiplied by gravity (e.g. Tritton, 2011). In the context of plasma dynamics, the Boussinesq approximation allows us to simplify the polarisation and viscous current terms as follows (Angus and Krasheninnikov, 2014):

$$\boldsymbol{\nabla}_\perp \cdot \left(n_e \frac{\mathrm{d}}{\mathrm{d}t} \boldsymbol{\nabla}_\perp \varphi \right) \approx n_e \frac{\mathrm{d}}{\mathrm{d}t} \nabla_\perp^2 \varphi, \qquad \boldsymbol{\nabla}_\perp \cdot \left(\frac{n_e m_i \nu_i \boldsymbol{\nabla}_\perp \nabla_\perp^2 \varphi}{B^2} \right) \approx \frac{n_e m_i \nu_i \nabla_\perp^2 \nabla_\perp^2 \varphi}{B^2}. \tag{2.70}$$

Finally, introducing the plasma vorticity $\omega = \nabla_\perp^2 \varphi / B$, equation (2.69) becomes

$$\frac{m_i n_e}{B} \frac{\mathrm{d}\omega}{\mathrm{d}t} = \nabla_\parallel J_\parallel - \frac{eg}{\Omega_i} \frac{\partial n_e}{\partial y} + \frac{n_e m_i \nu_i}{B} \nabla_\perp^2 \omega. \tag{2.71}$$

2.3.4 Three-dimensional model equations

In summary, equations (2.68), (2.71), (2.65), (2.66) describe the electrostatic drift fluid model of Easy et al. (2014, 2016). The model assumes cold ions, isothermal electrons, and the Boussinesq approximation. The geometry is simplified to a local slab with a uniform magnetic field $\boldsymbol{B} = B\hat{\mathbf{e}}_z$; the effects of magnetic curvature and inhomogeneity of B are then represented through additional effective gravity terms acting in the radial direction. Coordinates x and y represent the effective radial and poloidal directions, respectively. The system is governed by the following evolution equations for the plasma density n_e, vorticity $\omega = \nabla_\perp^2 \varphi / B$, where φ is the electrostatic potential, parallel ion velocity $v_{\parallel i}$, and parallel electron velocity $v_{\parallel e}$:

$$\frac{m_i n_e}{B} \left(\frac{\partial}{\partial t} + \boldsymbol{v}_E \cdot \boldsymbol{\nabla} + v_{\parallel i} \nabla_\parallel \right) \omega = \nabla_\parallel J_\parallel - \frac{eg}{\Omega_i} \frac{\partial n_e}{\partial y} + \frac{n_e m_i \nu_i}{B} \nabla_\perp^2 \omega, \tag{2.72}$$

$$\frac{\partial n_e}{\partial t} + \boldsymbol{v}_E \cdot \boldsymbol{\nabla} n_e + \nabla_\parallel \left(v_{\parallel e} n_e \right) = \frac{g n_e}{B c_s^2} \frac{\partial \varphi}{\partial y} - \frac{g}{\Omega_i} \frac{\partial n_e}{\partial y} + D \nabla_\perp^2 n_e + s_n, \tag{2.73}$$

$$m_e n_e \left(\frac{\partial}{\partial t} + \boldsymbol{v}_E \cdot \boldsymbol{\nabla} + v_{\parallel e} \nabla_\parallel \right) v_{\parallel e} = e n_e \nabla_\parallel \varphi - T_e \nabla_\parallel n_e + e n_e \eta J_\parallel - m_e s_n v_{\parallel e}, \tag{2.74}$$

$$m_i n_e \left(\frac{\partial}{\partial t} + \boldsymbol{v}_E \cdot \boldsymbol{\nabla} + v_{\parallel i} \nabla_\parallel \right) v_{\parallel i} = -e n_e \nabla_\parallel \varphi - e n_e \eta J_\parallel - m_i s_n v_{\parallel i}. \tag{2.75}$$

Sheath boundary conditions

In the scrape-off layer, boundary conditions need to be specified at the target plates. When ions and electrons hit a solid surface they recombine and are lost to the plasma, hence the target plates can be treated as perfect sinks of particles (Fitzpatrick, 2014). Lighter electrons generally move much faster than the heavy ions, and they are the first to arrive at the wall. The dominant flux of electrons at the wall causes it to charge up negatively, and so generate a potential barrier which repels electrons. This barrier is confined to a thin layer of plasma coating the surface of the wall and is known as a plasma sheath. Standard sheath boundary conditions on the ion and electron parallel velocities are given by (Omotani et al., 2015; Yu et al., 2006)

$$v_{\parallel i}(z = \pm l_\parallel) = \pm c_s, \tag{2.76}$$

$$v_{\parallel e}(z = \pm l_\parallel) = \pm c_s \exp\left(-\frac{e}{T_e}\varphi\right), \tag{2.77}$$

where $l_\parallel$ is the parallel SOL connection length — typically the mid-plane to target distance.

2.3.5 Two-dimensional model equations

The governing equations (2.72)—(2.75) can be simplified to a two-dimensional system by implementing a suitable closure for the current along the field lines. Two common closures are what are known as the sheath dissipation closure and the vorticity advection closure. The majority of studies invoke the sheath-limited model as it has been demonstrated to perform better than the vorticity advection closure at capturing the plasma dynamics associated with blobs (Easy et al., 2014; Riva et al., 2016). The sheath dissipation closure assumes negligible gradients of density and potential in the parallel direction and also that parallel current is regulated by the sheath boundary conditions (2.76), (2.77).

To obtain the two-dimensional set of equations we integrate equations (2.72), (2.73) along field lines between $z = -l_\parallel$ and $z = +l_\parallel$, and apply the sheath dissipation closure; we assume that density and electrostatic potential are uniform along the z–direction. We define an average over the parallel direction by

$$\langle \cdot \rangle = \frac{1}{2l_\parallel} \int_{-l_\parallel}^{+l_\parallel} \mathrm{d}z. \tag{2.78}$$

In the vorticity equation (2.72), the average of the divergence of the parallel current gives

$$\langle \hat{\boldsymbol{b}} \cdot \boldsymbol{\nabla} J_\parallel \rangle = \frac{e c_s n_e}{l_\parallel} \left(1 - \exp\left(-\frac{e}{T_e}\varphi\right)\right), \tag{2.79}$$

while the term $v_{\parallel i}\nabla_\parallel \omega$ vanishes on the assumption that ω does not vary in the parallel direction. In the continuity equation (2.73), the averaged parallel particle flux becomes

$$\langle \hat{\boldsymbol{b}} \cdot \boldsymbol{\nabla} \left(v_{\parallel e} n_e\right) \rangle = \frac{c_s n_e}{l_\parallel} \exp\left(-\frac{e}{T_e}\varphi\right). \tag{2.80}$$

The two-dimensional versions of equations (2.72), (2.73) are therefore

$$\left(\frac{\partial}{\partial t}+\boldsymbol{v}_E\cdot\nabla\right)\omega=\frac{1}{l_\parallel}c_s\Omega_i\left(1-\exp\left(-\frac{e}{T_e}\varphi\right)\right)-\frac{g}{n}\frac{\partial n}{\partial y}+\nu_i\nabla^2\omega, \tag{2.81}$$

$$\left(\frac{\partial}{\partial t}+\boldsymbol{v}_E\cdot\nabla\right)n=-\frac{1}{l_\parallel}nc_s\exp\left(-\frac{e}{T_e}\varphi\right)+\frac{gn}{Bc_s^2}\frac{\partial\varphi}{\partial y}-\frac{g}{\Omega_i}\frac{\partial n}{\partial y}+D\nabla^2 n+\frac{c_s}{l_\parallel}N(x). \tag{2.82}$$

Here, $N(x)$ is the reference density profile maintained by the source term, (Easy et al., 2014; Mendes and Bizarro, 2017) i.e.,

$$\langle s_n\rangle=\frac{c_s}{l_\parallel}N(x). \tag{2.83}$$

Under the sheath dissipation closure, the evolution is governed completely by equations (2.81) and (2.82); the equations (2.74) and (2.75) governing parallel dynamics are no longer relevant. We note that it is common practice to include only the linearised versions of the parallel closure terms (2.79), (2.80) in the two-dimensional equations (see e.g. Easy et al., 2014).

For completeness we include a description of the vorticity advection closure. The vorticity advection closure considers the two dimensional drift plane at the outboard mid-plane, under the assumption of very resistive plasma, in which parallel currents can be neglected (Krasheninnikov et al., 2008), i.e.

$$\nabla_\parallel J_\parallel\to 0. \tag{2.84}$$

This is also sometimes referred to as the inertial regime. In this closure the parallel velocites are approximated by the plasma sound speed, and the parallel advection terms are approximated as

$$v_{\parallel i}\nabla_\parallel\omega=\frac{c_s}{2l_\parallel}\omega,\qquad\qquad \nabla_\parallel\left(v_{\parallel e}n_e\right)=\frac{c_s}{2l_\parallel}n_e. \tag{2.85}$$

Under this closure, equations (2.72), (2.73) reduce to

$$\left(\frac{\partial}{\partial t}+\boldsymbol{v}_E\cdot\nabla\right)\omega=-\frac{c_s}{2l_\parallel}\omega-\frac{g}{n}\frac{\partial n}{\partial y}+\nu_i\nabla^2\omega, \tag{2.86}$$

$$\left(\frac{\partial}{\partial t}+\boldsymbol{v}_E\cdot\nabla\right)n=-\frac{c_s}{2l_\parallel}\left(n-N(x)\right)+\frac{gn}{Bc_s^2}\frac{\partial\varphi}{\partial y}-\frac{g}{\Omega_i}\frac{\partial n}{\partial y}+D\nabla^2 n, \tag{2.87}$$

where we assumed that the source term maintains the background density, i.e. $s_n\to c_s/2l_\parallel\,N(x)$.

As indicated in Chapter 1, we distinguish between single region models, which consider the dynamics in the SOL only, and two region models, which encompass both the core and the SOL. Owing to presence of the sheath dissipation terms the model composed of equations (2.81) and (2.82) is relevant for the dynamics of plasma in the region of open field lines, i.e. in the SOL region. In the core region, the field lines are closed, and hence the parallel direction can be considered periodic. Thus, on integration of (2.72), (2.73)

along the field lines all parallel terms including the source term vanish. Therefore, the equations governing plasma in the core are

$$\left(\frac{\partial}{\partial t} + \boldsymbol{v}_E \cdot \nabla\right) \omega = -\frac{g}{n}\frac{\partial n}{\partial y} + \nu_i \nabla^2 \omega, \tag{2.88}$$

$$\left(\frac{\partial}{\partial t} + \boldsymbol{v}_E \cdot \nabla\right) n = \frac{gn}{Bc_s^2}\frac{\partial \varphi}{\partial y} - \frac{g}{\Omega_i}\frac{\partial n}{\partial y} + D\nabla^2 n. \tag{2.89}$$

In Chapter 3 we will study the single region model governed entirely by equations (2.81) and (2.82). In Chapter 5 we will study the two region interaction between the core and the SOL governed by equations (2.88), (2.89), (2.81) and (2.82) together with continuity conditions at the separatrix.

2.3.6 Diffusion coefficients

The principal sources of diffusion and viscosity in a tokamak plasma are the ion-ion and ion-electron collisions. Neglecting the effect of toroidicity, collisional diffusion in plasma is described by classical expressions for the particle and momentum diffusion coefficients (Fundamenski et al., 2007):

$$D^{cl} = \left(1 + \frac{T_i}{T_e}\right)\rho_e^2 \nu_{ei}, \qquad \nu_i^{cl} = \frac{3}{4}\rho_i^2 \nu_{ii}. \tag{2.90}$$

Here, ρ_e and ρ_i are the electron and ion thermal gyroradii (recall (2.4)); ν_{ei} and ν_{ii} are the electron-ion and ion-ion collision frequencies respectively (Huba, 2006):

$$\nu_{ei} = \frac{n_e Z_i^2 e^4 \ln\Lambda}{3\varepsilon_0^2 m_e^{1/2}(2\pi T_e)^{3/2}}, \qquad \nu_{ii} = \frac{n_e Z_i^4 e^4 \ln\Lambda}{12\varepsilon_0^2 m_i^{1/2}(\pi T_i)^{3/2}}, \tag{2.91}$$

where Z_i is the ion charge state, ε_0 is the permittivity of free space, and $\ln\Lambda$ is the Coulomb logarithm:

$$\ln\Lambda = 18 - \log\left(\left(\frac{n_e}{10^{19}}\right)^{1/2}\left(\frac{T_e}{10^3 e}\right)^{-3/2}\right). \tag{2.92}$$

Note that in the cold ion limit, $T_i \to 0$, $\nu_{ii} \to \infty$ according to (2.91) and $\rho_i \to 0$ according to (2.4). Therefore, whilst the cold ions assumption is applied explicitly in the model equations, non-zero values of T_i will be used to evaluate the ion viscosity ν_i^{cl} (2.90); we will assume that ion temperature is equal to electron temperature: $T_i = T_e$. We also note that the diffusion coefficients (2.90) are evaluated using constant reference values of n_e and T_e (usually measured at the separatrix).

In the toroidal plasma the expressions for perpendicular diffusion are given by neoclassical theory. In particular, the neoclassical expressions for particle diffusivity and viscosity are given by (Fundamenski et al., 2007):

$$D^{neo} = (1 + 1.3q^2)D^{cl}, \qquad \nu_i^{neo} = (1 + 1.6q^2)\nu_i^{cl}. \tag{2.93}$$

where the quantity q is the so-called safety factor, which measures the pitch of the magnetic

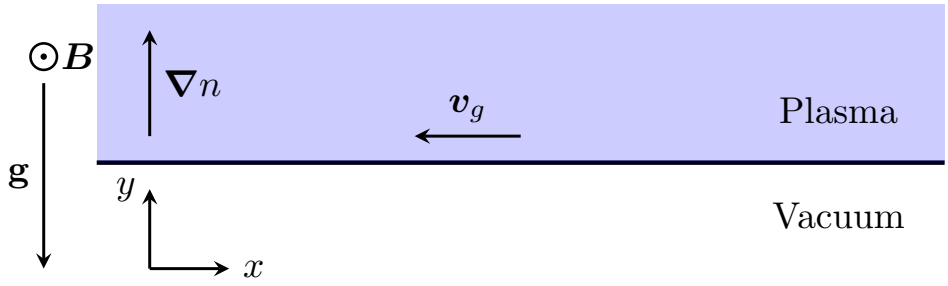

Figure 2.1: Initial configuration of a plasma surface subject to a gravitational instability.

field. The theoretical framework used to derive expressions (2.93) relies on the existence of closed field lines to obtain the effective radial diffusivities. We are however interested in the values of these diffusivities in the region of plasma edge that spans both the closed and open field line regions. Since there does not yet exist a theory of neoclassical transport on open field lines, expressions (2.93) are traditionally employed as a means of approximate treatment. On the other hand, it is conceivable that the values of transport coefficients in the SOL should lie between their classical and neoclassical values. The value of q depends on the machine (e.g. on MAST $q = 7$). Consequently, the neoclassical and classical values, and hence the diffusivities in the core and the SOL, can differ by one or two orders of magnitude. We will explore the implications of such a contrast in the values of diffusion coefficients between the two regions using an idealised model in Chapter 4.

2.4 Interchange mechanism

Having derived the *interchange* model, it is valuable to illustrate the physical mechanism behind the interchange instability. Classic plasma physics textbooks (e.g. Chen, 1984; Goldston and Rutherford, 1995) illustrate the mechanism with reference to the gravitational Rayleigh-Taylor instability. In ordinary hydrodynamics, a Rayleigh-Taylor instability arises when a heavy fluid is supported on top of a light fluid: the interface becomes "rippled", allowing the heavy fluid to fall through the light fluid. In plasmas, a Rayleigh-Taylor instability can occur when a dense plasma is supported against gravity by the pressure of a magnetic field. The physical mechanism behind the Rayleigh-Taylor instability requires the consideration of particle motions in the presence of a gravitational force.

Consider the simplest case of a plasma boundary in the x–y plane (see Figure 2.1). Let the density gradient $\boldsymbol{\nabla} n$ be in the positive vertical direction, the gravitational field $\mathbf{g}$ in the negative vertical direction. For simplicity, we furthermore assume that the plasma is isothermal and that it is supported by a uniform magnetic field pointing out of the page. In the presence of a force perpendicular to a magnetic field $\boldsymbol{B}$ – such as the gravitational

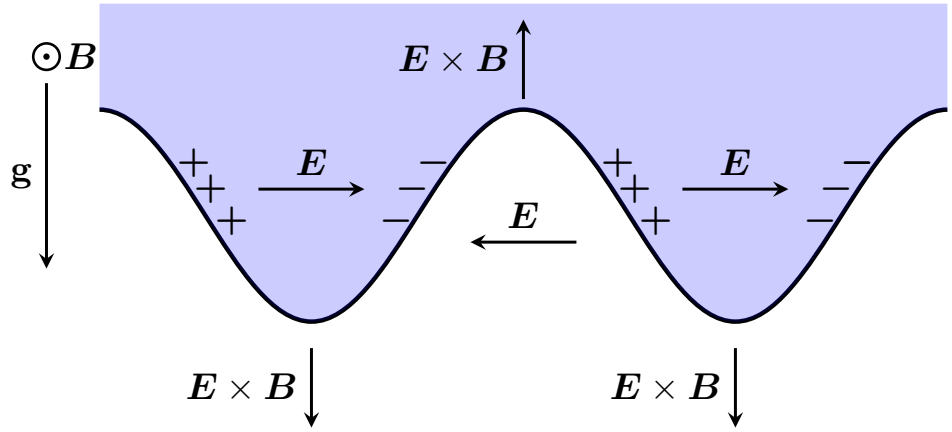

Figure 2.2: Physical mechanism of the gravitational instability.

force – a charged particle experiences a drift velocity

$$\boldsymbol{v}_g = \frac{m\mathbf{g} \times \hat{\boldsymbol{b}}}{eB}. \tag{2.94}$$

For ions, this gravitational drift is in the negative x direction, as seen in Figure 2.1. There is also an electron drift in the opposite direction, but this is much smaller because of the smaller electron mass. Suppose a small sinusoidal perturbation develops on a plasma-vacuum interface, as illustrated in Figure 2.2. The gravitational drift of ions on the plasma side of the interface will cause positive charge to build up on one side of the ripple; the depletion of ions causes a negative charge to build up on the other side of the ripple. Owing to this separation of charges, a small electric field $\boldsymbol{E}$ develops, and this electric field changes sign going from crest to trough of the perturbation. The resulting $\boldsymbol{E} \times \boldsymbol{B}$ drifts are phased so as to amplify the initial perturbation: the $\boldsymbol{E} \times \boldsymbol{B}$ drift is always upward in those regions where the interface has already moved upward, and downward in those regions where the interface has already moved downward. Thus the initial ripple is amplified causing an instability. A necessary condition for this instability is that the density gradient is in the direction opposite to the direction of gravity — in other words, that the light fluid is supporting the heavy fluid.

Although in laboratory experiments gravity does not play a big role, in curved magnetic fields, the centrifugal force on the plasma due to particle motion along the curved magnetic field lines acts as an equivalent "gravitational" force. Thus, an effective gravitational force can be used to model the effects of magnetic field curvature, with stability dependent on the sign of the curvature.

The role of curvature in the interchange instability can be demonstrated by the *shear-Alfvén law*. Consider the plasma fluid momentum equation for the centre of mass velocity $\boldsymbol{V}$:

$$\rho \frac{\mathrm{d}\boldsymbol{V}}{\mathrm{d}t} + \boldsymbol{\nabla} \cdot \Pi = -\boldsymbol{\nabla} P + \boldsymbol{J} \times \boldsymbol{B}. \tag{2.95}$$

By taking the curl of (2.95) and isolating the parallel component of the resulting equation

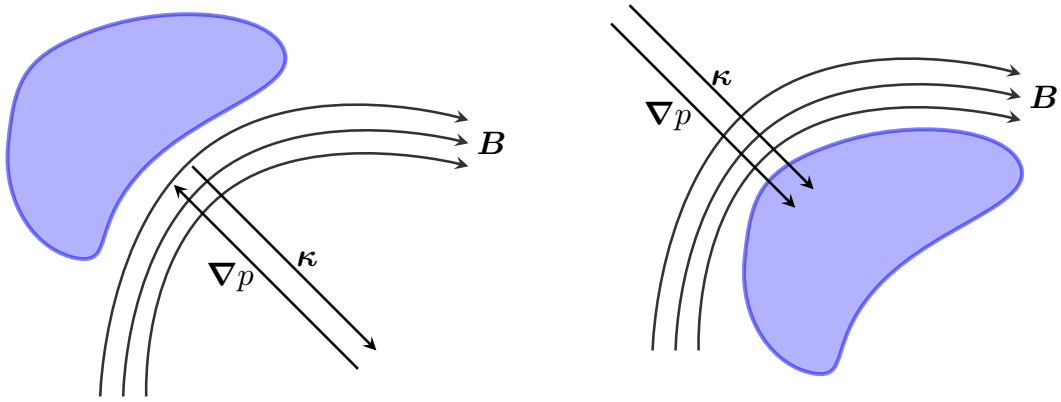

Figure 2.3: On the left, the plasma is confined on the convex side of the field lines; $\boldsymbol{\kappa} \cdot \boldsymbol{\nabla} p < 0$, thus the curvature is favourable. On the right, the pressure gradient is aligned with curvature $\boldsymbol{\kappa} \cdot \boldsymbol{\nabla} p > 0$, thus the curvature is unfavourable.

— i.e. applying $(\boldsymbol{B} \cdot \boldsymbol{\nabla} \times)$ to (2.95) — we obtain

$$\boldsymbol{B} \cdot (\boldsymbol{\nabla} \times \boldsymbol{f} - 2\boldsymbol{\kappa} \times \boldsymbol{f}) = B^2 \boldsymbol{B} \cdot \boldsymbol{\nabla} \left(\frac{J_\parallel}{B} \right) + 2\boldsymbol{B} \times \boldsymbol{\kappa} \cdot \boldsymbol{\nabla} P, \tag{2.96}$$

where $\boldsymbol{f}$ denotes the left hand side of (2.95), and $\boldsymbol{\kappa} = \hat{\boldsymbol{b}} \cdot \boldsymbol{\nabla} \hat{\boldsymbol{b}}$ is the magnetic field curvature (detailed derivation of (2.96) can be found in Appendix B). Expression (2.96) is known as the shear-Alfvén law (Hazeltine and Meiss, 2003). The left hand side describes plasma inertia. The right hand side contains the driving forces. The first term, involving the parallel current, gives rise to magnetic field line bending and current driven modes. These include the ideal kink and resistive tearing instabilities. The second term in (2.96) is called the interchange term. It is responsible for the interchange instability, an instability driven by pressure gradients in regions where the confining magnetic field is curved. Stability of an interchange mode depends on the scalar $\boldsymbol{\kappa} \cdot \nabla P$. In particular, a necessary condition for instability is $\boldsymbol{\kappa} \cdot \nabla P > 0$. Physically this means that regions of high pressure plasma are stable if they are contained within convex fields, as in the sketch shown on the left in Figure 2.3 – these are the regions of favourable curvature. On the other hand, regions of plasma contained within concave fields are the regions of unfavourable curvature and are susceptible to interchange instability. In tokamaks, the region of unfavourable curvature is on the outside of the torus; therefore unstable interchange modes tend to be localised there.

On the whole, the interchange instability is a pressure driven instability that arises when plasma is confined by an inhomogeneous magnetic field. As described above, it is somewhat similar to the overturning instability in an inversely stratified fluid subject to gravitational field. While we have illustrated this mechanism with reference to the Rayleigh-Taylor instability, we will see presently that a comparison to Rayleigh-Bénard convection is more useful. The reason is that there is an analogy between the interchange model equations (2.81), (2.82) and the equations governing two-dimensional Rayleigh-

Bénard convection. We will explore this analogy in detail in Chapter 3; immediately below we provide a short description of the convection problem drawing on the work of Chandrasekhar (1981).

2.5 Rayleigh-Bénard convection

Rayleigh-Bénard convection is a problem of thermal instability in a horizontal layer of fluid heated from below. By heating the layer of fluid from below an adverse temperature gradient is created in the layer. Thermal expansion will cause the fluid at the bottom to be lighter than the fluid at the top. Buoyancy will act to redistribute the fluid to remedy the weakness of this top-heavy configuration. This natural tendency on the part of the fluid is opposed by the stabilising effects of viscosity and thermal conductivity. When the temperature gradient across the layer is large enough, the stabilising effects are overcome by buoyancy and an overturning instability sets in as thermal convection.

The governing equations of Rayleigh-Bénard convection under the Boussinessq approximation are

$$\frac{\partial \boldsymbol{u}}{\partial t} + \boldsymbol{u}\cdot\boldsymbol{\nabla}\boldsymbol{u} = -\frac{1}{\rho_0}\boldsymbol{\nabla}p + \frac{\rho}{\rho_0}\mathbf{g} + \nu\nabla^2\boldsymbol{u}, \tag{2.97}$$

$$\boldsymbol{\nabla}\cdot\boldsymbol{u} = 0, \tag{2.98}$$

$$\frac{\partial T}{\partial t} + \boldsymbol{u}\cdot\boldsymbol{\nabla}T = \kappa\nabla^2 T, \tag{2.99}$$

$$\rho = \rho_0\left(1-\alpha\left(T-T_0\right)\right). \tag{2.100}$$

Here $\boldsymbol{u} = (u, v, w)$ is the fluid velocity, p is the pressure, ρ and T are the density and temperature; ρ_0 and T_0 are reference values of ρ and T in the fluid. ν is the kinematic viscosity, κ is the thermal diffusivity, and α is the coefficient of thermal expansion. Gravity is taken to act in the negative z direction, $\mathbf{g} = -g\hat{\mathbf{e}}_z$.

Consider a fluid layer confined between two horizontal planes at $z = 0$ and $z = d$. Boundary temperatures are fixed at T_0 on the bottom, and $T_0 - \Delta T$ on the top; the resulting temperature difference, ΔT, across the layer is the driving force for convection. It is straightforward to verify that a static ($\boldsymbol{U} = 0$) basic state with temperature depending on the vertical coordinate only satisfies:

$$T = T_0 - \frac{\Delta T}{d}z, \qquad \rho = \rho_0\left(1+\alpha\frac{\Delta T}{d}z\right), \qquad P = p_0 - \rho_0 g\left(z + \alpha\frac{\Delta T}{2d}z^2\right). \tag{2.101}$$

Here T_0, ρ_0 and p_0 are taken to be the temperature, density and pressure on the lower boundary, and $\Delta T/d$ is the temperature gradient across the layer.

Let the initial state be slightly perturbed. Let $\boldsymbol{u}$ denote the velocity in the perturbed state, θ denote the temperature perturbation and p the pressure perturbation. The con-

tinuity, momentum and temperature equations governing the perturbations read

$$\boldsymbol{\nabla} \cdot \boldsymbol{u} = 0 \tag{2.102}$$

$$\frac{\partial \boldsymbol{u}}{\partial t} + \boldsymbol{u} \cdot \boldsymbol{\nabla} \boldsymbol{u} = -\frac{1}{\rho_0} \nabla p + \alpha g \theta \hat{\mathbf{e}}_z + \nu \nabla^2 \boldsymbol{u}, \tag{2.103}$$

$$\frac{\partial \theta}{\partial t} + \boldsymbol{u} \cdot \boldsymbol{\nabla} \theta = -\frac{\mathrm{d}T}{\mathrm{d}z} w + \kappa \nabla^2 \theta. \tag{2.104}$$

We can write the equations in dimensionless form by scaling lengths with d, times with d^2/κ, pressure with $\rho_0 \kappa^2/d^2$ and temperature with ΔT. Then we obtain the following dimensionless equations

$$\boldsymbol{\nabla} \cdot \boldsymbol{u} = 0 \tag{2.105}$$

$$\frac{\partial \boldsymbol{u}}{\partial t} + \boldsymbol{u} \cdot \boldsymbol{\nabla} \boldsymbol{u} = -\nabla p + Ra\, Pr \theta \hat{\mathbf{e}}_z + Pr \nabla^2 \boldsymbol{u}, \tag{2.106}$$

$$\frac{\partial \theta}{\partial t} + \boldsymbol{u} \cdot \boldsymbol{\nabla} \theta = w + \nabla^2 \theta. \tag{2.107}$$

The two dimensionless parameters are the Rayleigh number Ra and the Prandtl number Pr, defined respectively as

$$Ra = \frac{\alpha g d^3 \Delta T}{\nu \kappa}, \qquad Pr = \frac{\nu}{\kappa}. \tag{2.108}$$

The Rayleigh number is a measure of convective driving of the system. It is a ratio of buoyancy forces that promote convection — causing hotter, lighter fluid to rise — to diffusive forces that inhibit convection — causing both heat and motion to dissipate. The Prandtl number is the ratio of the kinematic viscosity to the thermal diffusivity. For Prandtl number greater than unity, momentum will diffuse faster than heat and vice versa.

The system of governing equations is of sixth order, and therefore it requires six boundary conditions. The temperature is fixed at the boundaries. Since the basic state temperature already satisfies the required boundary conditions, the temperature perturbations must vanish on both boundaries:

$$\theta = 0 \qquad \text{at} \qquad z = 0, 1. \tag{2.109}$$

The impermeability condition states that the fluid cannot penetrate the boundaries, thus the vertical velocity mush vanish on both boundaries

$$w = 0 \qquad \text{at} \qquad z = 0, 1. \tag{2.110}$$

The boundary conditions on the horizontal components of fluid velocity depend on the nature of the bounding surface. We distinguish between *no slip* and *stress free* boundary conditions. The no slip boundary condition, also known as rigid boundary condition, requires that all components of the velocity must vanish

$$\boldsymbol{u} = (u, v, w) = 0. \tag{2.111}$$

Since this condition must be satisfied for all x and y on the surface, it follows from the incompressibility condition (2.105) that $\partial_z w = 0$ on the no slip boundary. The stress free boundary, also known as free slip, requires that tangential stress must vanish on the boundary. This condition is equivalent to the vanishing components σ_{xz} and σ_{yz} of the viscous stress tensor

$$\sigma_{xz} = \mu\left(\frac{\partial u}{\partial z} + \frac{\partial w}{\partial x}\right) = 0, \qquad \sigma_{yz} = \mu\left(\frac{\partial v}{\partial z} + \frac{\partial w}{\partial y}\right) = 0. \tag{2.112}$$

Since $w = 0$ on the bounding surface, the boundary conditions reduce to $\partial_z u = \partial_z v = 0$ on a free surface. From the incompressibility condition, differentiated with respect to z, it follows that

$$\frac{\partial^2 w}{\partial z^2} = 0 \tag{2.113}$$

on a stress free boundary. We shall restrict our attention to the case in which both bounding surfaces are stress free, as it allows an explicit solution and detailed analysis.

In the case of a two-dimensional flow in the y–z plane, we can express the velocity in terms of a streamfunction $\psi(y, z)$, such that $\boldsymbol{u} = \boldsymbol{\nabla} \times (\psi \hat{\mathbf{e}}_x) = (0, \partial_z\psi, -\partial_y\psi)$. In that case, the vorticity is $\boldsymbol{\omega} = \omega\hat{\mathbf{e}}_x$, where $\omega = -\nabla^2\psi$. This definition of velocity automatically satisfies the incompressibility condition (2.105). The evolution equation for ψ is obtained by taking the x-component of the curl of the momentum equation (2.106). The governing equations of two dimensional convection in terms of ψ and θ are thus

$$\left(\frac{\partial}{\partial t} + \boldsymbol{u}\cdot\boldsymbol{\nabla}\right)\nabla^2\psi = -RaPr\frac{\partial\theta}{\partial y} + Pr\nabla^2\nabla^2\psi, \tag{2.114}$$

$$\frac{\partial\theta}{\partial t} + \boldsymbol{u}\cdot\boldsymbol{\nabla}\theta = -\frac{\partial\psi}{\partial y} + \nabla^2\theta. \tag{2.115}$$

The boundary conditions (2.109), (2.110), (2.112) in terms of vorticity-streamfuntion variables require

$$\psi = \omega = \theta = 0 \qquad \text{at} \qquad z = 0 \qquad \text{and} \qquad z = 1. \tag{2.116}$$

The onset of convection can be determined by studying the linear stability of the system to small disturbances. We proceed by assuming the pertubations ψ and θ in (2.114), (2.115) are small, such that the nonlinear product of any two perturbation quantities is negligible. Thus we can write the linearised equations governing the perturbations:

$$\frac{\partial}{\partial t}\nabla^2\psi = -RaPr\frac{\partial\theta}{\partial y} + Pr\nabla^2\nabla^2\psi, \tag{2.117}$$

$$\frac{\partial\theta}{\partial t} = -\frac{\partial\psi}{\partial y} + \nabla^2\theta. \tag{2.118}$$

We seek normal mode solutions of the form

$$\psi = \hat{\psi}(z)\exp(iky + \sigma t), \qquad \theta = \hat{\theta}(z)\exp(iky + \sigma t), \tag{2.119}$$

where k is the wavenumber, and σ is the growth rate. On substituting into (2.117) and

(2.118) and eliminating $\hat{\theta}$ we obtain a sixth order ordinary differential equation for $\hat{\psi}$

$$\left(\mathcal{D}^2 - k^2 - \frac{\sigma}{Pr}\right)\left(\mathcal{D}^2 - k^2 - \sigma\right)\left(\mathcal{D}^2 - k^2\right)\hat{\psi} = -k^2 Ra\,\hat{\psi}, \tag{2.120}$$

where $\mathcal{D}$ denotes differentiation with respect to z. From the boundary condition $\theta = 0$ and equation (2.117) it follows that $\mathcal{D}^4\hat{\psi} = 0$ on the boundaries as well. Thus (2.120) needs to solved subject to

$$\hat{\psi} = \mathcal{D}^2\hat{\psi} = \mathcal{D}^4\hat{\psi} = 0 \qquad \text{on} \qquad z = 0, 1. \tag{2.121}$$

In fact it can be shown that all even derivatives of $\hat{\psi}$ must vanish on the boundaries. The solution that satisfies such boundary conditions is $\hat{\psi}(z) = A \sin n\pi z$, where $n \in \mathbb{N}$. Substitution into (2.120) leads to the dispersion relation

$$\left((n\pi)^2 + k^2 + \frac{\sigma}{Pr}\right)\left((n\pi)^2 + k^2 + \sigma\right)\left((n\pi)^2 + k^2\right) = k^2 Ra. \tag{2.122}$$

By the principle of exchange of stabilities, the instability for the n^{th} mode occurs when the growth rate σ passes through zero. The marginal stability curve for the n^{th} mode is thus given by the characteristic equation:

$$Ra = \frac{\left((n\pi)^2 + k^2\right)^3}{k^2}. \tag{2.123}$$

For Rayleigh numbers smaller than that given by (2.123), perturbations with wavenumber k will be stable; when the Rayleigh number exceeds the value given by (2.123), the same disturbances will be unstable. We are usually interested in the minimum, or critical, Rayleigh number for the onset of instability. Clearly the $n = 1$ mode is most readily destabilised, and the Rayleigh number reaches its minimal value for disturbances with the critical wavenumber $k = k_c = \pi/\sqrt{2}$, giving the critical Rayleigh number

$$Ra_c = \frac{27}{4}\pi^4. \tag{2.124}$$

Thus for $Ra > Ra_c$, the system is linearly unstable, whereas for $Ra < Ra_c$ the system is linearly stable.

The thermal convection problem is governed by two dimensionless parameters: the Rayleigh number and the Prandtl number, out of which only the Rayleigh number enters the criterion for the onset of instability. In the next chapter we demonstrate that the plasma problem, governed by equations (2.81) and (2.82), may be viewed as describing a thermal convection problem with additional effects. The new features include a non-uniform basic state gradient, linear damping terms, and additional advective terms. We characterize the conditions at the onset of instability and perform an extensive parameter scan to describe how the stability threshold varies as a function of plasma parameters.

Chapter 3

Linear stability analysis of the two–dimensional SOL model

3.1 Introduction

In this chapter we revisit the analogy between the instability of SOL plasma and that of Rayleigh-Bénard convection (RBC) (Berning and Spatschek, 2000; Garcia et al., 2006b; Ghendrih et al., 2003), thereby demonstrating that this analogy is not as clear-cut as previous literature has suggested. Previous considerations have restricted attention to the paradigmatic model for two-dimensional thermal convection; i.e. it is assumed from the outset that the plasma edge can be modelled using the conventional Rayleigh-Bénard equations (sometimes augmented by the inclusion of heuristic dissipation terms to account for the presence of particle sinks at the sheath of the SOL (Aydemir, 2005; Bian et al., 2003; Garcia et al., 2006a, 2005a)). As a consequence, a number of features that are relevant to the magnetized plasma problem are neglected. Here, we shall begin with the two-dimensional SOL equations and show that these can be 'naturally' reduced to a modified convection problem. An intuitive way to explore the analogy between these two systems is through the means of linear stability analysis; the linear stability properties of RBC are well understood, and it is therefore natural to ask how these stability properties change in the presence of the supplementary plasma-related features. In addition, the linear stability analysis is a valuable first step in studying complicated fluid systems, providing potentially important pointers to the nonlinear regime.

We study the linear stability of the two-dimensional fluid model for SOL plasma, described in Section 2.3.5. Although such models are fairly standard in SOL turbulence, there has been surprisingly little work exploring thoroughly their linear stability properties. Furthermore, previous linear stability calculations have either restricted attention to perturbations that are periodic in both radial (x) and poloidal (y) directions, expressing perturbations as simple Fourier modes (Mendes and Bizarro, 2017), or else have neglected the radial variation completely (Bisai et al., 2004); such treatments do not take into account the influence of boundary conditions on the stability properties. In hydrodynamics, it is well known that the choice of boundary conditions can affect both the stability properties of the system and the nature of the solutions. It is therefore of interest to begin

classifying these effects with regard to the plasma problem. In our analysis, periodicity is assumed only in the poloidal direction, while the radial extent is bounded; the radial structure of the perturbation is then determined as the solution of an eigenvalue problem. We find that, owing to the explicit x dependence of the coefficients in the problem, the radial structure of solutions can become highly localised — behaviour that cannot be recovered when the radial direction is treated as periodic. The emphasis of this study is to characterize the conditions at the onset of instability. We perform an extensive parameter scan to describe how the stability threshold varies as a function of plasma parameters.

In addition to solving the linear eigenvalue problem numerically, we use the analogy to RBC to construct a reduced linear system that allows an analytical solution; we then compare this against the solution to the full problem. We find that the reduced system provides useful insight into the qualitative behaviour of the full problem; in particular, it accurately predicts the changes to the stability threshold arising from variations of plasma parameters. Furthermore, we identify an approximate range in the parameter space for which there is good quantitative agreement between the full and reduced systems.

3.2 Mathematical formulation

3.2.1 Governing equations

We begin by recalling the equations we derived in Section 2.3.5, governing the evolution of the plasma vorticity $\omega = \nabla^2\varphi/B$ and plasma density n, given by equations (2.81) and (2.82) respectively:

$$\frac{\partial \omega}{\partial t} + \boldsymbol{v}_E \cdot \nabla\omega = \frac{1}{l_\parallel} c_s \Omega_i \left(1 - \exp\left(-\frac{e}{T_e}\varphi\right)\right) - \frac{g}{n}\frac{\partial n}{\partial y} + \nu_i \nabla^2 \omega, \tag{3.1}$$

$$\frac{\partial n}{\partial t} + \boldsymbol{v}_E \cdot \nabla n = -\frac{1}{l_\parallel} n c_s \exp\left(-\frac{e}{T_e}\varphi\right) + \frac{gn}{Bc_s^2}\frac{\partial \varphi}{\partial y} - \frac{g}{\Omega_i}\frac{\partial n}{\partial y} + D\nabla^2 n + \frac{c_s}{l_\parallel} N(x). \tag{3.2}$$

The change of variable $\theta = \log(n/n_0)$, where n_0 is a constant reference density value, allows us to recast equations (3.1) and (3.2) as

$$\frac{\partial \omega}{\partial t} + \boldsymbol{v}_E \cdot \nabla\omega = \frac{1}{l_\parallel} c_s \Omega_i \left(1 - \exp\left(-\frac{e}{T_e}\varphi\right)\right) - g\frac{\partial \theta}{\partial y} + \nu_i \nabla^2 \omega, \tag{3.3}$$

$$\frac{\partial \theta}{\partial t} + \boldsymbol{v}_E \cdot \nabla\theta = -\frac{c_s}{l_\parallel} \exp\left(-\frac{e}{T_e}\varphi\right) + \frac{g}{Bc_s^2}\frac{\partial \varphi}{\partial y} - \frac{g}{\Omega_i}\frac{\partial \theta}{\partial y} + D(\nabla^2\theta + |\nabla\theta|^2) + \frac{c_s}{l_\parallel}\exp\left(\Theta(x) - \theta\right), \tag{3.4}$$

where $\Theta(x) = \log(N(x)/n_0)$. Note that the diffusion related term $D\,|\nabla\theta|^2$ in (3.4) comes from the usual $D\nabla^2 n$ term in the density continuity equation (3.2), which transforms according to $\nabla^2 n/n = \nabla^2\theta + |\nabla\theta|^2$ upon the change of variable. At this point, subject to Bohm normalization, equations (3.3) and (3.4) are identical to equations (3a) and (3b) of Mendes and Bizarro (2017), although these authors left the source term (the last term on

the right hand side of (3.4)) unspecified.

We consider a layer of plasma bounded radially between $x = 0$ and $x = h$, where h represents the width of the scrape-off layer. The density n is fixed to $n_0 + \Delta n$ at the inner boundary, and n_0 at the outer boundary. We consider a steady basic state with plasma at rest, and assume that the basic state plasma density varies as a function only of the radial coordinate. We describe the basic state by upper case variables; thus $\Phi = 0$ and $n = N(x)$. The vorticity equation (3.3) is trivially satisfied while the log density equation (3.4) reduces to

$$\frac{\mathrm{d}^2\Theta}{\mathrm{d}x^2} + \left(\frac{\mathrm{d}\Theta}{\mathrm{d}x}\right)^2 = 0. \tag{3.5}$$

The basic state log density can thus be expressed as

$$\Theta(x) = \log\left(1 + \frac{\Delta n}{n_0}\left(1 - \frac{x}{h}\right)\right). \tag{3.6}$$

We now consider small perturbations to this basic state, expressing the potential, vorticity and density in the perturbed state by φ', ω' and $\Theta + \theta'$ respectively. On substituting these expressions into equations (3.3) and (3.4) and retaining only the lowest order terms in the perturbations, the linearised forms of the equations of motion become

$$\frac{\partial \omega'}{\partial t} = \frac{1}{l_\parallel} c_s \Omega_i \left(\frac{e}{T_e}\varphi'\right) - g\frac{\partial \theta'}{\partial y} + \nu_i \nabla^2 \omega', \tag{3.7}$$

$$\frac{\partial \theta'}{\partial t} - \frac{1}{B}\frac{\partial \varphi'}{\partial y}\frac{\mathrm{d}\Theta}{\mathrm{d}x} = \frac{c_s}{l_\parallel}\frac{e}{T_e}\varphi' + \frac{g}{Bc_s^2}\frac{\partial \varphi'}{\partial y} - \frac{g}{\Omega_i}\frac{\partial \theta'}{\partial y} + D\left(\nabla^2\theta' + 2\frac{\partial \theta'}{\partial x}\frac{\mathrm{d}\Theta}{\mathrm{d}x}\right) - \frac{c_s}{l_\parallel}\theta'. \tag{3.8}$$

Following an approach commonly used in two-dimensional simulations (Bian et al., 2003; Easy et al., 2014; Garcia et al., 2005c; Russell et al., 2009), we assume that perturbation quantities vanish on radial boundaries, i.e.

$$\varphi' = \omega' = \theta' = 0 \qquad \text{on} \qquad x = 0,\, h. \tag{3.9}$$

Periodic boundary conditions are invoked for the poloidal direction.

We now express the governing equations in dimensionless form. Non-dimensionalising x and y by h, t by the diffusive time scale h^2/D, n (and Δn) by n_0, and φ by BD, and suppressing the $'$ notation on the perturbed variables, equations (3.7) and (3.8) become

$$\frac{\partial \omega}{\partial t} = -Ra^* Pr\frac{\partial \theta}{\partial y} + Pr\nabla^2\omega + \frac{L_\perp^2 \Omega}{L_\parallel}\varphi, \tag{3.10}$$

$$\frac{\partial \theta}{\partial t} = \left(\frac{\mathrm{d}\Theta}{\mathrm{d}x} + \frac{2h}{R_c}\right)\frac{\partial \varphi}{\partial y} - \frac{Ra^* Pr}{\Omega}\frac{\partial \theta}{\partial y} + \nabla^2\theta + 2\frac{\mathrm{d}\Theta}{\mathrm{d}x}\frac{\partial \theta}{\partial x} - \frac{\Omega}{L_\parallel}\theta + \frac{L_\perp^2}{L_\parallel}\varphi, \tag{3.11}$$

where $\omega = \nabla^2\varphi$,

$$\frac{\mathrm{d}\Theta}{\mathrm{d}x} = \frac{-\Delta n}{1 + \Delta n(1 - x)}, \tag{3.12}$$

and where we have introduced the parameters

$$Ra^* = \frac{gh^3}{D\nu_i}, \qquad Pr = \frac{\nu_i}{D}, \qquad \Omega = \frac{\Omega_i h^2}{D}, \qquad L_\parallel = \frac{l_\parallel}{\rho_s}, \qquad L_\perp = \frac{h}{\rho_s}. \tag{3.13}$$

The parameter Ra^* measures the ratio of the strength of the curvature-induced gravitational force to viscous forces. It is similar to the Rayleigh number associated with buoyancy-driven flow, although this analogy is not complete since Ra^* is missing a factor describing the density difference (or temperature difference in convection) across the layer. Pr can be thought of as equivalent to the Prandtl number in the convection problem, but instead of describing the ratio of fluid viscosity to thermal diffusivity, here it represents the ratio of the ion viscosity to the particle diffusivity. Ω is the gyrofrequency divided by the time scale of diffusion. $L_\parallel$ is the normalised measure of parallel connection length, and $L_\perp$ is the normalised measure of the width of the layer.

The physical meaning of the terms in equations (3.10) and (3.11) clearly remains unchanged by this scaling. From left to right in the vorticity equation (3.10), the individual terms are linearised versions of the ion polarization current, the diamagnetic current, the current due to viscosity, and the parallel current to the sheath. In the density equation (3.11), the first term on the right hand side represents the density flux due to radial $\boldsymbol{E}\times\boldsymbol{B}$ drift velocity, with its two components corresponding to the advection of the background density distribution and the compressibility of the $\boldsymbol{E}\times\boldsymbol{B}$ drift. The second term is the density flux due to the diamagnetic drift; the third and fourth terms come from the particle diffusion term in (3.2); the last two terms are representative of parallel losses to the sheath.

3.2.2 Relation to Rayleigh-Bénard convection

The fundamental mechanism of interchange drive in boundary plasma has been compared to buoyancy drive in neutral fluids, with reference to Rayleigh-Bénard convection in particular (Berning and Spatschek, 2000; Garcia et al., 2006b; Ghendrih et al., 2003). Indeed, in their dimensionless form, equations (3.10) and (3.11) may be viewed as the equations governing the linear stability of two-dimensional Rayleigh-Bénard convection (RBC) (e.g. Chandrasekhar, 1981), but with the addition of extra terms. By this analogy, the plasma electrostatic potential and plasma vorticity correspond to the fluid streamfunction and fluid vorticity respectively, and the logarithm of plasma density corresponds to fluid temperature. Furthermore, the boundary conditions (3.9) are formally identical to stress-free, fixed temperature boundary conditions in the classical convection problem. These boundary conditions are particularly convenient in the case of the convection problem as they allow an explicit solution and detailed stability analysis.

The analogous linear convection problem that matches the boundary conditions of the original problem is governed by the equations

$$\frac{\partial \nabla^2\psi}{\partial t} = -Ra^* Pr \frac{\partial \theta}{\partial y} + Pr\nabla^2\nabla^2\psi, \tag{3.14}$$

$$\frac{\partial \theta}{\partial t} = -\log(1+\Delta n)\frac{\partial \psi}{\partial y} + \nabla^2\theta, \tag{3.15}$$

where ψ is the streamfunction, related to the velocity via $\mathbf{u} = (0, \partial_z\psi, -\partial_y\psi)$, and θ is the temperature perturbation. Equations (3.14), (3.15) govern two–dimensional motion in a plane layer; by convention the vertical direction is identified with the z coordinate. We thus identify the radial (x) direction in the plasma problem with the vertical (z) direction in the convection problem. Hence the poloidal direction in the plasma problem corresponds to the horizontal direction in the convection problem.

This analogy between the two sets of equations, along with compatible boundary conditions, motivates viewing the system (3.10), (3.11) as a modified convection problem, where the modifications can be categorized as follows. First, in RBC the basic state temperature gradient is uniform across the layer, $-\log(1+\Delta n)$. In this case, we can rescale θ further to write (3.14) and (3.15) in the standard form of RBC, namely

$$\frac{\partial \nabla^2\psi}{\partial t} = -Ra\,Pr\frac{\partial\theta}{\partial y} + Pr\nabla^2\nabla^2\psi, \tag{3.16}$$

$$\frac{\partial\theta}{\partial t} = -\frac{\partial\psi}{\partial y} + \nabla^2\theta. \tag{3.17}$$

Note now that the Rayleigh number of convection is $Ra = Ra^*\log(1+\Delta n)$. The first term on the right hand side of (3.15) represents the vertical advection of the uniform background temperature gradient. The analogous term in the plasma problem (3.11) is composed of two components; the first is the advection of the non–uniform basic state density gradient, while the other (which is representative of the effect of compressibility of the $\boldsymbol{E}\times\boldsymbol{B}$ drift) can be thought of as advection of a stabilizing uniform gradient. The second modification is that the plasma system (3.10), (3.11) includes linear damping terms, proportional to $1/L_\parallel$, which are physically representative of particle losses in the parallel direction. Finally, viewed as a modified temperature of RBC, equation (3.11) contains two additional advective terms. One corresponds to the diamagnetic drift term which acts to transport θ perturbations in the poloidal direction; the other can be interpreted as advection of θ by a spatially dependent flow that is proportional to the basic state density gradient.

As mentioned above, for the particular choice of boundary conditions, the convection problem can be solved exactly. In contrast, the presence of non-constant coefficients in the plasma problem make it particularly difficult to solve analytically. In the following section, we shall however construct a reduced system that can be solved in the same way as the RBC problem, and compare its solution to the numerical solution of the full system.

3.3 Linear stability analysis

3.3.1 Eigenvalue problem

We postulate normal mode solutions to equations (3.10) and (3.11) of the form

$$\varphi(x,y,t) = \hat{\varphi}(x)\exp(iky+\sigma t) + c.c., \tag{3.18}$$

$$\theta(x,y,t) = \hat{\theta}(x)\exp(iky+\sigma t) + c.c., \tag{3.19}$$

where $\hat{\varphi}(x)$, $\hat{\theta}(x)$ are complex eigenfunctions, k is the horizontal wave number of a particular normal mode and σ is the complex eigenvalue that determines the stability of the system. Substituting perturbations (3.18), (3.19) into equations (3.10) and (3.11) results in the linear eigenvalue problem,

$$(\mathscr{L}_1 - \sigma \mathscr{L}_2)\, \boldsymbol{S} = 0 \tag{3.20}$$

for the solution vector $\boldsymbol{S} = [\hat{\varphi}, \hat{\theta}]^\top$, where $\top$ denotes the transpose. The two linear operators $\mathscr{L}_1$ and $\mathscr{L}_2$ are defined by

$$\mathscr{L}_1 = \begin{bmatrix} Pr\left(\mathcal{D}^2 - k^2\right)^2 + \dfrac{L_\perp^2\,\Omega}{L_\parallel} & -ik\,Ra^*Pr \\ ik\left(\dfrac{\mathrm{d}\Theta}{\mathrm{d}x} + \dfrac{2h}{R_c}\right) + \dfrac{L_\perp^2}{L_\parallel} & -\dfrac{Ra^*Pr}{\Omega}ik + \left(\mathcal{D}^2 - k^2\right) + 2\dfrac{\mathrm{d}\Theta}{\mathrm{d}x}\mathcal{D} - \dfrac{\Omega}{L_\parallel} \end{bmatrix}, \tag{3.21}$$

$$\mathscr{L}_2 = \begin{bmatrix} \left(\mathcal{D}^2 - k^2\right) & 0 \\ 0 & 1 \end{bmatrix}, \tag{3.22}$$

and the boundary conditions for $\hat{\varphi}$ and $\hat{\theta}$ are given by

$$\hat{\varphi} = \mathcal{D}^2\hat{\varphi} = \hat{\theta} = 0 \qquad \text{at} \qquad x = 0,\, 1. \tag{3.23}$$

Here the operator $\mathcal{D}$ represents differentiation with respect to x of the perturbed variables.

The eigenvalue problem (3.20) must be solved numerically; we employ MATLAB's `bvp4c` routine for solving boundary value problems. We address the problem of marginal stability: thus, for each wavenumber k, we seek the density difference Δn for which $Re(\sigma) = 0$. Furthermore, the critical density difference Δn_c is defined as the minimum value of Δn at the onset of instability, with the critical wavenumber k_c being the wavenumber at which that minimum is attained. Note that eqns. (3.20)–(3.23) shall be referred to as the *full* problem, to be distinguished from the *reduced* problem, which we shall introduce in Section 3.3.3. Immediately below, we discuss the range of dimensionless parameter values used for these numerical investigations.

3.3.2 Parameters

In general, the dimensional parameters in the plasma edge vary from one discharge to another. Thus, rather than stating precise values of the physical parameters, we shall concern ourselves with representative, order-of-magnitude estimates; the following estimates are broadly relevant for the L-mode scrape-off layer in a medium size tokamak. We take estimates for the magnetic field $B \approx 1\,\mathrm{T}$, and the radius of curvature $R_c \approx 1\,\mathrm{m}$ (Easy et al., 2014). The width of the SOL, h, is typically estimated to be several centimetres (certainly not greater than 0.1 m), and the parallel connection length $l_\parallel \approx 10\,\mathrm{m}$. For a typical discharge, the edge values for temperature and density are found experimentally to be $T_e \approx 10\,\mathrm{eV}$, $n_e \approx 10^{18}\,\mathrm{m}^{-3}$ (Militello et al., 2016). Using appropriate formulae (outlined in Chapter 2), these give reasonable estimates for the sound speed c_s, the effective gravitational acceleration g, the gyro-radius ρ_s, and the gyrofrequency Ω_i. The matter of

Table 3.1: Range of dimensionless parameters.

Ra^*	10^5 — 10^{12}
Pr	10^{-4} — 1
Ω	10^5 — 10^8
$L_\perp$	55
$L_\parallel$	5500

estimating appropriate values of conduction and viscous coefficients on the other hand is far more ambiguous. Depending on the choice of classical (Braginskii, 1965) or anomalous values (implied by empirical scaling laws (Goldston, 1984)), the particle diffusivity D can range between 10^{-3} and 1, while the ion viscosity ν_i can range between 10^{-4} and 1. Hence it seems that physics uncertainty alone implies that Pr can range from 10^{-4} to 1, and Ra^* from 10^5 to 10^{12}; similarly, Ω can range between 10^5 and 10^8. This uncertainty in the values of the dimensionless parameters is summarised in Table 3.1. We focus on the effect of varying Ra^* and Pr, as the uncertainty in these is greatest, and fix $\Omega = 10^5$, $L_\parallel = 5500$, $L_\perp = 55$, $2h/R_c = 0.04$.

3.3.3 Reduced linear system

In the analogous convection problem (3.16), (3.17), with stress-free, fixed temperature boundary conditions (equivalent to (3.9)), the solutions take the simple sinusoidal form $\psi, \theta \sim \sin m\pi z \exp(\sigma t + iky)$, where m is an integer (cf. Chandrasekhar (1981)). The condition for marginal stability is then given by

$$Ra = \frac{\left(m^2\pi^2 + k^2\right)^3}{k^2}. \tag{3.24}$$

Owing to the explicit x dependence of the coefficients in the plasma problem, governed by (3.10) and (3.11), simple Fourier modes can no longer be adopted. Hence, to make progress analytically, we construct a reduced linear problem to (3.10), (3.11) by extending the Rayleigh–Bénard problem as far as we can whilst retaining the simplicity of its solutions. To this end, we replace the non-uniform basic state gradient in the first term on the right hand side of (3.11) by $-\log(1+\Delta n)$, and we omit the term $2\Theta'\partial_x\theta$ completely. The resulting reduced system is

$$\frac{\partial \omega}{\partial t} = -Ra^* Pr \frac{\partial \theta}{\partial y} + Pr\nabla^2\omega + \frac{L_\perp^2 \Omega}{L_\parallel}\varphi, \tag{3.25}$$

$$\frac{\partial \theta}{\partial t} + \frac{Ra^* Pr}{\Omega}\frac{\partial \theta}{\partial y} = -\left(\ln(1+\Delta n) - \frac{2h}{R_c}\right)\frac{\partial \varphi}{\partial y} + \nabla^2\theta + \frac{L_\perp^2}{L_\parallel}\varphi - \frac{\Omega}{L_\parallel}\theta. \tag{3.26}$$

Note that such a system would arise naturally if we neglect the diffusion related term $D\left|\nabla\theta\right|^2$ in equation (3.4). The basic state log density would then be linear, given by the solution of $\Theta'' = 0$, and the basic state gradient would be spatially uniform with $\Theta' = -\ln(1+\Delta n)$. The dimensionless perturbation equations in such a case would then be precisely (3.25) and (3.26). In contrast to the simple Rayleigh-Bénard problem, the

principle of exchange of stabilities is not valid, and the marginal state is characterised by a non-zero frequency of oscillation. Combining equations (3.25) and (3.26) into an equation for φ, and substituting the ansatz $\varphi = \mathcal{A}\sin(m\pi x)\exp(i\gamma t + iky)$, where $\gamma \in \mathbb{R}$, yields the dispersion relation

$$\left(i\gamma\Delta_k + Pr\Delta_k^2 + \frac{L_\perp^2\,\Omega}{L_\parallel}\right)\left(i\gamma + ik\frac{Ra^*Pr}{\Omega} + \Delta_k + \frac{\Omega}{L_\parallel}\right) = Ra^*Pr\left(ik\frac{L_\perp^2}{L_\parallel} + k^2\Delta\Theta\right), \tag{3.27}$$

where $\Delta_k = m^2\pi^2 + k^2$, and $\Delta\Theta = (\ln(1+\Delta n) - 2h/R_c)$. The imaginary part of (3.27) gives the frequency at onset:

$$\gamma = -k\Delta_k^2\left(\frac{Ra^*Pr^2}{\Omega}\right)\left[(1+Pr)\Delta_k^2 + \frac{\Omega}{L_\parallel}\left(\Delta_k + L_\perp^2\right)\right]^{-1}, \tag{3.28}$$

and the real part gives the stability threshold:

$$Ra^*\Delta\Theta = \frac{1}{k^2}\left(\Delta_k^2 + \frac{L_\perp^2\,\Omega}{L_\parallel Pr}\right)\left(\Delta_k + \frac{\Omega}{L_\parallel}\right) + \Delta_k^3\left(\frac{Ra^*Pr}{\Omega}\right)^2\frac{\Delta_k^2 + \frac{\Omega}{L_\parallel}\left(\Delta_k + L_\perp^2\right)}{\left[(1+Pr)\Delta_k^2 + \frac{\Omega}{L_\parallel}\left(\Delta_k + L_\perp^2\right)\right]^2}. \tag{3.29}$$

On inspection of expression (3.29), several features may be observed. First, we note that contained within expression (3.29), though slightly obscured, is the stability threshold of convection, Δ_k^3/k^2 (i.e. expression (3.24)); it can be revealed by multiplying out the brackets in the first term on the right hand side of (3.29). It follows, since all of the dimensionless parameters are positive, that the reduced plasma problem is more stable than the convection problem. Furthermore, unlike for the convection problem, here both the onset of instability as well as the critical wavenumber are dependent on the Prandtl number Pr (as well as on all the other parameters). Next, we observe the stabilizing effect of the compressible $\boldsymbol{E}\times\boldsymbol{B}$ drift, defining a lower bound for the marginal stability threshold, $\ln(1+\Delta n) > 2h/R_c$, consistent with previous literature (Ref. Garcia (2001)). Finally, we remark on the implications of the presence of the Ra^{*2} term on the right hand side of (3.29). Recall that in the analogous convection problem (cf. (3.14), (3.15)), the threshold for instability is given by expression (3.24) (where $Ra = Ra^*\ln(1+\Delta n)$); hence, increasing Ra^* always results in decreasing the marginal stability threshold, and thus an increasingly more unstable system. Here, on the other hand, the situation becomes more subtle: for large enough Ra^*, increasing Ra^* will result in increasing the density difference at the onset of instability, and thus a more stable system; this has also been observed by Mendes and Bizarro (2017). This stabilizing effect at large Ra^* is ultimately due to the inclusion of the curvature term due to the diamagnetic drift in the density continuity equation (3.2). Indeed, it is known that interchange-driven models of SOL plasma that do not include this curvature term in the density equation become more unstable with increasing curvature drive (here represented by Ra^*) (e.g. Refs. Aydemir (2005); Ghendrih et al. (2003)).

We can illustrate this point by referring back to the analogy with the simple RBC

system (cf. eqns. (3.14), (3.15)). In RBC, the ψ and θ cells are arranged with respect to each other in a way that is most favorable for instability; i.e. there is a preferred phase difference between the ψ and θ cells. Let us now consider the effect of adding the diamagnetic drift term $((Ra^* Pr/\Omega)\partial_y \theta)$ to the right hand side of the temperature equation (3.15). Such a term represents advection of the temperature perturbation in the y-direction by a uniform flow (whose magnitude is proportional to Ra^*). Crucially, however, this flow acts only on the temperature and not on the vorticity; it thus shifts the phase relation between the θ and ψ cells away from the preferred configuration, and therefore has a stabilizing effect. Furthermore, this stabilizing influence will become stronger as Ra^* is increased. We expect the same mechanism to be responsible for the stabilization at large values of Ra^* in the case of the plasma problem.

3.4 Characteristics of the instability

3.4.1 Comparison between the full and reduced systems

Figures 3.1a and 3.1b show, respectively, the critical density difference Δn_c and the corresponding critical wavenumber k_c at the onset of instability. For comparison, dashed lines indicate Δn_c and k_c of the reduced system, in this case obtained by minimizing the expression for marginal stability (3.29) with respect to the wavenumber. Before comparing the two systems, let us briefly comment on the effect of varying Ra^* and Pr on the stability threshold in the full system. The critical density curves (Fig. 3.1a) have a roughly parabolic shape for all values of Pr: as Ra^* is increased, Δn_c is reduced until it reaches a minimum, after which further increase of Ra^* leads to an increase in Δn_c. Unlike in the case of Rayleigh-Bénard convection, here the onset of instability is Pr dependent. Reducing Pr shifts the critical density curves to increased values of Ra^*; i.e. for smaller Pr, the location of the minimum of Δn_c occurs at higher Ra^*. Furthermore, the span of the trough between the two tails of each curve widens as Pr is decreased. The critical wavenumber (Fig. 3.1b) decreases with Ra^*, but the rate at which it decreases varies with Ra^*; broadly speaking, the gradient of this decrease becomes steeper with increasing Ra^*. Furthermore, reducing Pr for a given Ra^* increases the critical wavenumber.

Overall, we observe a remarkable agreement between the stability properties of the full system and those of the reduced system. Figure 3.2 shows the relative differences in the critical density difference and the critical wavenumber in the two systems. For each value of Pr, there exists a range of Ra^* values within which the critical density gradient and critical wavenumber of the reduced system are good approximations to their counterparts in the full system. These regions of agreement are characterised by low values of Δn_c, and therefore a basic state gradient that is close to uniform. Figure 3.3 shows the real and imaginary parts of the eigenfunctions of the full system in these circumstances; it can be seen that the radial structure of the dominant real part closely resembles that of the sinusoidal solutions of the reduced, constant coefficient system. Outside the ranges of agreement, the inhomogeneity of the basic state gradient becomes more pronounced, with the terms that were ignored in constructing the reduced system becoming significant

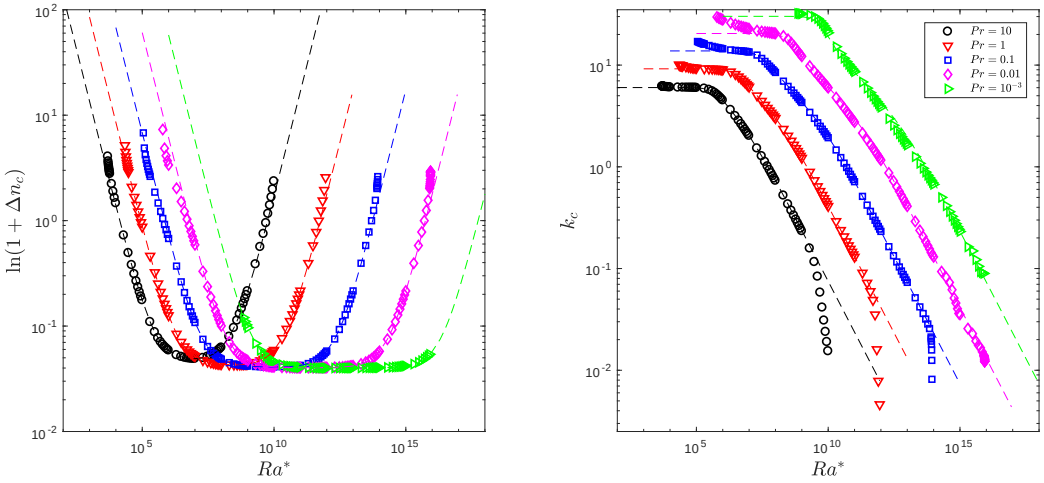

(a) (b)

Figure 3.1: Variation of (a) the critical density difference Δn_c, and (b) the corresponding critical wavenumber k_c, versus Ra^*. Markers: full system; dashed lines: reduced system.

in influencing the stability threshold and the structure of the solutions. In particular, when Δn_c becomes very large, the eigenfunctions develop sharp gradients near $x = 1$, characteristic of a boundary layer problem. This will be discussed in more detail below (see Section 3.4.3).

Perhaps unsurprisingly, the agreement between the full and reduced systems begins to break down when Δn_c grows to order unity, or, equivalently, in the limits of small and large Ra^*, though the precise meaning of 'small' and 'large' Ra^* is dependent on the value of Pr. We shall attempt to elucidate those meanings in the following sections. In both the full and reduced systems, the critical density difference Δn_c grows indefinitely in the limits of small and large Ra^*. For small Ra^*, the critical wavenumber in the reduced system tends to a constant value that is dependent on Pr. In the full system, on the other hand, as Ra^* is reduced, k_c appears to grow indefinitely. In the opposite limit, as Ra^* is increased, the critical wavenumber decreases towards zero faster in the full system than in the reduced system.

3.4.2 Properties of the reduced system

In this section we study the variation with Ra^* of the critical value of Δn and of the corresponding critical k in the reduced system. Through this investigation we will attempt to estimate the range of Ra^* for which there is good agreement between the stability thresholds of the full and reduced systems. As observed above, agreement between the two systems is good provided that the density difference is small — in particular when $\ln(1 + \Delta n_c) < 1$. By considering the behaviour of the critical density threshold in the reduced system, we can approximate the values of Ra^* at which the agreement breaks down, i.e. when $\ln(1 + \Delta n_c)$ exceeds unity.

Recall that the critical density difference Δn_c in the reduced system is obtained by

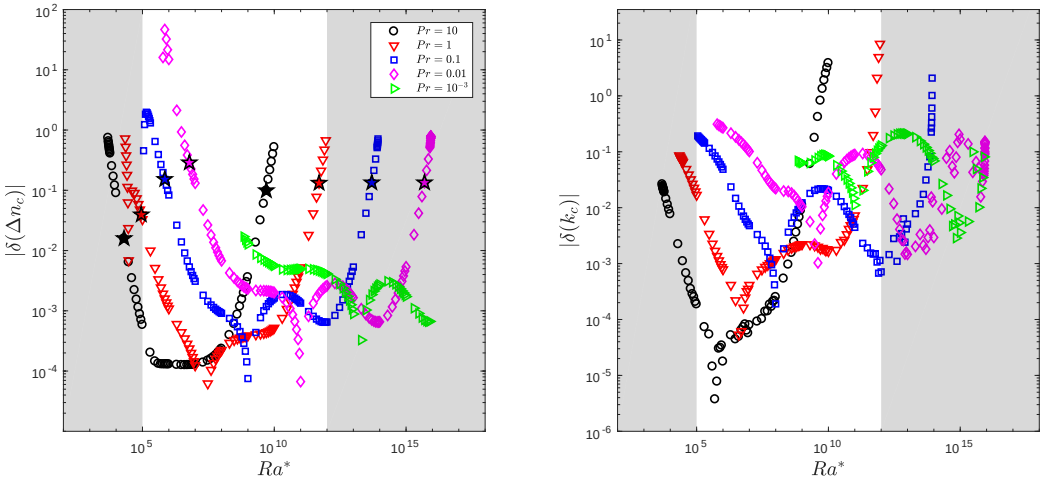

(a) (b)

Figure 3.2: Relative difference between the full and reduced systems for (a) the critical density difference Δn_c, and (b) the corresponding critical wavenumber k_c. Starred markers in (a) indicate the beginning and the end of the range of Ra^* for which $\ln(1 + \Delta n) < 1$. Shaded areas indicate the parameter space outside the range of interest, specified in Table 3.1.

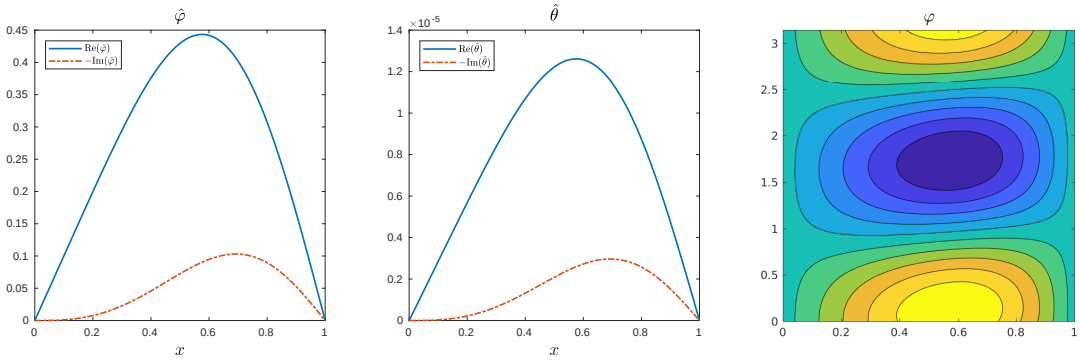

Figure 3.3: Radial eigenfunction profiles $\hat{\varphi}(x)$, $\hat{\theta}(x)$, and the resulting convective cell $\varphi(x, y)$ for $Ra^* = 10^{10}$, $Pr = 0.1$.

minimizing (3.29) with respect to k. On differentiating (3.29) with respect to k^2 and setting the result to zero, we find that the critical wavenumber satisfies the following equation:

$$\left[(2k^2-\pi^2)\Delta_k^2+\frac{\Omega}{L_\parallel}(k^2-\pi^2)\Delta_k-\pi^2\frac{L_\perp^2\Omega}{L_\parallel Pr}-\frac{1}{Pr}\left(\frac{L_\perp\Omega}{L_\parallel}\right)^2\right] + k^4\left(\frac{Ra^*Pr}{\Omega}\right)^2\xi\left(k,Pr,\Omega,L_\perp,L_\parallel\right)=0, \quad (3.30)$$

where

$$\xi\left(k,Pr,\Omega,L_\perp,L_\parallel\right)=\frac{\Delta_k^2\left[(1+Pr)\Delta_k^2+\frac{\Omega}{L_\parallel}(\Delta_k+L_\perp^2)\right]\left[5\Delta_k^2+\frac{\Omega}{L_\parallel}(4\Delta_k+3L_\perp^2)\right]\ldots -2\Delta_k^3\left[2(1+Pr)\Delta_k+\frac{\Omega}{L_\parallel}\right]\left[\Delta_k^2+\frac{\Omega}{L_\parallel}(\Delta_k+L_\perp^2)\right]}{\left[(1+Pr)\Delta_k^2+\frac{\Omega}{L_\parallel}(\Delta_k+L_\perp^2)\right]^3}. \quad (3.31)$$

Attempting to extract an analytical solution for k_c is a hopeless task, but we can gain useful insight by considering the limits of small and large Ra^*.

Behaviour at small Ra^*

When the factor $(Ra^*Pr/\Omega)^2$ in equation (3.30) is sufficiently small, the critical value k_c becomes independent of Ra^*, and can be approximated by a solution of

$$(2k^2-\pi^2)\Delta_k^2+\frac{\Omega}{L_\parallel}(k^2-\pi^2)\Delta_k-\pi^2\frac{L_\perp^2\Omega}{L_\parallel Pr}-\frac{1}{Pr}\left(\frac{L_\perp\Omega}{L_\parallel}\right)^2=0. \quad (3.32)$$

Provided that Ω/Pr is large (which is to be expected), dominant balance dictates that

$$k_c^6\sim\frac{1}{2Pr}\frac{L_\perp^2\Omega}{L_\parallel}\left(\pi^2+\frac{\Omega}{L_\parallel}\right). \quad (3.33)$$

Figure 3.4b shows that the dominant balance estimate for k_c and the true solution of (3.30) are in good agreement, and that the agreement improves for smaller values of Pr. We note also that for each value of Pr the true solution curves begin to deviate from the approximations only when the factor $(Ra^*Pr/\Omega)^2$ grows to $\mathcal{O}(10^2)$.

Using (3.33) in (3.29) gives the following scaling for the critical density difference Δn_c in the small Ra^* limit,

$$Ra^*\log(1+\Delta n_c)\sim\frac{1}{Pr}\frac{L_\perp^2\Omega}{L_\parallel}+\left(\frac{\sqrt{2}L_\perp^2\Omega}{L_\parallel Pr}\left(\pi^2+\frac{\Omega}{L_\parallel}\right)\right)^{2/3}. \quad (3.34)$$

This estimate is compared to the true variation of Δn_c in Figure 3.4a; again we observe good agreement between the two results, especially when Pr is small. For completeness, we need to provide some appropriate interpretation of what 'small' Ra^* means in this context. In this matter we adopt a pragmatic approach. Bearing in mind that we are

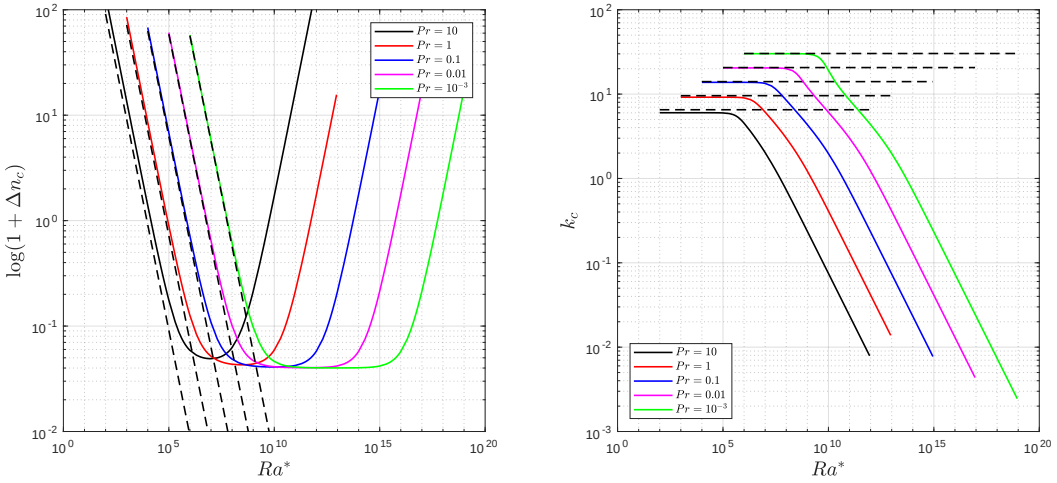

(a) (b)

Figure 3.4: Scaling behaviour at small Ra^*. (a) Variation of k_c as given by solution of (3.30) (solid lines) and the approximation (3.33) (dashed lines). (b) Variation of Δn_c given by solution of (3.29) (solid lines) and the approximation (3.34) (dashed lines).

interested in conditions for which $\ln(1+\Delta n_c) \approx 1$, and observing that the curves and the scalings in Figure 3.4a indeed align when $\ln(1+\Delta n)$ is above unity, from (3.34) we estimate that Ra^* can be considered 'small' if

$$Ra^* \lesssim \frac{1}{Pr}\left(\frac{L_\perp^2\Omega}{L_\parallel}\right) + \frac{\sqrt[3]{2}}{Pr^{2/3}}\left(\frac{L_\perp^2\Omega}{L_\parallel}\left(\pi^2 + \frac{\Omega}{L_\parallel}\right)\right)^{2/3}. \tag{3.35}$$

Behaviour at large Ra^*

When Ra^* becomes large, the last term in (3.30) would appear to dominate, suggesting that k_c is a root of $\xi\left(k, Pr, \Omega, L_\perp, L_\parallel\right) = 0$, with ξ defined in (3.31). However, for the parameter values under consideration, we found that this equation has no roots. Consequently, the large Ra^{*2} term in (3.30) has to be balanced by other terms in that equation. We therefore expect the dominant balance to be given by

$$\frac{\pi^2}{Pr}\frac{L_\perp^2\Omega}{L_\parallel} + \frac{1}{Pr}\left(\frac{L_\perp\Omega}{L_\parallel}\right)^2 \sim 3\pi^4 k^4 \left(\frac{Ra^* Pr}{\Omega}\right)^2 \left(\frac{L_\perp^2\Omega}{L_\parallel}\right)^{-1}, \tag{3.36}$$

which leads to the scaling

$$k_c \sim \left(\frac{L_\perp^4\Omega^4}{3\pi^4 L_\parallel^2}\left(\pi^2 + \frac{\Omega}{L_\parallel}\right)\right)^{1/4} Ra^{*-1/2} Pr^{-3/4}. \tag{3.37}$$

Using this estimate for k_c in (3.29) gives the scaling for the critical density Δn_c at large Ra^*,

$$\log(1+\Delta n_c) \sim \frac{\pi^6 L_\parallel}{L_\perp^2\Omega^3} Ra^* Pr^2. \tag{3.38}$$

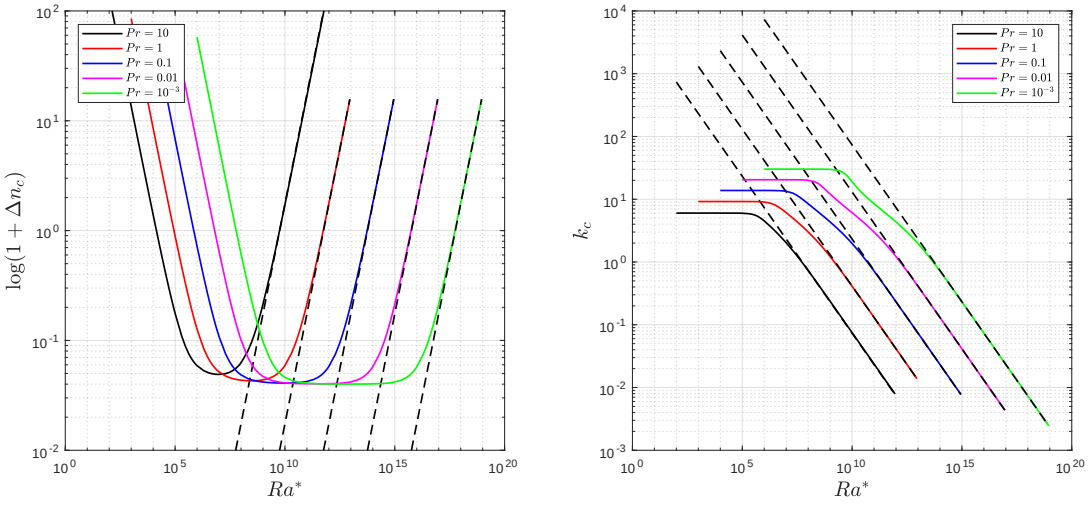

(a) (b)

Figure 3.5: Scaling behaviour at large Ra^*. (a) Variation of k_c as given by solution of (3.30) (solid lines) and the approximation (3.37) (dashed lines). (b) Variation of Δn_c given by solution of (3.29) (solid lines) and the approximation (3.38) (dashed lines).

Figures 3.5a and 3.5b compare estimates (3.37) and (3.38) with the true values obtained from numerical solution of the full system (3.20). In both cases the agreement is remarkable, given the simplicity of the scalings and the complexity of the true solution. As for the case of small Ra^*, we again observe that the true Δn_c curves match their respective scalings when $\log(1+\Delta n_c)$ exceeds unity. We may therefore estimate from (3.38) that the 'large' Ra^* regime is defined by

$$Ra^* \gtrsim \frac{L_\perp^2 \Omega^3}{\pi^6 L_\parallel} Pr^{-2}. \tag{3.39}$$

Implications for the behaviour of the full system

Once we have identified the regions of small and large Ra^*, can we safely say that outside these regions the reduced system is a good approximation to the full system? The best answer we can offer is 'tentatively'. We would certainly expect the agreement to break down when the terms unaccounted for by the reduced system (related to Δn) grow in magnitude to order unity (i.e. when $\ln(1 + \Delta n) > 1$). Furthermore, the relative error between the stability boundaries in the two systems remains below acceptable levels within these ranges (recall Figure 3.2a). However, we cannot ignore the general trend of the error curves in Figure 3.2a to shift upwards as Pr is reduced. It is plausible that for values of Pr smaller than those investigated here, the window of agreement between the two systems could shrink. Nonetheless, for the range of Pr values of interest (see Table 3.1), the estimates of small and large Ra^* can be used as approximate lower and upper bounds of Ra^* between which the reduced system is a good predictor of the behaviour in the full system. Finally, we can comment briefly on the behaviour of the full system in the limit of large Ra^*. Although we are not able to extract any precise scaling for the behaviour

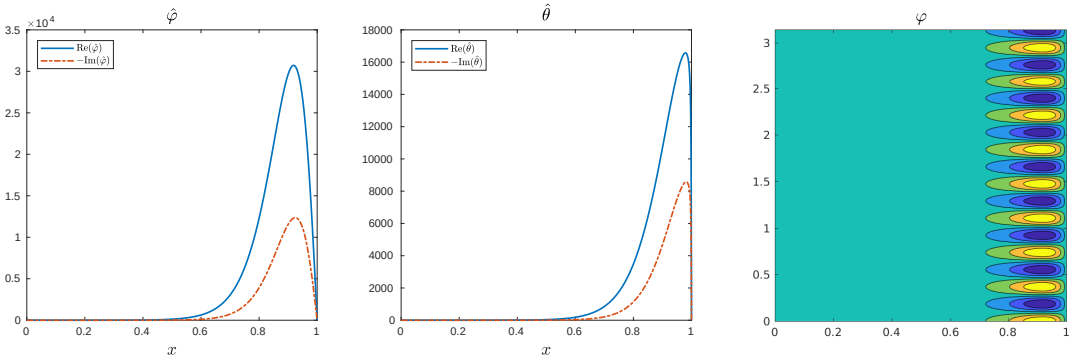

Figure 3.6: Radial eigenfunction profiles $\hat{\varphi}(x)$, $\hat{\theta}(x)$, and the resulting convective cell $\varphi(x, y)$ for $Ra^* = 1.1 \times 10^5$, $Pr = 0.1$ (the imaginary part of the eigenfunction has been multiplied by 100).

of the critical wavenumber in the full system, we can conclude, by comparison with the reduced system, that for large Ra^*, k_c decays faster than $Ra^{*-1/2}$. Furthermore, the rate of this decay increases as Pr is decreased.

3.4.3 Beyond the reduced system — a boundary layer problem

Recall from Figure 3.1a that Δn_c increases indefinitely in the limits of very small or very large Ra^*. As Δn_c grows, the inhomogeneity of the basic state gradient becomes more marked. In particular, as $\Delta n_c \to \infty$, $\Theta' \to -(1-x)^{-1}$: thus the basic state gradient develops a singularity at $x = 1$. Consequently, the φ and θ eigenfunctions develop sharp gradients near $x = 1$, as shown in Figure 3.6. This behaviour is characteristic of a boundary layer problem. Although solution of the boundary layer problem lies beyond the scope of this paper, here we demonstrate, through fairly simple means, that it is possible to extract the inner boundary layer solution, and to verify that it is consistent with numerically obtained solutions of the full system.

We consider the log density equation (3.8) expressed in normal mode form:

$$\sigma\theta = \left(\frac{\mathrm{d}\Theta}{\mathrm{d}x} + \frac{2h}{R_c}\right) ik\varphi - i\frac{Ra^*\,Pr}{\Omega}k\theta + (\mathcal{D}^2\theta - k^2\theta) + 2\frac{\mathrm{d}\Theta}{\mathrm{d}x}\mathcal{D}\theta - \frac{\Omega}{L_\parallel}\theta + \frac{L_\perp^2}{L_\parallel}\varphi. \tag{3.40}$$

Suppose that there is a boundary layer near $x = 1$, where gradients in x are large. Let $\varepsilon \ll 1$ be the ordering parameter, with the only ordering assumption being that derivatives in x are large, with $\mathrm{d}/\mathrm{d}x \sim \mathcal{D} \sim 1/\varepsilon$. It then follows from (3.40) that the dominant balance inside the boundary layer, at $\mathcal{O}\left(1/\varepsilon^2\right)$, is governed by the ordinary differential equation:

$$0 = \mathcal{D}^2\theta_{in} + 2\frac{\mathrm{d}\Theta}{\mathrm{d}x}\mathcal{D}\theta_{in}. \tag{3.41}$$

This can be integrated to obtain

$$\mathcal{D}\theta_{in} = A\exp(-2\Theta(x)) = A\left(1 + \Delta n(1-x)\right)^{-2}. \tag{3.42}$$

In Figure 3.7, we compare numerically obtained solutions for $\mathcal{D}\theta$ to the proposed inner

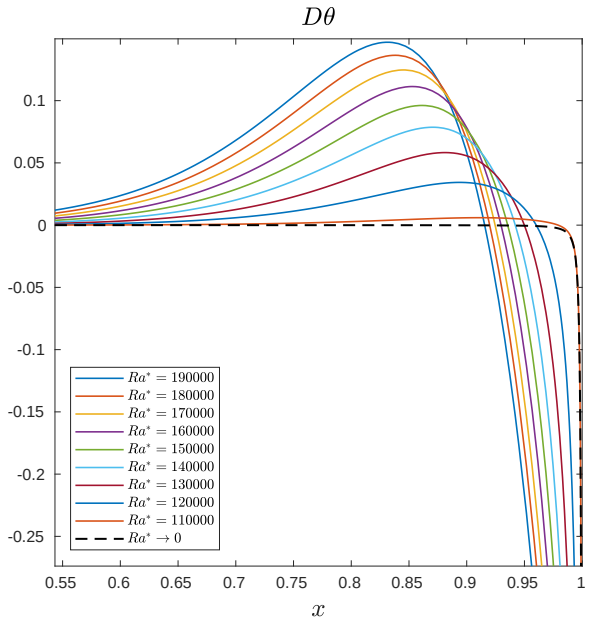

Figure 3.7: Boundary layer behaviour at small Ra^*, $Pr = 0.1$. Solid lines are numerical solutions of $\mathcal{D}\theta$ for a range of decreasing Ra^*. The dashed line is the inner boundary layer solution (3.42) (evaluated with Δn_c matching that of the numerical solution with lowest Ra^*). All profiles have been normalised by $\mathcal{D}\theta(x = 1)$.

boundary layer solution (3.42) for a range of decreasing Ra^*. It can be seen that the numerical solutions tend to the profile given by (3.42). This provides evidence that for very large Δn, the linear SOL equations have the nature of a boundary layer problem.

3.5 Discussion

In this chapter, we have pursued two closely related objectives. The first is an in-depth linear stability analysis of a two-dimensional fluid model often used to study SOL dynamics. In this regard, we focus on characterizing the conditions at the onset of instability. Specifically, we calculate the stability threshold and investigate its dependence on various plasma parameters. Although the parameter estimates are based on the SOL conditions relevant to medium sized tokamaks, increasing the plasma density and temperature to values characteristic of larger tokamaks (e.g. $n_e \approx 10^{19}\,\mathrm{m}^{-3}$, $T_e \approx 50\,\mathrm{eV}$) still yields values of Ra^* and Pr within the range considered here (Table 3.1).

At the same time, we revisit, and explore further, the analogy between the SOL plasma problem and Rayleigh-Bénard convection in neutral fluids. In this respect, we demonstrate that the SOL plasma equations can indeed be reduced to those describing thermal convection with additional effects, in which analogues of the dimensionless Rayleigh and Prandtl numbers can be identified. The presence of these additional terms, however, makes the analogy not entirely straightforward: indeed the SOL stability problem differs markedly from that of Rayleigh-Bénard convection in three important respects.

First, the Rayleigh number Ra^* makes an explicit appearance in two terms in the

SOL system. One is in the interchange drive term in the vorticity equation, which is a direct analogue of the buoyancy term responsible for driving the instability in the case of thermal convection; this term is therefore understood to be destabilizing. In the convection problem, increasing Ra^* results in lowering the critical density threshold and thus an increasingly more unstable system. In the SOL problem, however, Ra^* also appears in the density continuity equation in the term representing density flux due to diamagnetic drift; this term has a stabilizing effect, and will thus compete with the destabilizing effect of the interchange drive term. Overall, increasing Ra^* will initially have a destabilizing effect up to a certain point, beyond which any further increase in Ra^* will be stabilizing.

Second, we observe that the stability threshold is Prandtl number dependent, unlike in the case of RBC. As can be seen in Figure 3.1a, this dependence is not straightforward: at small enough Ra^* the critical density difference required for the onset of instability decreases with increasing Pr, whereas at large Ra^* this trend is reversed.

Third, the basic state log density gradient in the SOL problem is non-uniform; as a result, the equations contain coefficients with explicit x dependence. In contrast to the convection problem, which for idealized boundary conditions can be solved exactly, the presence of non-constant coefficients in the plasma problem makes it impossible to extract an analytical expression for the marginal stability threshold; in general, the problem has to be tackled numerically. To make analytical progress, the background gradient is sometimes approximated by a constant value (for example, Mendes and Bizarro (2017) represent the gradient by the inverse of the scale length for the exponential decay of density in the SOL). Similarly here, we also consider a simplified constant-coefficient ordinary differential equation, which can be solved in exactly the same way as for the convection problem. This reduced system provides useful insight into the qualitative behaviour of the full problem, accurately predicting the responses of Δn_c and k_c to variations in Ra^* and Pr. Furthermore, for each value of Pr, we have identified an approximate range of Ra^* for which there is good quantitative agreement between the full and reduced systems. Outside the regions of agreement, the full system exhibits complex behaviour that cannot be explained by the simplified system. In particular, we have demonstrated that owing to the spatial dependence of the background gradient, the radial structure of the solutions of the linear system can become highly localised, to the point of developing a boundary layer.

The work included in this thesis is been guided by the long term motivation of uncovering the mechanism for the generation of plasma filaments at the edge of magnetic confinement devices. In this chapter we have elucidated the analogy between the simple SOL plasma models and Rayleigh-Bénard convection, and have thereby gained insight into the fundamental stability problem. As such, this study constitutes a successful first step towards the long term goal and also paves the way for analytical considerations of more complicated models. Since it is believed that filaments are generated in the core region before being ejected to the scrape-off layer, the natural step for extending the current work is the consideration of a two-layer model in which the domain encompasses both of those regions — such an extension will be the subject of Chapter 5.

Chapter 4

Two-layer convection

4.1 Introduction

In light of the analogy between the single region plasma problem and that of Rayleigh-Bénard convection, we may expect a similar relation to hold between the two-region plasma problem and the two-layer convection problem. At the same time, we note that the single layer plasma problem was more considerably complicated than the classic convection problem and, by the same token, we expect the two-region plasma problem to be a more complicated version of the two-layer convection. Furthermore, as we shall establish below, the two layer convection problem is itself much richer and more complicated than the single layer problem. Therefore, before proceeding to the analysis of the two-region plasma system, in this chapter we outline the two-layer convection system and describe some of its interesting features, focusing mainly on those that will be relevant for the plasma problem. We also conduct a precursor study of a two-layer configuration with interface conditions appropriate for the core-SOL configuration.

Two-layer convection consists of two horizontal layers of fluid, one above the other, heated from below (see Figure 4.1). The two fluid layers can have different depths, and are characterised by different thermal and mechanical properties (i.e. density, viscosity, thermal diffusivity, thermal expansion coefficient etc.). Conventionally, lighter fluid is placed on top of the heavier fluid so that the static configuration is stable. The layers are separated by a thin interface, which couples the behaviour in the two layers through mechanical and thermal continuity conditions. This interface can be considered to be either flat or deformable. Furthermore, the presence of this interface allows for the Marangoni effect, whereby convection may be driven by surface tension gradients at the interface due to temperature variation (Marangoni convection in the context of superposed layers has been studied by Zeren and Reynolds (1972)). Interfacial deformation can be neglected under the assumption that the density jump between the layers is large.

Originally, most research into two-layer convection was motivated by its suggested occurrence in the Earth's mantle (Busse, 1981; Richter and Johnson, 1974). However, even without the possible application to mantle convection, the problem of convection in superposed layers has attracted considerable attention because of its interesting the-

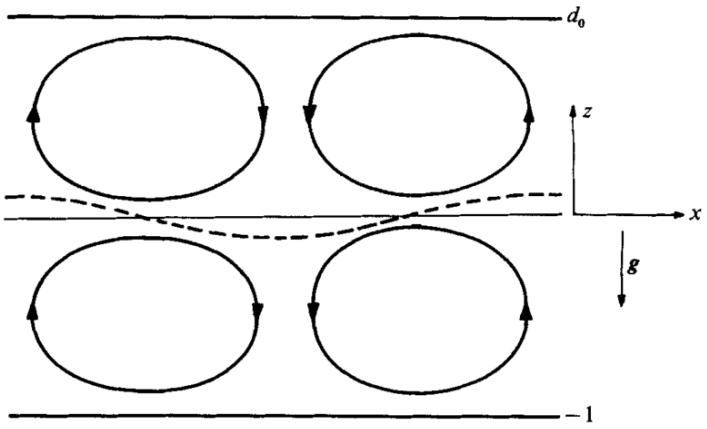

Figure 4.1: Schematic sketch of convection in a fluid composed of two immiscible layers, with either a flat horizontal interface between the layers (solid), or a distorted interface (dashed). Taken from Rasenat et al. (1989).

oretical aspects. The ostensibly simple addition of a second convecting layer engenders a rich variety of qualitatively new phenomena, such as competition between instabilities in the separate layers, oscillatory behaviour at the onset of convection, deformations of the interface, and interfacial surface tension driven modes. Owing to the large number of potentially relevant parameters, the wealth of possible behaviour is impressive. Whereas convection in a single layer of Boussinesq fluid is governed by just two dimensionless parameters, the Rayleigh and the Prandtl number, of which the latter does not enter into the stability criterion, up to ten parameters may be important for the two-layer problem. Parameters such as layer height ratios, various fluid property ratios and surface tension gradient all diversely affect the onset of convection in the layers, resulting in a variety of distinct convection modes. There have been a number of papers dedicated to exploration of some particular subspace of the parameter space, with the goal of extracting conditions for the occurrence of different convection modes (e.g. Diwakar et al., 2014; Rasenat et al., 1989).

One theoretical aspect of the two layer problem that has attracted a lot of attention is the possibility of instability occurring via a Hopf bifurcation. In the case of single layer convection, the principle of exchange of stabilities holds, whereby the solutions at the onset are steady (non-oscillatory). In the case of superposed fluids, on the other hand, overstable solutions are possible. One type of oscillatory solutions can arise on account of the presence of a deformable interface. However, another type of oscillation is possible even in the case when the interface is fixed flat (when distortions to the interface are neglected), which is due to a competition between two possible couplings between the layers. Stationary convection in layered systems can either be mechanically coupled, or thermally coupled. In the first case, one layer reaches critical conditions more rapidly (for a lower thermal constraint) than the other, which is in turn passively driven via coupling of horizontal velocities at the interface. In the second case, coupling is ensured by thermal continuity conditions, combined with buoyancy effects. Both kinds of coupling are often distinguished by the relative sense of rotation of convective cells in both layers.

The mechanically coupled mode is characterised by counter-rotating rolls, whereas the thermally coupled mode, depicted in Figure 4.1, possesses co-rotating rolls. In the case of thermal coupling, the two co-rotating rolls are separated by a buffer layer, where a small third roll may develop, which satisfies mechanical continuity at the interface. When the Rayleigh numbers in the two layers are nearly equal, competition arises between these states, and the convective pattern oscillates between mechanical and thermal coupling.

In this chapter we study a simple two-layer convection model, as an idealization of the core-SOL interaction. As described in Section 2.3.6, the differences in the magnetic field topology between the two plasma regions may have consequences on the values of perpendicular diffusion coefficients – the ion viscosity and the particle diffusivity. In particular, the diffusivities in the core and the SOL can differ by one or two orders of magnitude. Therefore, in the spirit of previous comparisons of single region plasma problems to single layer Rayleigh-Bénard convection, we may draw a similar analogy between two-region plasma models and two-layer convection — i.e. two-region plasma models can be viewed as a modified two-layer convection problem. The modifications arise in two ways: the first comes from the extra terms which account for plasma related effects (described in Chapter 3); the second is due to interface conditions. In this chapter we focus on the latter modification, and consider a simple two-layer convection model, as a precursor to the study of the more complicated core-SOL problem including all of the plasma-related effects. The superposed layers represent the core and the SOL, with the interface between the layers representing the separatrix. Conventionally, in two-layer convection, the layers are considered immiscible and an impermeability condition is enforced at the interface between the two fluids. When the interface is considered fixed flat this amounts to imposing the condition of vanishing vertical velocity. This forces convection to develop as two cells — one in each layer. A more relevant interface condition in the context of the core-SOL problem is the continuity of velocity, with plasma allowed to flow freely across the separatrix. With the immiscibility condition relaxed, two cells are no longer necessary, and convection can develop in the form of a single cell spanning the whole domain. Such a configuration is a special case of the problem studied by Le Bars and Davaille (2002). There, the two fluid layers were considered to be miscible in the sense that there was no surface tension at the interface. The only parameter that plays a role at the interface is the buoyancy number B — the ratio of chemical density anomaly to thermal density anomaly. In the limit of $B = 0$, the fluids in each layer are of equal density, and the interface conditions reduce to those in which we are interested. Whereas Le Bars and Davaille (2002) only consider the effect of variation of viscosity contrast, and focus on the occurrence of the oscillatory instability for $B \neq 0$, here, motivated by the plasma problem, we are interested in the behaviour of the system when both the viscosity and thermal diffusivity ratios between the layers vary by several orders of magnitude.

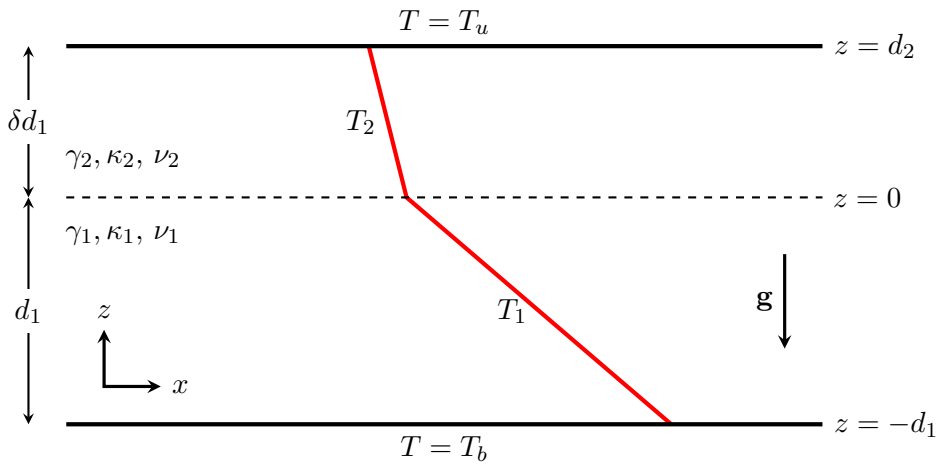

Figure 4.2: Sketch of the problem configuration.

4.2 Mathematical formulation

4.2.1 Governing equations

We consider two horizontal layers of fluid, one above the other, heated from below. Let d_1 and $d_2 = \delta d_1$ denote the depths of the lower and upper layers respectively. We assume that the fluid layers have kinematic viscosity ν_i, thermal diffusivity κ_i and coefficient of expansion γ_i, where index $i = 1$ refers to the lower layer and $i = 2$ to the upper layer. Let the lower layer occupy $-d_1 < z < 0$ and the upper $0 < z < d_2$. The planes $z = -d_1$ and $z = d_2$ are held at uniform temperatures T_b and T_u respectively, with $T_b > T_u$. A sketch of the configuration is shown in Fig. 4.2. Prior to the onset of convection the fluid is at rest and the applied temperature difference imposes a conductive temperature profile in both layers:

$$T_1 = T_b - \beta_1(z + d_1), \qquad -d_1 \le z < 0, \tag{4.1}$$

$$T_2 = T_u - \beta_2(z - d_2), \qquad 0 \le z \le d_2, \tag{4.2}$$

where β_i represent the adverse temperature gradient in each layer. Furthermore, continuity of temperature and heat flux require that

$$\beta_1 = \frac{\kappa_2(T_b - T_u)}{\kappa_2 d_1 + \kappa_1 d_2}, \qquad \beta_2 = \frac{\kappa_1(T_b - T_u)}{\kappa_2 d_1 + \kappa_1 d_2}. \tag{4.3}$$

Hence, the total temperature difference is split into a temperature drop across each layer, with the temperature drop in each layer related to the thermal diffusivities and depths of the two layers.

Under the Boussinesq approximation, the equation of motion for the velocity $\boldsymbol{u}_i$ and the heat equation for the temperature deviation θ_i from the steady state temperature

distribution, for each fluid layer, are given by

$$\boldsymbol{\nabla}\cdot\boldsymbol{u}_i = 0, \tag{4.4}$$

$$\frac{\partial \boldsymbol{u}_i}{\partial t} + \boldsymbol{u}_i\cdot\boldsymbol{\nabla}\boldsymbol{u}_i = -\frac{1}{\rho_0}\boldsymbol{\nabla}p_i + \gamma_i g\theta_i\hat{\boldsymbol{e}}_z + \nu_i\nabla^2\boldsymbol{u}_i, \tag{4.5}$$

$$\frac{\partial \theta_i}{\partial t} + \boldsymbol{u}_i\cdot\boldsymbol{\nabla}\theta_i = \beta_i w_i + \kappa_i\nabla^2\theta_i. \tag{4.6}$$

We express the governing equations in dimensionless form: scaling time with d_1^2/κ_1, length with d_1, velocities $\boldsymbol{u}_i$ with κ_1/d_1, pressures p_i with $\rho_0(\kappa_1/d_1)^2$ and temperatures θ_i with $\beta_1 d_1$ yields the following dimensionless equations for each fluid layer:

$$\frac{\partial \boldsymbol{u}_1}{\partial t} + \boldsymbol{u}_1\cdot\boldsymbol{\nabla}\boldsymbol{u}_1 = -\boldsymbol{\nabla}p_1 + Ra_1 Pr_1\theta_1\hat{\boldsymbol{e}}_z + Pr_1\nabla^2\boldsymbol{u}_1, \tag{4.7}$$

$$\frac{\partial \theta_1}{\partial t} + \boldsymbol{u}_1\cdot\boldsymbol{\nabla}\theta_1 = w_1 + \nabla^2\theta_1, \tag{4.8}$$

$$\frac{\partial \boldsymbol{u}_2}{\partial t} + \boldsymbol{u}_2\cdot\boldsymbol{\nabla}\boldsymbol{u}_2 = -\boldsymbol{\nabla}p_2 + Ra_1 Pr_1\frac{\gamma_2}{\gamma_1}\theta_2\hat{\boldsymbol{e}}_z + \frac{\nu_2}{\nu_1}Pr_1\nabla^2\boldsymbol{u}_2, \tag{4.9}$$

$$\frac{\partial \theta_2}{\partial t} + \boldsymbol{u}_2\cdot\boldsymbol{\nabla}\theta_2 = \frac{\beta_2}{\beta_1}w_2 + \frac{\kappa_2}{\kappa_1}\nabla^2\theta_2, \tag{4.10}$$

where

$$Ra_1 = \frac{g\gamma_1\beta_1 d_1^4}{\nu_1\kappa_1}, \qquad Pr_1 = \frac{\nu_1}{\kappa_1}. \tag{4.11}$$

Since we are interested in the onset of infinitesimal disturbances, we linearize the governing equations (4.7)–(4.10), thereby neglecting the nonlinear terms $\boldsymbol{u}_i\cdot\boldsymbol{\nabla}\boldsymbol{u}_i$ and $\boldsymbol{u}_i\cdot\boldsymbol{\nabla}\theta_i$. Furthermore, we assume the flow to be two-dimensional and introduce streamfunctions ψ_i such that $\boldsymbol{u}_i = \boldsymbol{\nabla}\times(\psi_i\boldsymbol{e}_y)$ and the vorticity $\omega_i = -\nabla^2\psi_i$. On taking the curl of the momentum equations (4.7) and (4.9), the linearized forms of the equations of motion become

$$\frac{1}{Pr_1}\frac{\partial \omega_1}{\partial t} = -Ra_1\frac{\partial \theta_1}{\partial x} + \nabla^2\omega_1, \tag{4.12}$$

$$\frac{\partial \theta_1}{\partial t} = \frac{\partial \psi_1}{\partial x} + \nabla^2\theta_1, \tag{4.13}$$

$$\frac{1}{Pr_1}\frac{\partial \omega_2}{\partial t} = -Ra_1\gamma_r\frac{\partial \theta_2}{\partial x} + \nu_r\nabla^2\omega_2, \tag{4.14}$$

$$\frac{\partial \theta_2}{\partial t} = \beta_r\frac{\partial \psi_2}{\partial x} + \kappa_r\nabla^2\theta_2, \tag{4.15}$$

where $\kappa_r = \kappa_2/\kappa_1$, $\nu_r = \nu_2/\nu_1$, $\beta_r = \beta_2/\beta_1$, $\gamma_r = \gamma_2/\gamma_1$.

In dimensionless units, the lower layer occupies $-1 \le z < 0$, and the upper layer occupies $0 < z \le \delta$. The outer boundaries are assumed to be stress free and isothermal, thus

$$\psi_1 = \frac{\partial^2\psi_1}{\partial z^2} = \theta_1 = 0 \quad \text{at} \quad z = -1, \tag{4.16}$$

$$\psi_2 = \frac{\partial^2\psi_2}{\partial z^2} = \theta_2 = 0 \quad \text{at} \quad z = \delta. \tag{4.17}$$

At the boundary between the two layers, i.e. at $z = 0$, we assume the following continuity conditions. Continuity of velocity gives

$$\psi_1 = \psi_2, \quad \frac{\partial \psi_1}{\partial z} = \frac{\partial \psi_2}{\partial z}. \tag{4.18}$$

Continuity of tangential and normal stress yields

$$\nu_1 \left(\frac{\partial^2 \psi_1}{\partial z^2} - \frac{\partial^2 \psi_1}{\partial x^2} \right) = \nu_2 \left(\frac{\partial^2 \psi_2}{\partial z^2} - \frac{\partial^2 \psi_2}{\partial x^2} \right), \tag{4.19}$$

$$\nu_1 \frac{\partial}{\partial z} \left(\frac{\partial^2 \psi_1}{\partial z^2} + 3\frac{\partial^2 \psi_1}{\partial x^2} \right) = \nu_2 \frac{\partial}{\partial z} \left(\frac{\partial^2 \psi_2}{\partial z^2} + 3\frac{\partial^2 \psi_2}{\partial x^2} \right). \tag{4.20}$$

It is important to note that an unavoidable consequence of the conditions of continuity of tangential and normal stress, (4.19) and (4.20), is a discontinuity in vorticity across the interface for $\nu_r \neq 1$. Finally, continuity of temperature and heat flux lead to

$$\theta_1 = \theta_2, \quad \kappa_1 \frac{\partial \theta_1}{\partial z} = \kappa_2 \frac{\partial \theta_2}{\partial z}. \tag{4.21}$$

4.2.2 Marginal stability analysis

We seek normal mode solutions of the form

$$\psi_i = \hat{\psi}_i(z) \exp(ikx + \sigma t) + c.c., \tag{4.22}$$
$$\theta_i = \hat{\theta}_i(z) \exp(ikx + \sigma t) + c.c., \tag{4.23}$$

where k is the horizontal wavenumber and σ is the growth rate. Substituting these expressions into equations (4.12)–(4.15) yields

$$\frac{\sigma}{Pr_1}(\mathcal{D}^2 - k^2)\psi_1 = ik\, Ra_1 \theta_1 + (\mathcal{D}^2 - k^2)^2 \psi_1, \tag{4.24}$$
$$\sigma \theta_1 = ik\, \psi_1 + (\mathcal{D}^2 - k^2)\theta_1, \tag{4.25}$$
$$\frac{\sigma}{Pr_1}(\mathcal{D}^2 - k^2)\psi_2 = ik\, Ra_1 \gamma_r \theta_2 + \nu_r (\mathcal{D}^2 - k^2)^2 \psi_2, \tag{4.26}$$
$$\sigma \theta_2 = ik\beta_r \psi_2 + \kappa_r (\mathcal{D}^2 - k^2)\theta_2, \tag{4.27}$$

where $\mathcal{D}$ denotes differentiation with respect to z. The boundary and interface conditions (4.16)–(4.21) may be written as

$$\psi_1 = \mathcal{D}^2 \psi_1 = \theta_1 = 0 \quad \text{at} \quad z = -1, \tag{4.28}$$
$$\psi_2 = \mathcal{D}^2 \psi_2 = \theta_2 = 0 \quad \text{at} \quad z = \delta, \tag{4.29}$$
$$\psi_1 = \psi_2, \quad \mathcal{D}\psi_1 = \mathcal{D}\psi_2,$$
$$\left(\mathcal{D}^2 \psi_1 + k^2 \psi_1\right) = \nu_r \left(\mathcal{D}^2 \psi_2 + k^2 \psi_2\right),$$
$$\left(\mathcal{D}^3 \psi_1 - 3k^2 \mathcal{D}\psi_1\right) = \nu_r \left(\mathcal{D}^3 \psi_2 - 3k^2 \mathcal{D}\psi_2\right),$$
$$\theta_1 = \theta_2, \quad \mathcal{D}\theta_1 = \kappa_r \mathcal{D}\theta_2 \quad \text{at} \quad z = 0. \tag{4.30}$$

As described in the Introduction (Section 4.1), the problem formulated here is a special case of that studied by Le Bars and Davaille (2002). There, the fluid layers were considered to have different densities, thus introducing the additional parameter B, a ratio of two density differences, one of chemical and one of thermal origin. The two problems are equivalent when $B = 0$. In general, depending on the value of B, the solutions at the onset of instability are either steady or oscillatory. In particular, oscillatory instability sets in for $0 < B < B_c$, where B_c is some critical value; for $B > B_c$ the most unstable mode has purely real growth rate. Similarly, in the absence of density stratification, i.e. in the limit $B = 0$, the frequency at the onset of instability vanishes and the oscillatory mode transforms itself into a steady mode. Therefore, we restrict attention to the onset of stationary convection, in which case $\sigma = 0$. Consequently, the Prandtl number Pr_1 does not enter the analysis. It follows from (4.3) that $\beta_r = \kappa_r^{-1}$; furthermore, we fix $\gamma_r = 1$. Our task has thus been reduced to the problem of determining the critical conditions as a function of the parameters δ, ν_r and κ_r.

It is useful to introduce a separate Rayleigh number for the upper layer, defined by

$$Ra_2 = \frac{g\gamma_2\beta_2(\delta d_1)^4}{\nu_2\kappa_2} = \frac{Ra_1\delta^4}{\nu_r\kappa_r^2}. \tag{4.31}$$

The ratio Ra_2/Ra_1 provides a measure for the ratio of the contributions from the two layers to the buoyancy-driven instability. When this ratio is significantly different from unity the onset of instability occurs primarily in one layer while the other plays a passive role (Rasenat et al., 1989). Clearly, this will be the case when either ν_r or κ_r (or both) are either very small or very large. Note, however that it is not instructive to consider either of the Rayleigh numbers individually. For example, consider the case of layers of equal depth and viscosity ($\delta = \nu_r = 1$), and large thermal diffusivity contrast. Recall from (4.3) that the basic state temperature gradients in each layer are

$$\beta_1 = \frac{\Delta T}{d_1\left(1 + \kappa_r^{-1}\delta\right)}, \qquad \beta_2 = \frac{\Delta T}{\delta d_1\left(1 + \kappa_r\delta^{-1}\right)}, \tag{4.32}$$

where $\Delta T = (T_b - T_u)$. It follows that as $\kappa_r \to 0$, $\beta_1 \to 0$ and $\beta_2 \to \Delta T/\delta d_1$. Thus the entire temperature drop occurs over the upper layer, while in the bottom layer there is no buoyancy and consequently $Ra_1 \to 0$. This should not be taken to mean that layer 1 becomes unstable even in the absence of an adverse thermal gradient, but rather that layer 1 does not contribute towards the onset of instability. Conversely, when $\kappa_r \to \infty$, $\beta_1 \to \Delta T/d_1$ and $\beta_2 \to 0$; thus layer 1 is entirely responsible for the onset of instability, while layer 2 plays a passive role.

Finally, we observe the symmetry of the configuration. If we instead choose to scale the equations using the properties of the upper layer, i.e. scale time with $(\delta d_1)^2/\kappa_2$, length with δd_1, velocity with $\kappa_2/(\delta d_1)$, pressure with $\rho_0(\kappa_2/(\delta d_1))^2$ and temperature with $\beta_2\delta d_1$,

the governing equations become

$$\frac{1}{Pr_2}\partial_t\omega_1 = -Ra_2\gamma_r^{-1}\partial_x\theta_1 + \nu_r^{-1}\nabla^2\omega_1, \tag{4.33}$$

$$\partial_t\theta_1 = \beta_r^{-1}\partial_x\psi_1 + \kappa_r^{-1}\nabla^2\theta_1, \tag{4.34}$$

$$\frac{1}{Pr_2}\partial_t\omega_2 = -Ra_2\partial_x\theta_2 + \nabla^2\omega_2, \tag{4.35}$$

$$\partial_t\theta_2 = \partial_x\psi_2 + \nabla^2\theta_2, \tag{4.36}$$

where $Pr_2 = \nu_2/\kappa_2$. In this case layer 1 occupies $-\delta^{-1} < z < 0$, and layer 2 occupies $0 < z < 1$. Comparing these with (4.12)–(4.15), we observe that the equations are identical on interchanging (Ra_1, Pr_1, k, δ, ν_r, κ_r, β_r, γ_r) and (Ra_2, Pr_2, k/δ, δ^{-1}, ν_r^{-1}, κ_r^{-1}, β_r^{-1}, γ_r^{-1}). Therefore, we need only consider the case with $\delta \leq 1$; the case with $\delta > 1$ can be reconstructed from symmetry considerations.

4.2.3 Limiting cases

We note that when the fluid properties of each layer are equal (i.e. $\nu_r = \kappa_r = 1$) then the problem reduces to that of classical (single layer) Rayleigh-Bénard convection, with the onset of instability occurring at

$$Ra_1^c = \frac{27}{4}\left(\frac{\pi}{1+\delta}\right)^4, \qquad k^c = \frac{1}{\sqrt{2}}\left(\frac{\pi}{1+\delta}\right). \tag{4.37}$$

On the other side of the spectrum, the problem we wish to study has four interesting limits:

1. when one of the layers is infinitely more viscous than the other, i.e. $\nu_r \to \infty$ (or $\nu_r \to 0$);

2. when one of the layers is infinitely more thermally diffusive than the other, i.e. $\kappa_r \to \infty$ (or $\kappa_r \to 0$);

3. when one of the layers is both infinitely more viscous and thermally diffusive than the other, i.e. $\kappa_r \to \infty$, $\nu_r \to \infty$ (or $\kappa_r \to 0$, $\nu_r \to 0$);

4. when one of the layers is infinitely more viscous and the other is infinitely more thermally diffusive, i.e. $\kappa_r \to 0$, $\nu_r \to \infty$ (or $\kappa_r \to \infty$, $\nu_r \to 0$).

Three of these cases (1, 3 and 4) can be understood by considering the limits in the problem of Nield (1968), who studied the onset of stationary convection in a layer of fluid, of depth d and thermal conductivity K, bounded from below by a rigid plate of infinite thermal conductivity and from above by a solid layer of finite conductivity K' and finite thickness d' (see Figure 4.3). The fluid layer is governed by the steady version of equations (4.12) and (4.13), while the solid layer obeys $\nabla^2\theta = 0$. The no-slip condition is applied on the boundaries of the fluid layer: i.e. at the bottom plate and at the fluid-solid boundary. The thermal boundary conditions consist of fixed temperature at the bottom of the fluid

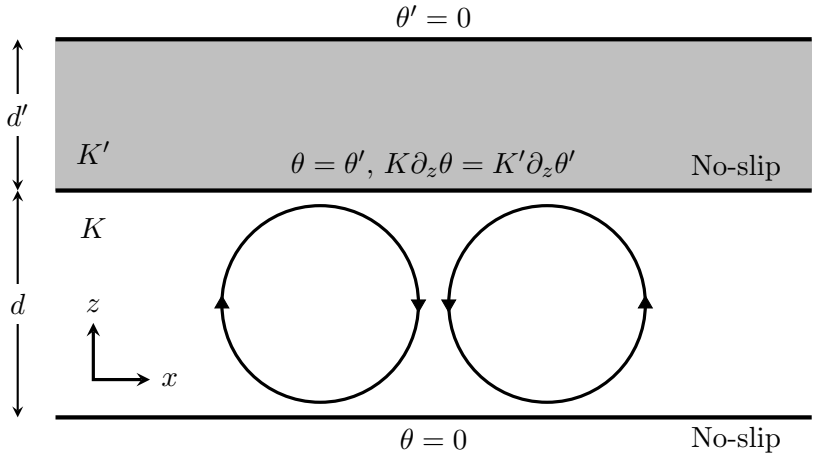

Figure 4.3: Schematic of the configuration studied by Nield (1968).

and at the top of the solid, and continuity of temperature and heat flux at the fluid-solid interface.

Nield (1968) calculated the critical Rayleigh number as a function of the depth ratio d'/d and thermal conductivity ratio K'/K (these are analogous to parameters δ and κ_r in our problem). The two limiting cases of interest are: $K'/K \to 0$, and $K'/K \to \infty$. When $K'/K \to \infty$, the critical Rayleigh number and the critical wavenumber tend to

$$Ra = 1707.8, \qquad k = 3.117. \tag{4.38}$$

These correspond to the onset of convection in a layer bounded by rigid isothermal plates. This makes sense: when K' is infinite, the boundary condition at the top of the solid is instantaneously transmitted throughout the solid, to the top of the fluid.

The second limit is slightly more subtle. When $K'/K \to 0$, the critical Rayleigh number and the critical wavenumber tend to

$$Ra = 1295.8, \qquad k = 2.553. \tag{4.39}$$

These values correspond to those of the onset of convection in a layer where one boundary is rigid and isothermal and the other is rigid with constant heat flux. As $K'/K \to 0$, the condition of contuinuty of heat flux at the fluid-solid boundary becomes the condition of no heat flux and the solid layer becomes a perfect insulator.

4.3 Onset of convection

4.3.1 The case of equal layer depths ($\delta = 1$)

We now return to the problem governed by equations (4.24)–(4.30). We begin with the case of two layers of equal depth, i.e. $\delta = 1$, and equal thermal diffusivity, $\kappa_r = 1$, and consider the effect of varying the viscosity ratio ν_r. Figure 4.4 shows the variation of the critical Rayleigh numbers, Ra_1^c and Ra_2^c, and the critical wavenumber k^c with respect

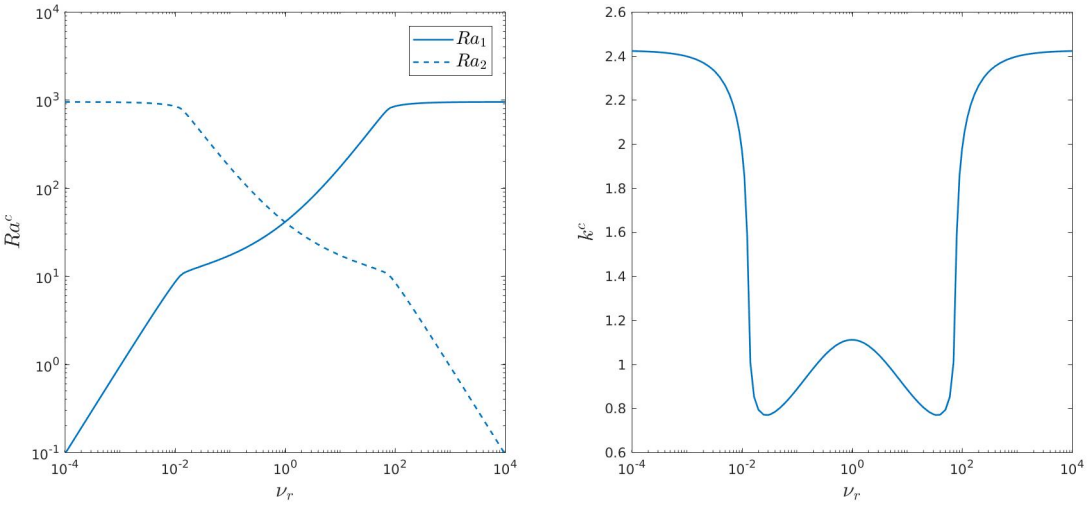

(a) (b)

Figure 4.4: Variation of the critical Rayleigh number and the accompanying critical wavenumber as a function of ν_r, for the case of layers of equal depth and equal thermal diffusivity ($\delta = \kappa_r = 1$).

to ν_r. As discussed in Section 4.2.2, the symmetry of the system with $\delta = 1$ results in a reflectional symmetry (when ν_r is plotted logarithmically) between the Ra_1^c and Ra_2^c curves about the line $\nu_r = 1$. Similarly, k^c is symmetric about $\nu_r = 1$.

Perhaps the most striking feature of Figure 4.4(b) is the non-monotonic behaviour of the critical wavenumber k. When $\nu_r = 1$ (i.e. single layer convection), the convection cells fill the entire depth of the domain, with horizontal length scale given by (4.37). On first introducing a viscosity contrast between the two layers — and here we consider $\nu_r > 1$, without loss of generality — there is an initial decrease in the critical wavenumber, indicating a shift in the preferred horizontal length scale toward larger cells. This is accompanied by a decrease in Ra_2 and an increase in Ra_1, thereby indicating the growing importance of the lower layer in terms of contributing to the instability. On increasing the viscosity ratio further, there is a marked transition, with a sharp increase in the critical wavenumber. At this point the convective cells are expelled from the viscous layer, and the motion is localised in the layer with lower viscosity, as seen in Figure 4.5. It is interesting to note that similar localised solutions have been observed in the problem of single layer convection in which the viscosity is a strongly but smoothly varying function of temperature; there the convection becomes confined to a sublayer as the ratio of maximum to minimum viscosity increases (see for example Booker (1976); Richter et al. (1983)).

As the viscosity contrast becomes infinite, the interface behaves like a rigid boundary, and the viscous layer like a solid slab. The critical Rayleigh number of the less viscous layer and the critical wavenumber tend towards asymptotic values, which correspond to those of convection in a layer of fluid in which one boundary is a solid layer of finite thermal conductivity and thickness; on this boundary the velocity obeys the no-slip condition. Hence, in this limit, the problem is reduced to that studied in Ref. Nield (1968), although

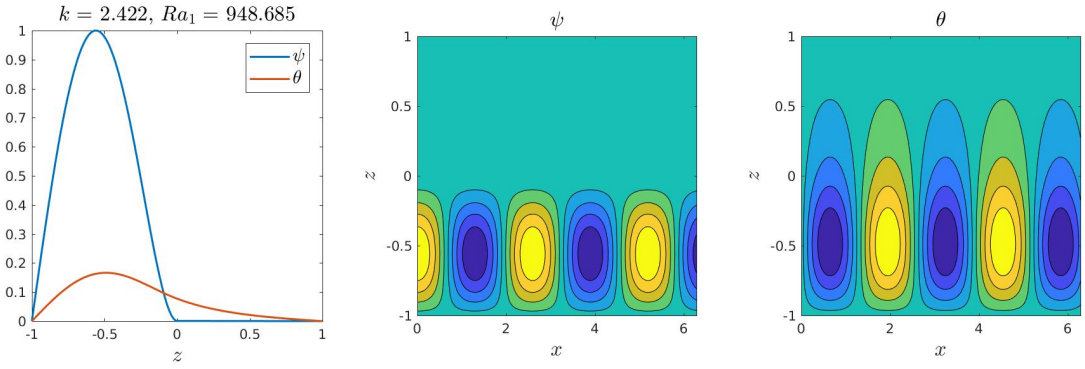

(a) (b) (c)

Figure 4.5: Critical mode for $\nu_r = 10^4$, $\kappa_r = 1$, $\delta = 1$. (a) Eigenfunction profiles; (b) contour plot of the streamfunction; (c) contour plot of the temperature perturbation.

there the other boundary was assumed to be rigid (no-slip), whereas here it is stress free. Naturally, the Rayleigh number of the more viscous layer decreases indefinitely according to relation (4.31). As noted earlier, this does not mean that the viscous layer becomes increasingly more unstable, but rather that the motion in this layer ceases, with the dynamics governed solely by the diffusion of the temperature perturbation.

The variation of Ra^c and k^c with respect to κ_r for the case of layers of equal viscosity, i.e. $\nu_r = 1$, is shown in Fig. 4.6. Similarly to the limit of infinite viscosity contrast described above, as the ratio of thermal diffusivities becomes infinite, the critical Rayleigh number and the critical wavenumber of the less thermally diffusive layer tend towards asymptotic values. Similarly, the Rayleigh number of the layer with higher thermal diffusivity decreases indefinitely according to expression (4.31). In this case, as the ratio of thermal diffusivities becomes infinite, the adverse temperature gradient in the thermally diffusive layer vanishes (cf. (4.32)), which necessitates vanishing Rayleigh number. The isothermal boundary condition is transmitted instantaneously throughout the thermally diffusive layer, and consequently the temperature perturbation is localised in the layer with lower thermal diffusivity, as can be seen in Fig. 4.7. Note, however, that the fluid motion persists in the thermally diffusive layer. Furthermore, the horizontal wavelength given by the asymptotic value of k^c as κ_r approaches either zero or infinity is representative of the vertical extent of the fluid motion. The motion in the thermally diffusive layer is of Stokes flow type (governed by $\nabla^2\nabla^2\psi = 0$) and is driven entirely by the mechanical forcing at the interface.

Figure 4.8 shows the variation of Ra^c and k^c with respect to ν_r at different values of κ_r. Clearly, the non-monotonic behaviour of the wavenumber as a function of ν_r persists for values of κ_r other than unity. In fact it becomes more intricate, being dependent on whether the more (less) viscous layer is also more (less) thermally diffusive — i.e. if ν_r and κ_r are both less than 1, or both greater than 1.

If $\kappa_r > 1$, then initially as ν_r is increased from 1, k^c is reduced until it reaches a minimum, after which a further increase leads to a sharp increase in k^c towards an asymptotic limit. The position of the minimum of k^c, and the subsequent sharp transition, occurs at

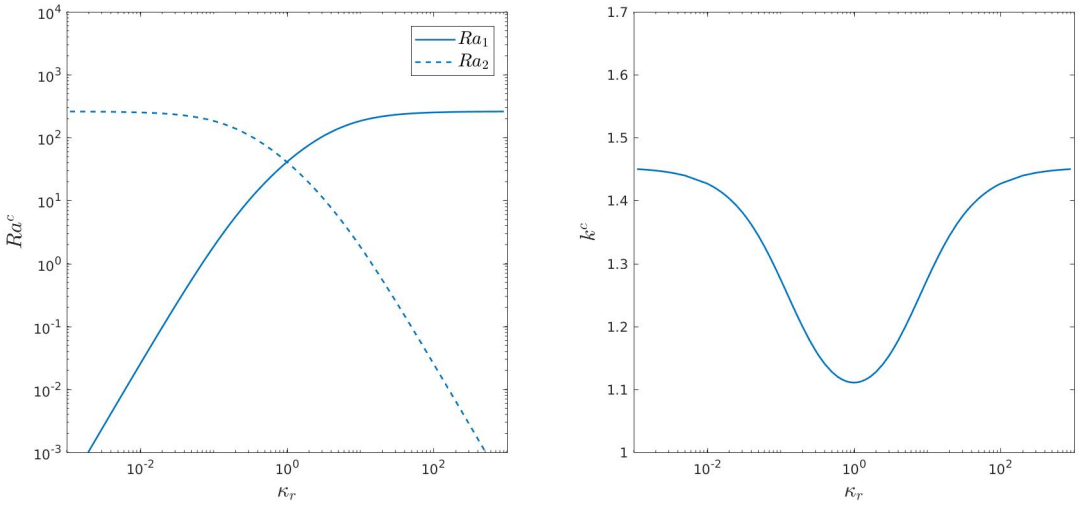

(a) (b)

Figure 4.6: Variation of the critical Rayleigh number (solid lines denote Ra_1^c, dash-dot lines denote Ra_2^c) and critical wavenumber as a function of κ_r, for the case of layers of equal depths and equal viscosity ($\delta = \nu_r = 1$).

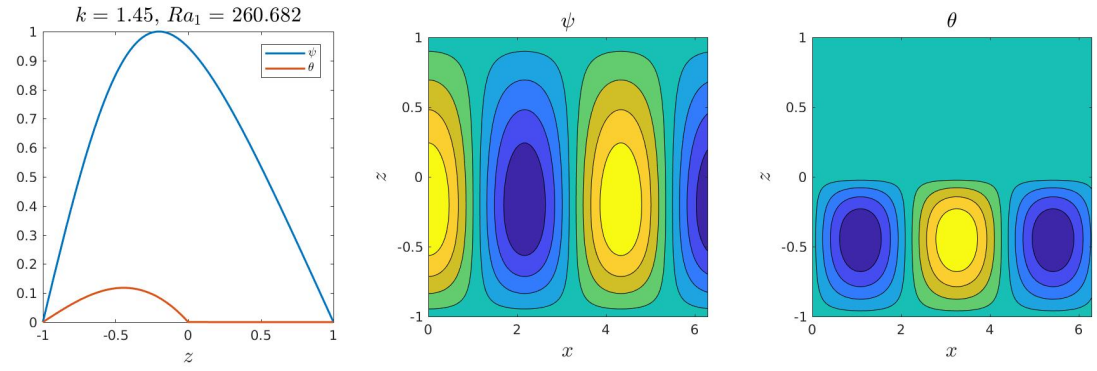

(a) (b) (c)

Figure 4.7: Critical mode for $\kappa_r = 1000$, $\nu_r = 1$, $\delta = 1$. (a) Eigenfunction profiles; (b) contour plot of the streamfunction; (c) contour plot of the temperature perturbation.

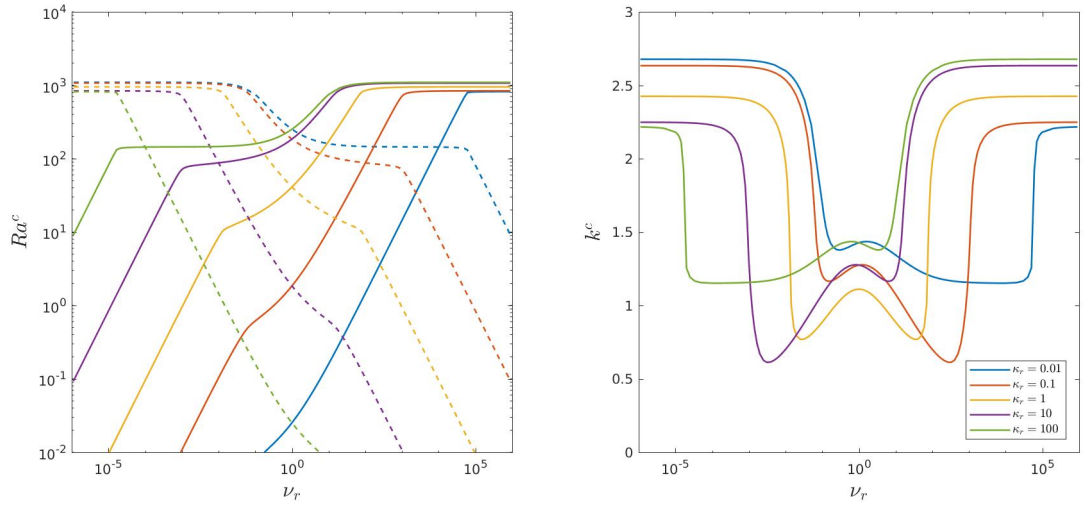

(a) (b)

Figure 4.8: Variation of the critical Rayleigh number (solid lines denote Ra_1^c, dash-dot lines denote Ra_2^c) and critical wavenumber as a function of ν_r for different values of κ_r, and $\delta = 1$.

lower values of ν_r for higher values of κ_r. Furthermore, the initial dip in k^c is smaller for higher values of κ_r. As $\nu_r \to \infty$, the limiting values of the critical Rayleigh number of the less viscous layer (in this case the bottom layer) and the critical wavenumber increase with κ_r. The behaviour of the limits of k^c and Ra^c as $\nu_r \to \infty$ is consistent with the results of Nield (1968), where it was also observed that both k^c and Ra^c increase as the ratio of solid to fluid conductivity is increased.

By analogy with the limits of Nield (1968), keeping ν_r infinite and allowing $\kappa_r \to \infty$, the viscous slab becomes infinitely conducting and so, in addition to acting like a no-slip boundary, the interface now also becomes isothermal. The asymptotic values of the critical Rayleigh number and the critical wavenumber correspond to those of single layer convection with fixed temperature boundaries of which one is rigid and the other is stress free (Pellew and Southwell, 1940):

$$R_*^c = 1101, \qquad k_*^c = 2.67. \tag{4.40}$$

In this limit, both the convection cell and the temperature perturbation occupy the layer with lower viscosity and lower thermal diffusivity, as seen in Fig. 4.9. This picture changes slightly when the more viscous layer is less thermally diffusive. For $\kappa_r < 1$, as ν_r is increased from 1, there is an initial small increase in k^c, followed by a decrease in k^c to a minimum, and a subsequent sharp increase towards the asymptotic limit of $\nu_r \to \infty$. Additionally, the minimum of k^c moves to higher values of ν_r for smaller κ_r.

We have seen above (Fig. 4.5) that when the viscosity contrast is sufficiently large then the convective cells become localised in the layer with lower viscosity, while the other layer behaves like a solid slab. Similarly, for large enough thermal diffusivity contrast

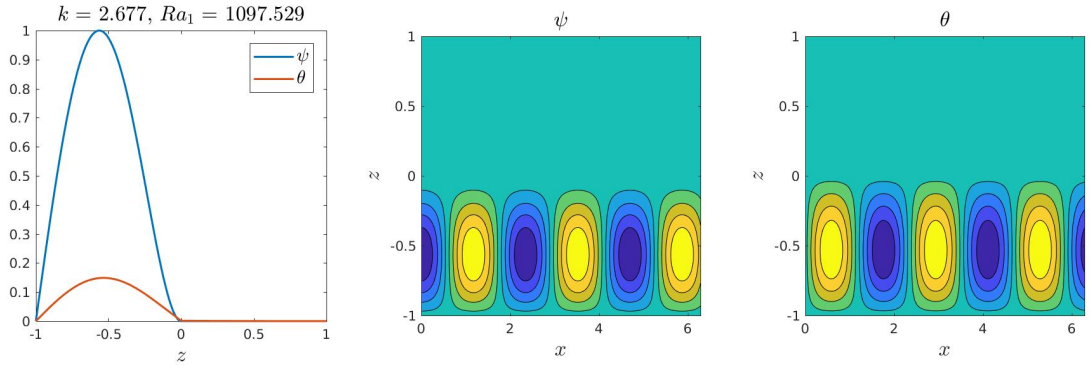

(a) (b) (c)

Figure 4.9: Critical mode for $\kappa_r = 100$, $\nu_r = 9 \times 10^5$, $\delta = 1$. (a) Eigenfunction profiles; (b) contour plot of the streamfunction; (c) contour plot of the temperature perturbation.

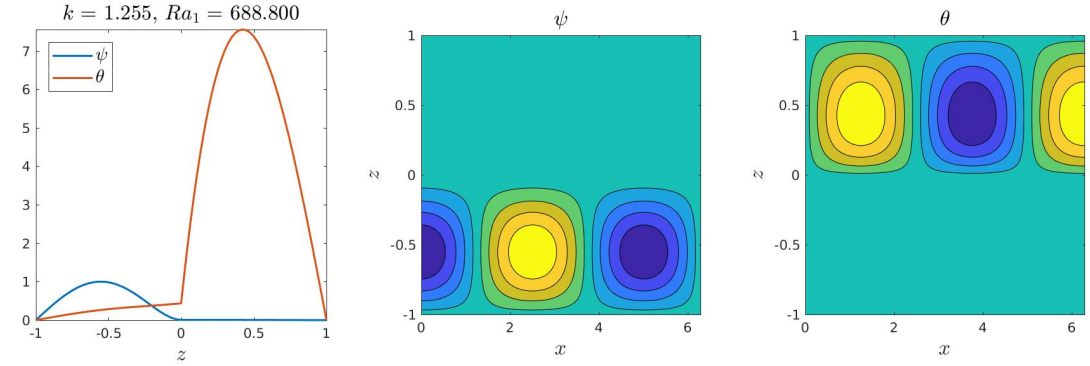

(a) (b) (c)

Figure 4.10: Critical mode for $\kappa_r = 0.01$, $\nu_r = 5 \times 10^4$, $\delta = 1$. (a) Eigenfunction profiles; (b) contour plot of the streamfunction; (c) contour plot of the temperature perturbation.

(Fig. 4.7), the temperature perturbation becomes confined to the less thermally diffusive layer. Interestingly, there is a regime in parameter space, with ν_r large and κ_r small, in which these pictures can be combined such that the critical mode is one in which fluid motion and temperature perturbation are segregated — i.e. confined to different layers. An example of such a mode is plotted in Figure 4.10, where $\nu_r = 5 \times 10^4$ and $\kappa_r = 0.01$. However, this mode does not persist in the limit $\nu_r \to \infty$ and $\kappa_r \to 0$. On increasing ν_r, eventually there is a sharp increase in k^c (cf. Fig. 4.8) and the critical mode transitions towards the $\nu \to \infty$ limit: i.e. that corresponding to the critical mode of convection in a layer of fluid in which one boundary is a solid slab of finite thermal conductivity and thickness, as seen in Figure 4.11.

In the limit $\nu_r \to \infty$ and $\kappa_r \to 0$, the viscous slab behaves like a perfect insulator and the thermal condition on the interface is that of no heat flux. The limiting values of the critical Rayleigh number and the critical wavenumber correspond to those of single layer convection in which one of the boundaries is rigid and insulating, and the other is stress free and isothermal:

$$R_*^c = 816.75, \qquad k_*^c = 2.215. \tag{4.41}$$

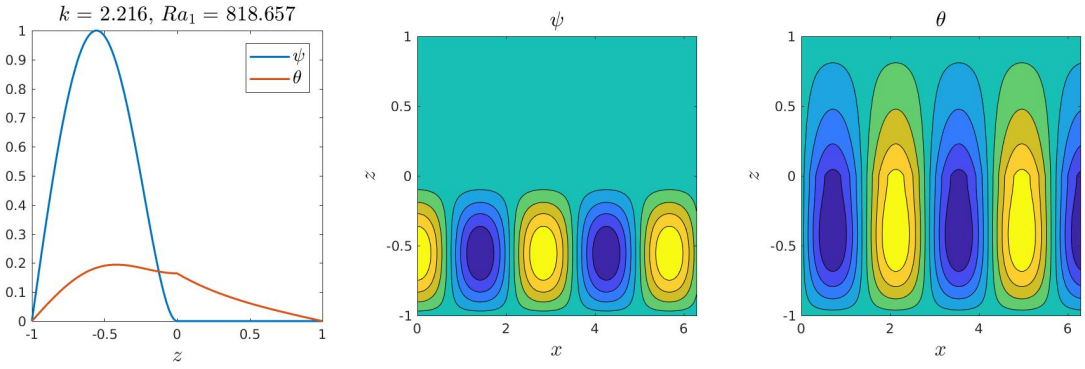

(a) (b) (c)

Figure 4.11: Critical mode for $\kappa_r = 0.01$, $\nu_r = 9 \times 10^5$, $\delta = 1$. (a) Eigenfunction profiles; (b) contour plot of the streamfunction; (c) contour plot of the temperature perturbation.

4.3.2 The case of different layer depths ($\delta \neq 1$)

We now consider the case where the two layers are of different depth. As noted in Section 4.2.2, the symmetry of the problem allows us to restrict attention to the case with $\delta < 1$, which means that the top layer will always be thinner than the bottom layer. We note that the interpretation of the limiting behaviour of the critical Rayleigh number and the critical wavenumber with respect to ν_r and κ_r described above also holds in the case of layers of unequal depth. Additionally, in the limit $\delta \to 0$, Ra^c and k^c tend to the asymptotic values given by (4.40).

Figure 4.12 shows the variation of the critical Rayleigh numbers, Ra_1^c and Ra_2^c, with respect to the viscosity contrast ν_r for different values of layer depth ratio δ, with $\kappa_r = 1$. First, we consider the case with $\nu_r > 1$, i.e. the thin upper layer is more viscous. The behaviour of the critical Rayleigh number and the critical wavenumber in the cases of unequal layer depths ($\delta = 0.25$ and $\delta = 0.5$) is qualitatively similar to that in the case of equal layer depths ($\delta = 1$). When $\nu_r = 1$, the convective cell fills the entire domain, and its horizontal scale, with critical wavenumber k^c given by expression (4.37), is comparable with the depth of the box. Initially, as ν_r is increased, k^c is reduced until it reaches a minimum. A further increase in ν_r leads to an increase in k^c towards an asymptotic limit, where the top layer behaves like a solid slab. This increase in k^c becomes less sharp, and occurs at lower values of ν_r, for smaller δ. The asymptotic values of Ra_1^c and k^c in the limit $\nu_r \to \infty$ increase as δ is decreased. This is consistent with the results of Ref. Nield (1968), in which it was also observed that both Ra^c and k^c increase with a decrease in the ratio of the depth of the solid layer to that of the fluid layer.

When $\nu_r < 1$, the thick bottom layer is more viscous, behaving like a solid slab when the viscosity contrast is sufficiently large. The value of ν_r at which the transition to this limiting behaviour takes place decreases with decreasing δ. Furthermore, in the case of layers of unequal depth (i.e. $\delta \neq 1$) the transition becomes a discontinuous jump. At the point of discontinuity the marginal stability curve has two distinct minima, as seen in Fig. 4.13. Therefore, at the transition point, there are two distinct unstable modes. At the minimum corresponding to the lower wavenumber, the convective cell fills the entire

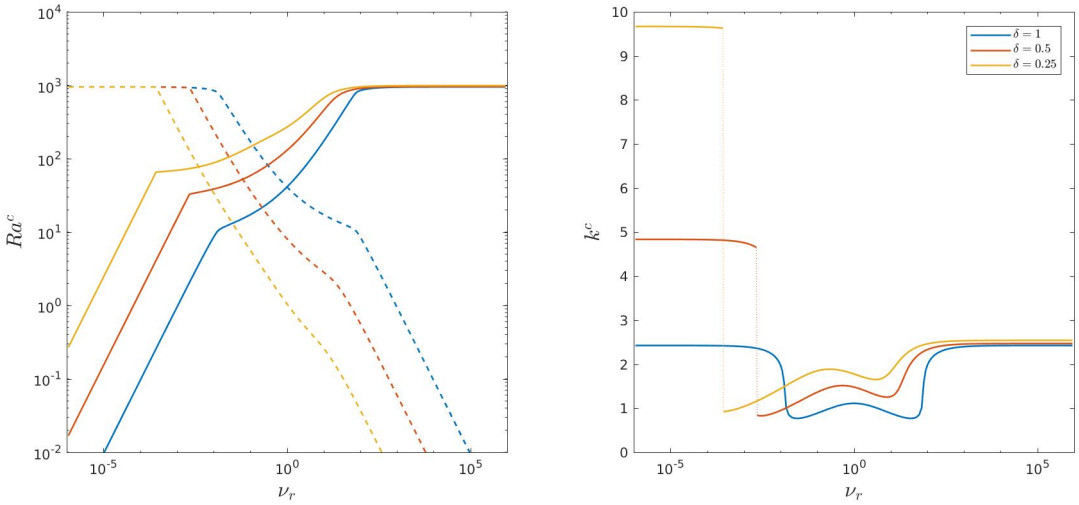

(a) (b)

Figure 4.12: Variation of the critical Rayleigh number (solid lines denote Ra_1^c, dash-dot lines denote Ra_2^c) and critical wavenumber as a function of ν_r for different values of δ and $\kappa_r = 1$.

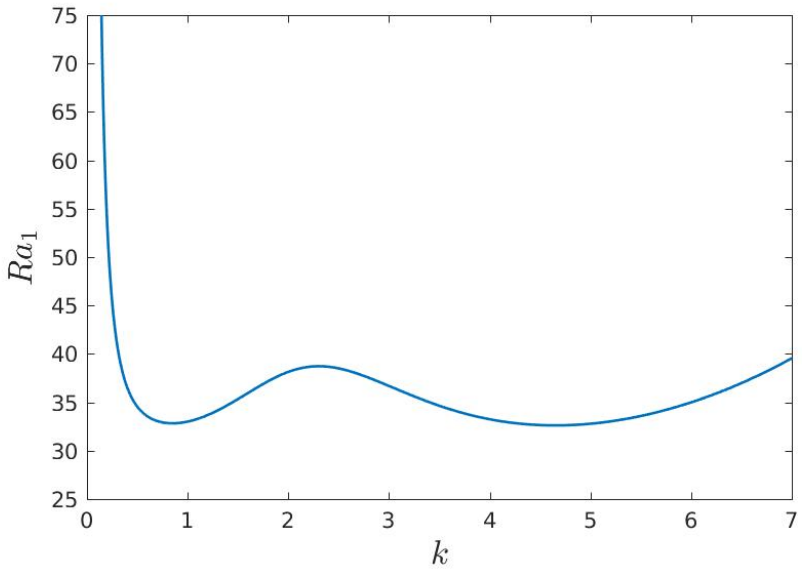

Figure 4.13: Marginal stability curve for the case $\delta = 0.5$, $\nu_r = 2.2 \times 10^{-3}$, $\kappa_r = 1$.

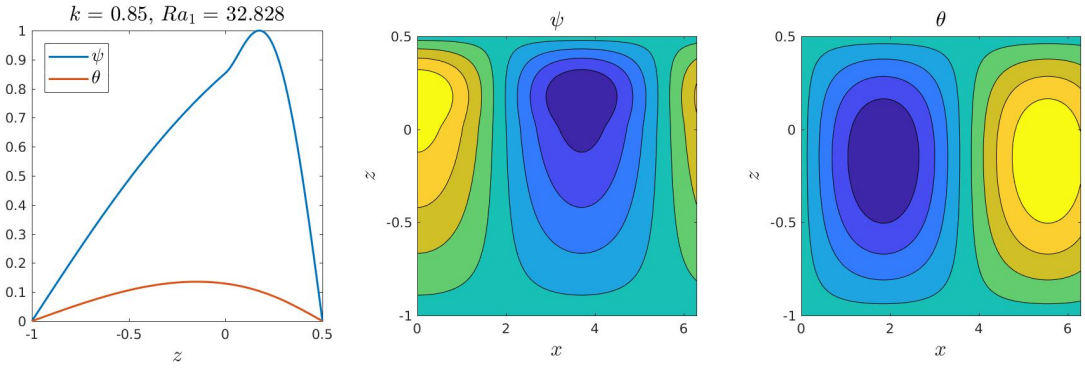

(a) (b) (c)

Figure 4.14: Solution associated with the minimum at $k = 0.85$ of the marginal stability curve in Figure 4.13. (a) Eigenfunction profiles, (b) contour plot of the streamfunction, (c) contour plot of the temperature perturbation.

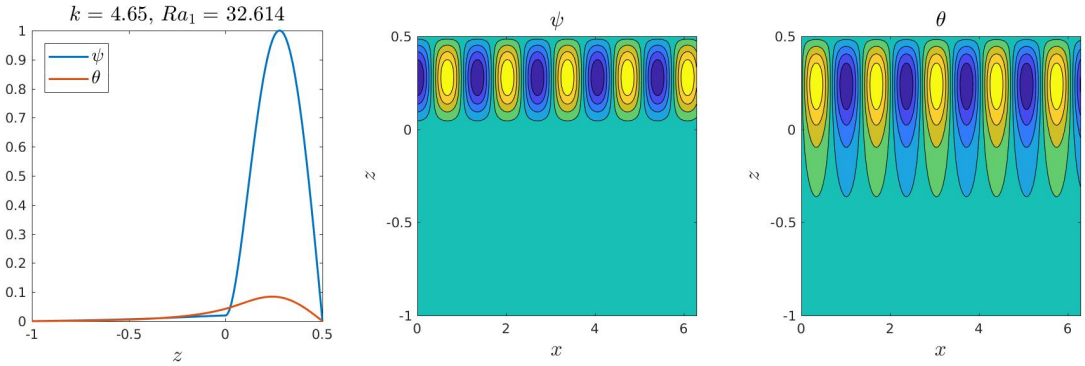

(a) (b) (c)

Figure 4.15: Solution associated with the minimum at $k = 4.65$ of the marginal stability curve in Figure 4.13. (a) Eigenfunction profiles, (b) contour plot of the streamfunction, (c) contour plot of the temperature perturbation.

domain, as can be seen in Fig. 4.14, with a horizontal scale comparable with that of the depth of the box. By contrast, at the minimum corresponding to the larger wavenumber, the motion is localised in the layer with lower viscosity, as seen in Fig. 4.15. The horizontal scale of convection cells in this case is comparable with the depth of the thin upper layer.

Figures 4.16, 4.17 show the variation of the critical Rayleigh numbers and the critical wavenumber with respect to ν_r, with $\kappa_r = 0.1$ and $\kappa_r = 10$ respectively. As in the case of equal layer depths ($\delta = 1$), the position of the minimum of the sharp transition in k^c shifts to lower values of ν_r as κ_r is increased.

4.4 Discussion

In this paper we have studied the linear stability of a two-layer Boussinesq convection problem in order to gain insight into the onset of interchange instability in two-region models of the plasma edge in fusion confinement devices. A key difference between the

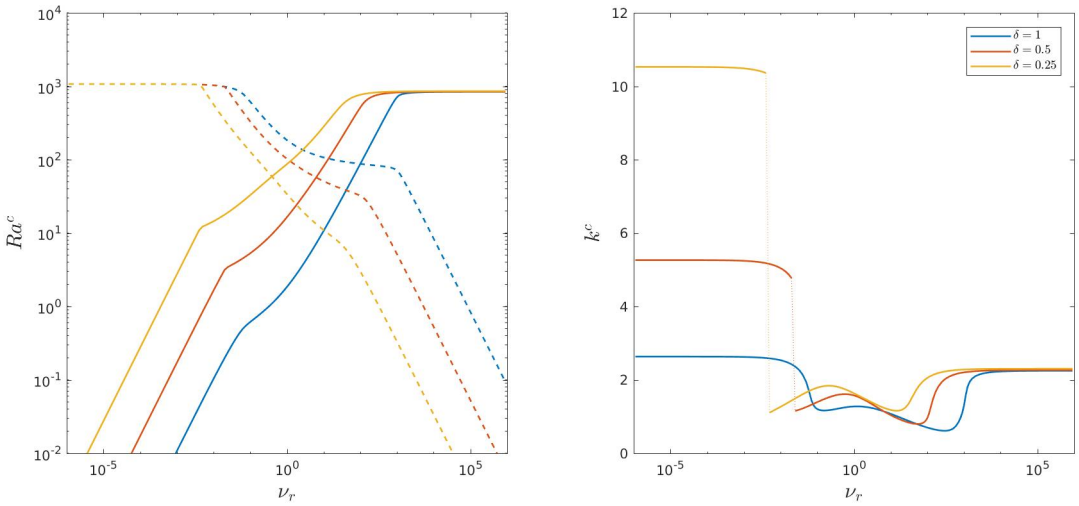

(a) (b)

Figure 4.16: Variation of the critical Rayleigh number (solid lines denote Ra_1^c, dash-dot lines denote Ra_2^c) and critical wavenumber as a function of ν_r for different values of δ, and $\kappa_r = 0.1$.

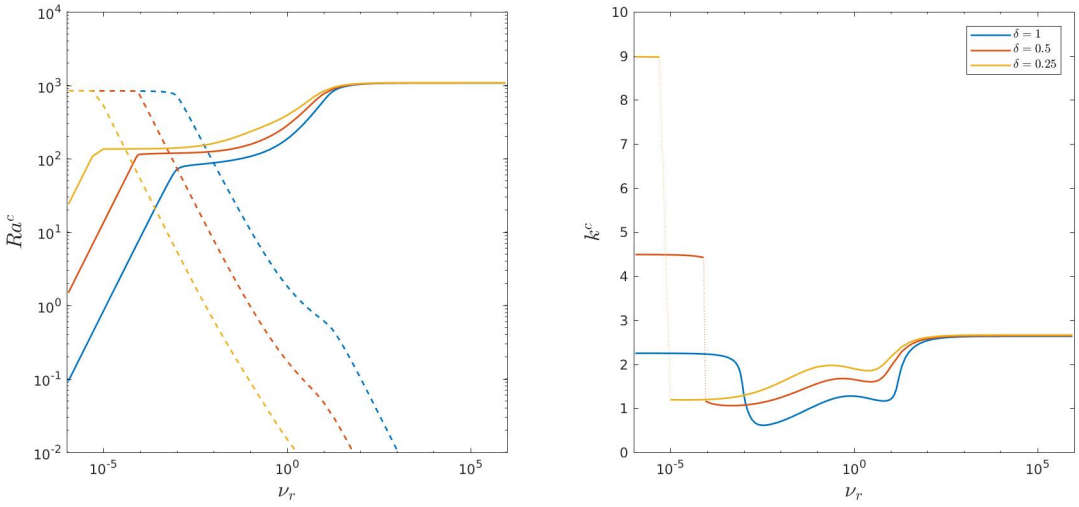

(a) (b)

Figure 4.17: Variation of the critical Rayleigh number (solid lines denote Ra_1^c, dash-dot lines denote Ra_2^c) and critical wavenumber as a function of ν_r for different values of δ, and $\kappa_r = 10$.

model that we have studied here and two-layer problems that have been considered previously is in the choice of interface conditions. Whereas conventionally the two layers are considered immiscible, separated by an impermeable interface, in the context of the core-SOL problem the relevant condition at the boundary between the two layers is the continuity of velocity, with plasma allowed to flow freely across the separatrix. The edge plasma problem can therefore be thought of as convection with a jump in viscosity and thermal diffusivity.

We have investigated the onset of convection as a function of viscosity contrast, thermal diffusivity contrast and layer depth ratio. Even in the fairly simple system considered here, depending on the values of these parameters, we have found a variety of distinct unstable modes. These can be broadly categorized according to three regimes: whole layer, localised, and segregated. The approximate boundaries between these regimes in (ν_r, κ_r) parameter space for the two cases of $\delta = 1$ and $\delta = 0.5$ are shown in Figure 4.18; it can be seen that the regime diagrams for equal and unequal layer depths are qualitatively similar.

The whole layer regime occurs when neither the viscosity contrast, nor the thermal diffusivity contrast, are too large (region I in Fig. 4.18). In this regime, both the convection cells and the temperature perturbation extend over the two layers.

The localised modes are characterized by either the velocity cells, or the temperature perturbations, or both, being confined to one of the layers. In this regime, one of the layers is entirely responsible for the onset of instability, while the other plays a passive role. The localised solutions are associated with limits of infinite viscosity contrast and infinite thermal diffusivity contrast, and can be further sub-categorized accordingly. In the regime associated with the limit of infinite viscosity contrast (region IIb), the viscous layer behaves like a solid slab; the convection cells become localised to the layer with lower viscosity, and the temperature perturbation penetrates the viscous layer only through diffusion. In the regime associated with the limit of infinite thermal diffusivity contrast (region IIa), the temperature perturbation is confined to the layer with lower thermal diffusivity. In the layer with higher thermal diffusivity, there is no buoyancy, owing to the absence of thermal gradient, and the fluid motion is forced entirely through the mechanical coupling at the interface. Naturally, on intersection of the regimes associated with $\kappa_r \to \infty$ and $\nu_r \to \infty$ (or $\kappa_r \to 0$ and $\nu_r \to 0$) — i.e. when one of the layers is both significantly more viscous and thermally diffusive — both the velocity and the temperature perturbation of the most unstable mode are localised to the less diffusive layer (region IIab). The transition between the whole-layer and the localised regimes is governed by the ratio of the Rayleigh numbers. Although the precise critical value of that ratio depends nonlinearly on ν_r, κ_r and δ, and is impossible to extract analytically, in general it seems that one of the Rayleigh numbers must be sufficiently greater than the other.

The segregated regime occurs when one of the layers is significantly more viscous, while the other is significantly more thermally diffusive (region III). The critical mode is one where the fluid motion and the temperature perturbation are segregated, being confined, respectively, to layers with lower viscosity and lower thermal diffusivity.

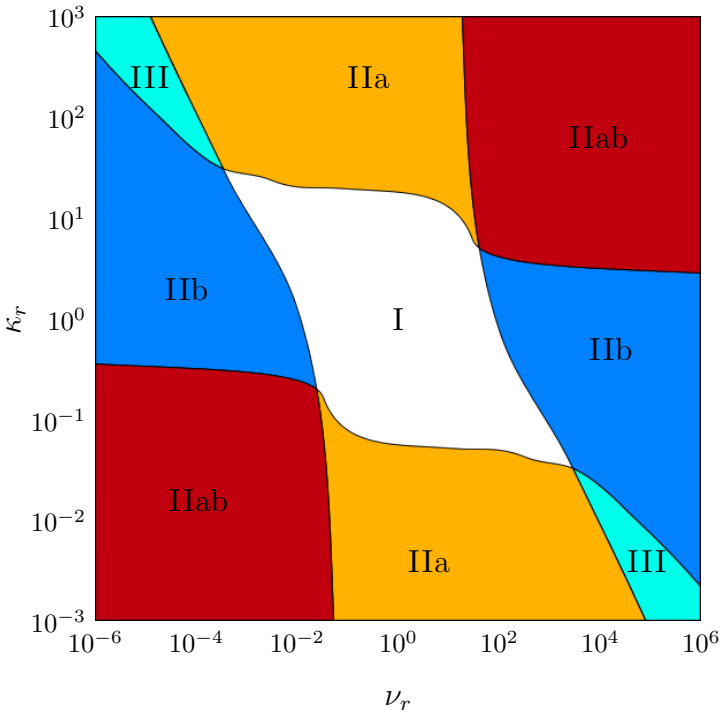

(a) $\delta = 1$

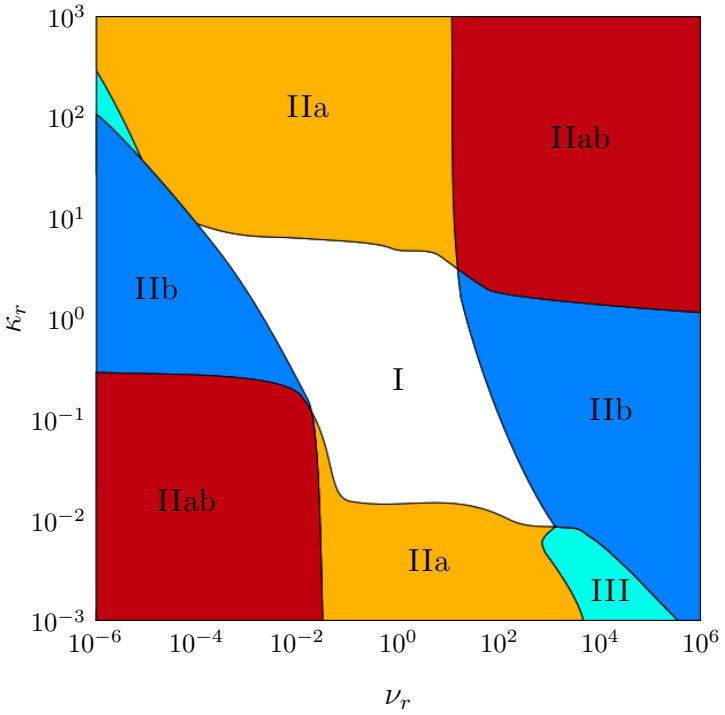

(b) $\delta = 0.5$

Figure 4.18: Approximate boundaries between distinct solution regimes for the case with (a) $\delta = 1$ and (b) $\delta = 0.5$. Regimes are labelled as follows: I whole-layer; IIa localised temperature perturbation; IIb localised velocity; IIab localised temperature and velocity; III segregated.

It is likely that the distinct regimes are characterised by different heat transport properties. In terms of the plasma problem this translates to different properties of the particle flux in the SOL, and the resulting plasma-wall interaction. As described in Section 2.3.6, while the values of diffusion coefficients in the core are given by neoclassical expressions (2.93), the neoclassical theory does not hold in the SOL, and it is conceivable that the values of transport coefficients in the SOL should lie between their classical and neoclassical values. If this is the case this would lead to a regime with $\nu_r \ll 1$ and $\kappa_r \ll 1$, with both the velocity and the temperature perturbation confined to the SOL. It should however be borne in mind that the purely convective model is an idealization of the core-SOL interaction, and does not include all of the physical effects present in the full plasma problem. Specifically there are two types of modifications required (these modification were described in the previous chapter). One is the addition of extra features accounting for plasma-related effects that act over both layers — these include a non-uniform basic state gradient and additional advective terms. The other is the physical representation of particle and energy losses in the regions of open field lines, which requires the inclusion of additional damping terms in the equations governing the SOL. This latter modification breaks the symmetry of the problem, and possibly inhibits the existence of modes localised to the SOL. In order to pursue these questions, in the next chapter we begin the investigation of the full two-region plasma problem.

Chapter 5

Two-region plasma problem: Linear theory

5.1 Introduction

Initial models of edge turbulence were restricted only to the SOL region (Bisai et al., 2004, 2005; Ghendrih et al., 2005, 2003; Sarazin and Ghendrih, 1998). These studies required an inclusion of a local turbulence drive within the SOL region. Subsequently, motivated by the concept that turbulence originates in the core, the simple SOL models have been extended to consider a configuration composed of the two regions — core and SOL — connected at the interface, as sketched in Figure 5.1. In the same spirit, in this chapter we extend the single region considerations of Chapter 3 and study a configuration that encompasses both the core and SOL regions. The two regions exhibit distinct dynamics parallel to the magnetic field; in the core, field lines are considered periodic in the parallel direction, while in the SOL the field lines end with a Debye sheath at a material surface. The presence of the sheath provides a sink for plasma particles and energy, and thus equations governing the dynamics in the SOL region contain heuristic dissipation terms associated with losses to the sheath. By contrast, these parallel loss terms do not come into the equations governing the core region, as the core plasma does not come in contact with material surfaces.

One of the most notable models in the edge-SOL drift fluid modelling campaign was ESEL (**E**dge-**S**OL **EL**ectrostatic; first appearance in Garcia et al. (2004)), a two-dimensional interchange model consisting of evolution equations for density, vorticity, and electron temperature. Computations using ESEL successfully reproduce intermittent ejection of coherent plasma blobs from the core region, and their subsequent propagation into the SOL. Furthermore, ESEL was successful in capturing properties of SOL turbulence, with reports of significant points of agreement with tokamak experiments on TCV (Garcia et al., 2007, 2005b), JET (Fundamenski et al., 2007), EAST (Yan et al., 2013), and MAST (Militello et al., 2012, 2013). In such simulations, synthetic probes are placed within the domain for data time series collection. The statistics of single-point recordings from synthetic probes are compared to statistics of experimental measurements recorded using Langmuir probes. The agreement between the simulation results and experimental

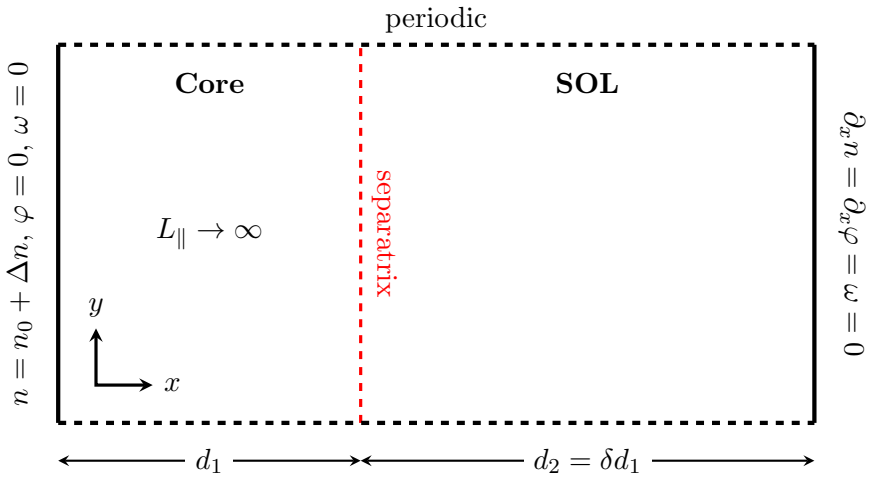

Figure 5.1: Schematic of the two region configuration.

data was established in terms of the following observations:

- radial profiles of time-averaged particle density, as well as probability distribution functions of particle density fluctuations and their statistical skewness and flatness;
- radial profiles of time-averaged radial particle flux, as well as probability distribution functions of particle flux fluctuations and their statistical skewness and flatness;
- the conditionally averaged pulse waveform shape in the far-SOL.

While the list of publications reporting studies of SOL turbulence using a two-region approach is extensive, there appear to be no reports on the linear stability properties of such models. With linear stability analysis being a valuable first step in studying complicated fluid systems, providing potentially important pointers to the nonlinear regime, it is surprising that in the case of edge-SOL modelling this step has been skipped over. Without knowledge of the stability threshold, it is difficult to judge how supercritical (i.e. how far into the nonlinear regime) are the simulations performed.

Additionally, even the simplest interchange models admit a substantial number of physical parameters such as: curvature drive, perpendicular diffusion coefficients, and parallel dissipation rates. These parameters differ from one publication to another depending on the machine and the particular discharge modelled. Differences between machine parameters (such as magnetic field, radius of curvature, safety factor, parallel connection length) and plasma conditions between different discharges (such as plasma density, electron and ion temperature) lead to a broad variability in terms of the values of physical model parameters used in the simulations. Table 5.1 highlights the variability in the values of particle diffusivity and ion viscosity in ESEL simulations. The diffusion coefficients undoubtedly affect the stability threshold of the system and the conditions at the onset. With the enormous variability in terms of physical parameters used, it is of interest to determine if there is a possibility of different regimes of behaviour.

Another source of variability comes from the differences in geometrical parameters of the numerical domain. One of these parameters is the ratio of the widths of the core and

Machine	D_n	μ	Reference
TCV	10^{-2}	10^{-2}	Garcia et al. (2005c, 2006c)
TCV	4.5×10^{-3}	2.5×10^{-2}	Garcia et al. (2005b)
TCV	4.5×10^{-3}	8.5×10^{-3}	Fundamenski et al. (2007)
JET	2.9×10^{-4}	3.1×10^{-3}	Fundamenski et al. (2007)
TCV	4.7×10^{-3}	VNR	Militello et al. (2012)
MAST	1.95×10^{-3}	VNR	Militello et al. (2012)
MAST	1.21×10^{-2}	1.13×10^{-1}	Militello et al. (2013)
EAST	1.8×10^{-3}	3.5×10^{-2}	Yan et al. (2013)

Table 5.1: Example values of normalised ion viscosity μ and particle diffusivity D_n used in ESEL simulations; VNR = values not reported.

SOL regions ($d_1 : d_2$ in Figure 5.1). With the core region being responsible for turbulence production, and the SOL responsible for dissipation to the sheath, it is reasonable to expect that this ratio of widths could play a role in terms of the onset of instability and subsequent nonlinear evolution of the system.

The other relevant geometrical parameter is the aspect ratio between the radial and the poloidal extent of the numerical domain. Analytically, periodicity in the poloidal direction allows for perturbations of arbitrary wavelength; numerically, the finite poloidal extent of the numerical box only allows wavelengths that fit the box. Knowledge of the critical wavelength at the onset of instability can therefore guide the choice of an appropriate aspect ratio, thereby avoiding the possibility of artificially constraining the intensity of turbulence by restricting the system to slower growing modes.

Owing to a large number of potentially relevant parameters it is of intrinsic theoretical interest to develop an understanding of how these parameters affect the onset of instability and to explore the possibility of the existence of distinct regimes of behaviour. Here we address this point through a linear stability analysis of a simple two-region interchange model that includes a simple description of open and closed field line regions based on the sheath dissipation closure.

5.2 Mathematical formulation

5.2.1 Governing equations

We consider a model of edge plasma in an outboard midplane region that encompasses both the core and the scrape-off layer, as depicted in Figure 5.1. Let d_1 and $d_2 = \delta d_1$ denote the thickness of the core region and the SOL region respectively, and $x = 0$ denote the position of the separatrix. The governing equations are (cf. (2.88), (2.89), (2.81), (2.82)):

$$\left(\frac{\partial}{\partial t} + \boldsymbol{v}_E \cdot \nabla\right) \omega = -\frac{g}{n}\frac{\partial n}{\partial y} + \nu_i \nabla^2 \omega + H(x)\Lambda_\omega, \tag{5.1}$$

$$\left(\frac{\partial}{\partial t} + \boldsymbol{v}_E \cdot \nabla\right) n = \frac{gn}{Bc_s^2}\frac{\partial \varphi}{\partial y} - \frac{g}{\Omega_i}\frac{\partial n}{\partial y} + D\nabla^2 n + H(x)\Lambda_n, \tag{5.2}$$

where

$$\Lambda_\omega = \frac{1}{l_\parallel} c_s \Omega_i \left(\frac{e}{T_e} \varphi \right), \tag{5.3}$$

$$\Lambda_n = \frac{c_s}{l_\parallel} n_0 - \frac{1}{l_\parallel} n c_s \left(1 - \frac{e}{T_e} \varphi \right), \tag{5.4}$$

describe parallel losses in the SOL due to sheath dissipation. Here, $H(x)$ is the Heaviside function, and n_0 is a constant reference SOL density. These equations are to be solved subject to the following radial boundary conditions (e.g. Garcia et al., 2005b; Militello et al., 2012):

$$\varphi = \omega = 0, \quad n = n_0 + \Delta n \qquad \text{at} \qquad x = -d_1, \tag{5.5}$$

$$\frac{\partial \varphi}{\partial x} = \omega = \frac{\partial n}{\partial x} = 0 \qquad \text{at} \qquad x = d_2. \tag{5.6}$$

The poloidal direction is considered periodic.

5.2.2 Nondimensionalisation

Conventionally, in edge plasma literature the governing equations appear in Bohm-normalised form obtained by scaling length with ρ_s, time with Ω_i^{-1}, density with n_0, potential with T_e/e. Equations (5.1), (5.2) scaled according to Bohm normalisation are

$$\frac{\mathrm{d}\omega}{\mathrm{d}t} = -\frac{\hat{g}}{n} \frac{\partial n}{\partial y} + \mu \nabla^2 \omega + H(x) \frac{\varphi}{L_\parallel}, \tag{5.7}$$

$$\frac{\mathrm{d}n}{\mathrm{d}t} = n \hat{g} \frac{\partial \varphi}{\partial y} - \hat{g} \frac{\partial n}{\partial y} + D_n \nabla^2 n + H(x) \left(\frac{n\varphi}{L_\parallel} - \frac{n - n_0}{L_\parallel} \right), \tag{5.8}$$

where

$$\hat{g} = \frac{g}{\rho_s \Omega_i^2} = \frac{2\rho_s}{R}, \qquad D_n = \frac{D}{D_{\mathrm{Bohm}}}, \qquad \mu = \frac{\nu_i}{D_{\mathrm{Bohm}}}, \tag{5.9}$$

are the normalised effective gravitational acceleration, particle diffusion and viscosity respectively, and $D_{\mathrm{Bohm}} = \rho_s^2 \Omega_i$ is Bohm diffusion.

Formally, equations (5.8), (5.7) constitute a two-region version of the model studied in Easy et al. (2014) (their equations (7), (8)). The model considered here is different from ESEL in terms of the following aspects. First, the ESEL model includes evolution of electron temperature, and in this respect it could be considered more complicated. Here, we consider the idealised isothermal limit whereby the electron temperature is assumed constant. Second, the ESEL model employs the so-called thin layer approximation (Madsen et al., 2016). This approximation neglects particle density variations in the polarization flux entering the vorticity equation and hence assumes a constant inertia of all fluid parcels irrespective of the local particle density. As a consequence, in the ESEL model, the density variation $1/n$ in front of the first term on the vorticity equation (5.7) is neglected (see for example equation (20c) in Garcia et al. (2005c)). Third, in ESEL the parallel losses of particle density and vorticity in the region of open field lines are modelled using the

vorticity advection closure (described in section 2.3.5). In our model, parametrisation of parallel losses is based on the sheath dissipation closure.

The Bohm-normalised equations (5.8), (5.7) evolve on the time scale given by the ion gyrofrequency, Ω_i^{-1}. On the other hand, according to the underlying assumptions behind drift-ordered models the system should evolve on a much slower time scale given by the dynamical frequency (the dynamical frequency is much smaller than the gyrofrequency, see (2.38)). Furthermore, in light of the analysis in Chapter 3, we expect the length scale of the convective cells to be comparable with the radial extent of the domain, and thus much larger than the gyroradius ρ_s. Therefore, we shall proceed with the alternative nondimensionalisation based on the diffusion timescale; scaling time with d_1^2/D, length with d_1, potential with BD, density with n_0, equations (5.1), (5.2) become

$$\frac{\mathrm{d}\omega}{\mathrm{d}t} = -Ra^* Pr \frac{1}{n}\frac{\partial n}{\partial y} + Pr\nabla^2\omega + H(x)\frac{L_\perp^2\,\Omega}{L_\parallel}\varphi. \tag{5.10}$$

$$\frac{\mathrm{d}n}{\mathrm{d}t} = \zeta n\frac{\partial\varphi}{\partial y} - \frac{Ra^* Pr}{\Omega}\frac{\partial n}{\partial y} + \nabla^2 n + H(x)\left(\frac{L_\perp^2}{L_\parallel}n\varphi - \frac{\Omega}{L_\parallel}(n-n_0)\right), \tag{5.11}$$

The dimensionless parameters are

$$Ra^* = \frac{g d_1^3}{D\nu_i}, \qquad Pr = \frac{\nu_i}{D}, \qquad \Omega = \frac{\Omega_i d_1^2}{D}, \qquad L_\parallel = \frac{l_\parallel}{\rho_s}, \qquad L_\perp = \frac{d_1}{\rho_s}, \qquad \zeta = \frac{2d_1}{R_c}. \tag{5.12}$$

These are related to the traditional Bohm plasma parameters (5.9) as follows:

$$Ra^* = \frac{\hat{g}L_x^3}{D_n\mu}, \qquad Pr = \frac{\mu}{D_n}, \qquad \Omega = \frac{L_x^2}{D_n}, \qquad \zeta = \hat{g}L_x, \qquad L_\perp = L_x, \tag{5.13}$$

where L_x is the Bohm-normalised radial length of the core region under consideration.

5.3 Linear stability analysis

5.3.1 Basic state

We consider a steady basic state with plasma at rest, and assume that the basic state plasma density varies as a function only of the radial coordinate. We describe the basic state by upper case variables; thus $\Phi_k = 0$ and $n_k = N_k(x)$. The basic state density distribution is given by

$$\frac{\mathrm{d}^2 N_1}{\mathrm{d}x^2} = 0, \qquad -1 \le x < 0, \tag{5.14}$$

$$\frac{\mathrm{d}^2 N_2}{\mathrm{d}x^2} - \frac{\Omega}{L_\parallel}N_2 = -\frac{\Omega}{L_\parallel}n_0, \qquad 0 < x \le \delta, \tag{5.15}$$

where indices $k = 1, 2$ denote core and SOL regions respectively. Boundary conditions on density (cf. (5.5), (5.6)), and the continuity of density and density flux at the separatrix

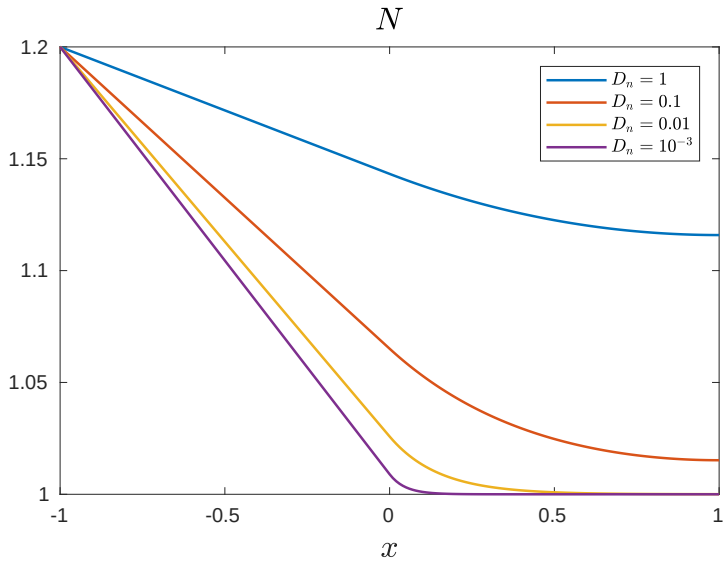

Figure 5.2: Basic state profiles for varying values of D_n; other parameters fixed $\Delta n = 0.2$, $n_0 = 1$, $\delta = 1$, $L_\perp = 50$, $L_\parallel = 5500$.

require that

$$N_1 = n_0 + \Delta n \qquad \text{at} \qquad x = -1, \tag{5.16}$$

$$\frac{\mathrm{d}N_2}{\mathrm{d}x} = 0 \qquad \text{at} \qquad x = \delta, \tag{5.17}$$

$$N_1 = N_2, \qquad \frac{\mathrm{d}N_1}{\mathrm{d}x} = \frac{\mathrm{d}N_2}{\mathrm{d}x} \qquad \text{at} \qquad x = 0. \tag{5.18}$$

Solving (5.14), (5.15) subject to conditions (5.16)–(5.18) yields

$$N_1 = n_0 + \Delta n \left(1 + A_1 \left(x + 1\right)\right), \tag{5.19}$$

$$N_2 = n_0 + \Delta n \left(A_2 \cosh(\alpha x) + B_2 \sinh(\alpha x)\right), \tag{5.20}$$

where $\alpha = (\Omega / L_\parallel)^{1/2} = L_\perp / (D_n L_\parallel)^{1/2}$ and

$$A_1 = \frac{-\alpha \tanh(\alpha\delta)}{(1 + \alpha \tanh(\alpha\delta))}, \qquad A_2 = \frac{1}{(1 + \alpha \tanh(\alpha\delta))}, \qquad B_2 = \frac{-\tanh(\alpha\delta)}{(1 + \alpha \tanh(\alpha\delta))}. \tag{5.21}$$

Figure 5.2 shows plots of the basic state density distribution for varying values of D_n. We note that the basic state depends explicitly on the value of the particle diffusivity D_n and parallel connection length $L_\parallel$. This indicates that the equilibrium density profile arises from the balance between perpendicular diffusion and parallel losses. In particular, when diffusivity D_n is small (α is large), SOL is loss dominated, and the density profile in the SOL approaches uniform reference density (as $\alpha x \to \infty$, $N_2 \to n_0$); this is illustrated in Figure 5.2 for $D_n = 10^{-3}$. On the other hand, for sufficiently large D_n (small α) diffusion dominates over parallel losses and the equilibrium density in the SOL exceeds the constant reference value, as seen for the case $D_n = 1$.

5.3.2 Linear perturbation equations

On introducing the change of variable $\theta = \log(n/n_0)$, as in Section 3.2, the governing equations (5.11), (5.10) become

$$\frac{\mathrm{d}\omega}{\mathrm{d}t} = -Ra^* Pr \frac{\partial \theta}{\partial y} + Pr\nabla^2\omega + H(x)\frac{L_\perp^2}{L_\parallel}\Omega\varphi. \tag{5.22}$$

$$\frac{\mathrm{d}\theta}{\mathrm{d}t} = \zeta\frac{\partial\varphi}{\partial y} - \frac{Ra^* Pr}{\Omega}\frac{\partial\theta}{\partial y} + \nabla^2\theta + |\nabla\theta|^2 + H(x)\left(\frac{L_\perp^2}{L_\parallel}\varphi - \frac{\Omega}{L_\parallel}\left(1-\exp(\theta)\right)\right), \tag{5.23}$$

Note that the basic state equation (5.15) written in terms of $\Theta_2(x) = \log(N_2(x)/n_0)$ becomes

$$\Theta_2'' + \Theta_2'^2 - \frac{\Omega}{L_\parallel}\left(1-\exp(-\Theta_2)\right) = 0. \tag{5.24}$$

We now consider small perturbations to this basic state, expressing the potential, vorticity and log-density in the perturbed state by φ_k, ω_k and $\Theta_k + \theta_k$ respectively. We substitute these expressions into equations (5.22) and (5.23). In the SOL region, the log-density equation (5.23) becomes

$$\begin{aligned}\frac{\partial\theta_2}{\partial t} + \mathbf{v}_E\cdot\nabla(\Theta_2+\theta_2) = \zeta\frac{\partial\varphi_2}{\partial y} - \frac{Ra^* Pr}{\Omega}\frac{\partial\theta_2}{\partial y} + \left(\nabla^2\theta_2 + (\nabla\theta_2)^2 + \Theta_2'' + \Theta_2'^2 + 2\frac{\partial\theta_2}{\partial x}\Theta_2'\right)\\ + \left(\frac{L_\perp^2}{L_\parallel}\varphi_2 - \frac{\Omega}{L_\parallel}\left(1-\exp(-(\Theta_2+\theta_2))\right)\right)\end{aligned} \tag{5.25}$$

We note that

$$\exp(-(\Theta_2+\theta_2)) = \exp(-\Theta_2)\left(1-\theta_2\ldots\right) = \exp(-\Theta_2) - \frac{n_0}{N_2(x)}\theta_2 + \mathcal{O}\left(\theta_2^2\right). \tag{5.26}$$

Using (5.24) and (5.26) we obtain the linearised version of (5.25):

$$\frac{\partial\theta_2}{\partial t} = \left(\Theta_2' + \zeta\right)\frac{\partial\varphi_2}{\partial y} - \frac{Ra^* Pr}{\Omega}\frac{\partial\theta_2}{\partial y} + \nabla^2\theta_2 + 2\frac{\partial\theta_2}{\partial x}\Theta_2' + \frac{L_\perp^2}{L_\parallel}\varphi_2 - \frac{1}{N_2(x)}\frac{\Omega}{L_\parallel}\theta_2. \tag{5.27}$$

The full set of linearised perturbation equations is therefore

$$\frac{\partial\omega_1}{\partial t} = -Ra^* Pr\frac{\partial\theta_1}{\partial y} + Pr\nabla^2\omega_1, \tag{5.28}$$

$$\frac{\partial\theta_1}{\partial t} = \left(\Theta_1'(x) + \zeta\right)\frac{\partial\varphi_1}{\partial y} - \frac{Ra^* Pr}{\Omega}\frac{\partial\theta_1}{\partial y} + \nabla^2\theta_1 + 2\Theta_1'(x)\frac{\partial\theta_1}{\partial x}, \tag{5.29}$$

$$\frac{\partial\omega_2}{\partial t} = -Ra^* Pr\frac{\partial\theta_2}{\partial y} + Pr\nabla^2\omega_2 + \frac{L_\perp^2}{L_\parallel}\Omega\varphi_2, \tag{5.30}$$

$$\frac{\partial\theta_2}{\partial t} = \left(\Theta_2'(x) + \zeta\right)\frac{\partial\varphi_2}{\partial y} - \frac{Ra^* Pr}{\Omega}\frac{\partial\theta_2}{\partial y} + \nabla^2\theta_2 + 2\Theta_2'(x)\frac{\partial\theta_2}{\partial x} - \frac{1}{N_2(x)}\frac{\Omega}{L_\parallel}\theta_2 + \frac{L_\perp^2}{L_\parallel}\varphi_2. \tag{5.31}$$

The perturbation variables satisfy the following boundary conditions (cf. (5.5), (5.6))

$$\varphi = \omega = \theta = 0 \qquad \text{at} \qquad x = -1, \tag{5.32}$$

$$\partial_x \varphi = \omega = \partial_x \theta = 0 \qquad \text{at} \qquad x = \delta. \tag{5.33}$$

Additionally, continuity of velocity, tangential and normal stress, density and density flux are satisfied at the separatrix:

$$\begin{gathered}
\varphi_1 = \varphi_2, \quad \frac{\partial \varphi_1}{\partial x} = \frac{\partial \varphi_2}{\partial x}, \\
\frac{\partial^2 \varphi_1}{\partial x^2} - \frac{\partial^2 \varphi_1}{\partial y^2} = \frac{\partial^2 \varphi_2}{\partial x^2} - \frac{\partial^2 \varphi_2}{\partial y^2}, \\
\frac{\partial}{\partial x}\left(\frac{\partial^2 \varphi_1}{\partial x^2} + 3\frac{\partial^2 \varphi_1}{\partial y^2}\right) = \frac{\partial}{\partial x}\left(\frac{\partial^2 \varphi_2}{\partial x^2} + 3\frac{\partial^2 \varphi_2}{\partial y^2}\right), \\
\theta_1 = \theta_2, \quad \frac{\partial \theta_1}{\partial x} = \frac{\partial \theta_2}{\partial x} \qquad \text{at} \qquad x = 0.
\end{gathered} \tag{5.34}$$

5.3.3 Marginal stability analysis

We seek normal mode solutions of the form

$$\varphi_k(x,y,t) = \hat{\varphi}_k(x) \exp\left(iky + \sigma t\right) + c.c., \qquad \theta_k(x,y,t) = \hat{\theta}_k(x) \exp\left(iky + \sigma t\right) + c.c., \tag{5.35}$$

where k is the poloidal wavenumber and σ is the growth rate, which can be in general complex: $\sigma = s + i\gamma$; s, $\gamma \in \mathbb{R}$. Substituting these expressions into equations (5.28)–(5.31) yields

$$\sigma\left(\mathcal{D}^2 - k^2\right)\hat{\varphi}_1 = -ikRa^* Pr\hat{\theta}_1 + Pr\left(\mathcal{D}^4 - 2k^2\mathcal{D}^2 + k^4\right)\hat{\varphi}_1, \tag{5.36}$$

$$\sigma\hat{\theta}_1 = ik\left(\Theta_1'(x) + \zeta\right)\hat{\varphi}_1 - ik\frac{Ra^* Pr}{\Omega}\hat{\theta}_1 + \left(\mathcal{D}^2 - k^2\right)\hat{\theta}_1 + 2\Theta_1'(x)\mathcal{D}\hat{\theta}_1, \tag{5.37}$$

$$\sigma\left(\mathcal{D}^2 - k^2\right)\hat{\varphi}_2 = -ikRa^* Pr\hat{\theta}_2 + Pr\left(\mathcal{D}^4 - 2k^2\mathcal{D}^2 + k^4\right)\hat{\varphi}_2 + \frac{L_\perp^2 \Omega}{L_\parallel}\hat{\varphi}_2, \tag{5.38}$$

$$\sigma\hat{\theta}_2 = ik\left(\Theta_2'(x) + \zeta\right)\hat{\varphi}_2 - ik\frac{Ra^* Pr}{\Omega}\hat{\theta}_2 + \left(\mathcal{D}^2 - k^2\right)\hat{\theta}_2 + 2\Theta_2'(x)\mathcal{D}\hat{\theta}_2 - \frac{1}{N_2(x)}\frac{\Omega}{L_\parallel}\hat{\theta}_2 + \frac{L_\perp^2}{L_\parallel}\hat{\varphi}_2. \tag{5.39}$$

Boundary and separatrix conditions (5.32)–(5.34) become

$$\varphi_1 = \mathcal{D}^2\varphi_1 = \theta_1 = 0 \quad \text{at} \quad x = -1, \tag{5.40}$$

$$\mathcal{D}\varphi_2 = \left(\mathcal{D}^2 - k^2\right)\varphi_2 = \mathcal{D}\theta_2 = 0 \quad \text{at} \quad x = \delta, \tag{5.41}$$

$$\begin{gathered}
\varphi_1 = \varphi_2, \quad \mathcal{D}\varphi_1 = \mathcal{D}\varphi_2, \\
\left(\mathcal{D}^2\varphi_1 + k^2\varphi_1\right) = \left(\mathcal{D}^2\varphi_2 + k^2\varphi_2\right), \\
\left(\mathcal{D}^3\varphi_1 - 3k^2\mathcal{D}\varphi_1\right) = \left(\mathcal{D}^3\varphi_2 - 3k^2\mathcal{D}\varphi_2\right), \\
\theta_1 = \theta_2, \quad \mathcal{D}\theta_1 = \mathcal{D}\theta_2 \quad \text{at} \quad x = 0.
\end{gathered} \tag{5.42}$$

Equations (5.36)–(5.39), subject to boundary and separatrix condtions (5.40) – (5.42), constitute an eigenvalue boundary value problem. We solve the eigenvalue problem numerically using the shooting method (Stoer and Bulirsch, 2013); we shoot from the boundaries with matching imposed at $x = 0$. As in the case of the one region problem in Chapter 3, here the principle of exchange of stabilities is not valid, and the marginal state is characterised by a non-zero frequency of oscillation. We are interested in the onset of instability: thus for each wavenumber k, we seek the density difference Δn for which $Re(\sigma) = 0$. In particular, we seek the minimal, critical, density difference Δn_c, and the accompanying critical wavenumber at which this minimum is attained.

5.3.4 Parameters

As outlined briefly in the introduction to this chapter (Section 5.1), differences in plasma conditions between discharges leads to variability in the values of physical parameters. Figure 5.3 illustrates the variation of normalised particle diffusivity D_n, normalised ion viscosity μ, and normalised effective gravitational acceleration $\hat{g}$, with respect to electron temperature and plasma density. These parameter values have been evaluated using neoclassical expressions introduced in Section 2.3.6, assuming $T_i = T_e$ and MAST machine parameters: $q = 7$, $B = 0.5$T, $R = 0.85$m. Clearly, D_n and μ admit a considerable range of values depending on plasma conditions, varying between 10^{-4} – 10^{-1} and 10^{-3} – 1 respectively in the most extreme cases. Variation in the possible values of $\hat{g}$, which is independent of plasma density, is modest in comparison.

In the stability analysis below, we therefore focus on the effect of varying D_n and μ, and fix $\hat{g} = 2.4 \times 10^{-3}$, $L_\perp = 50$, $L_\parallel = 5500$. Recall from (5.13) that varying D_n affects Ra^*, Pr and Ω, whereas varying μ only affects Pr.

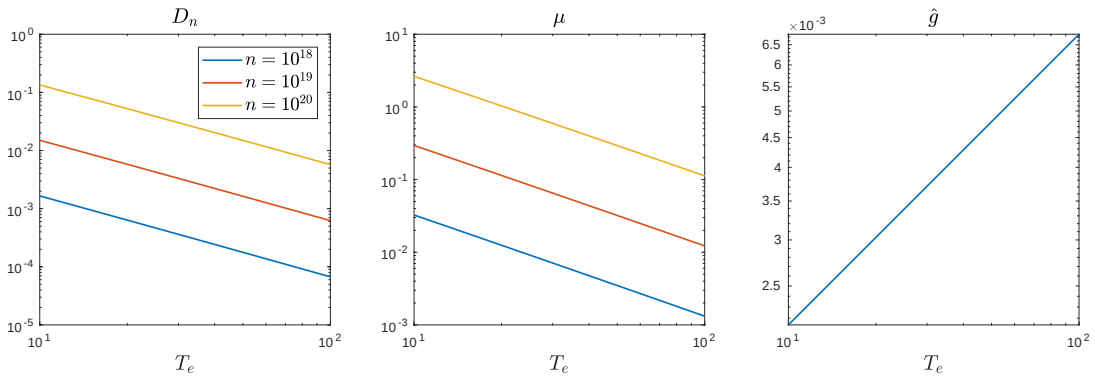

(a) (b) (c)

Figure 5.3: Plots of normalised particle diffusivity D_n (a), normalised ion viscosity μ (b), and normalised effective gravitational acceleration $\hat{g}$ (c), as a function of electron temperature T_e (eV), for different values of plasma density n (m^{-3}).

5.3.5 Necessary conditions for instability

Before proceeding with the analysis of results, we utilise the analogy with the thermal convection problem in order to gain insight about a necessary condition for the onset of

instability in the plasma problem. Recall the linear two-dimensional convection equations (cf. (2.117), (2.118)):

$$\frac{\partial \nabla^2 \psi}{\partial t} = -Ra^* Pr \frac{\partial \theta}{\partial y} + Pr \nabla^2 \nabla^2 \psi, \tag{5.43}$$

$$\frac{\partial \theta}{\partial t} = \frac{\mathrm{d}T}{\mathrm{d}z} \frac{\partial \psi}{\partial y} + \nabla^2 \theta. \tag{5.44}$$

A necessary condition for instability in convection is an adverse basic state temperature gradient $\frac{\mathrm{d}T}{\mathrm{d}z} < 0$ — i.e. an unstable temperature stratification. In the classical convection problem $\frac{\mathrm{d}T}{\mathrm{d}z}$ is negative and uniform. Motion is driven by a combined effect of the buoyancy drive term and the advection of the basic state temperature gradient (respectively the first terms on the right hand side in (5.43) and (5.44)). In the absence of a temperature gradient, or when the temperature increases with height (stable stratification), convective motions will not onset.

Comparing (5.44) with (5.29), (5.31) we recognise that $(\Theta' + \zeta)$ is an analogue of $\frac{\mathrm{d}T}{\mathrm{d}z}$. Therefore, in the plasma problem, a necessary condition for instability is that $(\Theta' + \zeta)$ is negative somewhere. Note however that the nature of the basic state density distribution is such that $(\Theta' + \zeta)$ changes sign within the domain. Hence, within the domain there are regions of unstable stratification adjacent to regions of stable stratification. Such a situation is commonly encountered in the studies of penetrative convection (e.g. Saslaw and Schwarzschild, 1965; Veronis, 1963).

Penetrative convection refers to the phenomena that occur whenever convection in a thermally unstable fluid layer penetrates into adjacent stable layers. Penetration of convection across the interface between stable and unstable layers is of astrophysical importance, as stellar convection zones are commonly sandwiched between stably stratified regions. Penetration of cold plumes from the outer convective zone of the sun into the upper layers of the tachocline can generate internal gravity waves, and thus can play an important role in the turbulent transport of momentum in the tachocline (e.g. Hurlburt et al., 1986). Clearly we can observe similarities between this picture and the phenomena in the edge plasma, where coherent blobs created in the inner edge region through interchange instability propagate into the stably stratified scrape-off layer.

5.4 Onset of instability

5.4.1 The case of equal region widths ($\delta = 1$)

We begin with the case where the core and SOL regions are of equal width, i.e. $\delta = 1$, and consider the effect of varying the particle diffusivity D_n and ion viscosity μ. Figures 5.4a and 5.4b show the variation of the critical density difference, Δn_c, with respect to the particle diffusivity D_n and ion viscosity μ, respectively. In both cases, we observe that reducing the diffusion parameters reduces the critical density difference required for the onset of instability. In the case of the particle diffusivity this reduction in Δn_c comes as the result of increasing the magnitude of the interchange drive in the vorticity equation

(first term on the right hand side of eqns. (5.28), (5.30)). In the case of ion viscosity, it is a result of decreasing the magnitude of the coefficient in front of the viscosity term in the vorticity equation. Note that decreasing D_n also results in increasing the coefficient of the viscous term as $Pr = \mu/D_n$; however, the coefficient of the interchange term ($\sim D_n^{-2}$) increases substantially faster.

The variation of the critical wavenumber k_c with respect to the particle diffusivity D_n and ion viscosity μ is shown in Figures 5.4c and 5.4d respectively. Let us first consider the variation with respect to μ (Figure 5.4d). Figure 5.5 shows contour plots of potential φ, vorticity ω, and log-density θ perturbations, at fixed $D_n = 0.1$ and decreasing values of μ. Also plotted are the underlying basic state log-density gradient Θ' profiles for each case, in which the convectively unstable region is highlighted. When $\mu = 1$, the perturbations take the form of large cells whose wavelength is comparable to the width of the convectively unstable region. This can be seen in Figure 5.5a: contours of the potential perturbation φ, and thus the fluid motion, are confined to within the range of the convectively unstable region. Note, however, that the density perturbation extends slightly into the quiescent region owing to diffusion. We observed similar behaviour in the two-layer convection problem in the case of large viscosity contrast where the temperature perturbation extended into the dormant viscous layer. On first decreasing μ, the critical wavenumber increases slowly indicating a shift toward narrower cells. This effect is tied in with the decrease in Δn_c, which, broadly speaking, shifts the basic state gradient Θ' upwards, thus narrowing the extent of the convectively unstable region (Figure 5.5b). Therefore the increase in k_c reflects the reduction in the cell size due to the shrinking convective region. When μ is decreased below some critical value a second stable region appears and the convectively unstable region becomes localised near the separatrix, sandwiched by convectively stable regions on both sides (Figure 5.5c). This drastic narrowing of the unstable region is accompanied by a pronounced increase in k_c, which reflects a change to smaller cells localised near the separatrix.

The variation of k_c with respect to D_n follows a similar pattern with one addition: varying D_n now also changes the shape of the basic state gradient. In particular, as D_n is reduced, the transition between Θ'_1 and Θ'_2 becomes sharper. This additional factor plays a role in affecting the structure of the critical modes. This is most clearly visible in contours of θ in Figure 5.6. When $D_n = 1$ the unstable region covers all of the core as well as the majority of the SOL region, and θ perturbations penetrate the entire domain (Figure 5.6a). As seen in Figure 5.6b, on reducing D_n, the width of the unstable region narrows, and with it the extent of θ perturbation, which now only slightly penetrates the convectively stable SOL. As we decrease D_n further (Figure 5.6c), a second stable region appears, and θ perturbations become localised near the separatrix where the basic state is convectively unstable.

Figure 5.7 shows the variation of the frequency at the onset of instability. The frequency is negative which implies propagation of convective cells in the positive y direction. Generally, the magnitude of the frequency increases as D_n is decreased (at a fixed μ). This is consistent with our expectations from the reduced single region plasma problem (Section

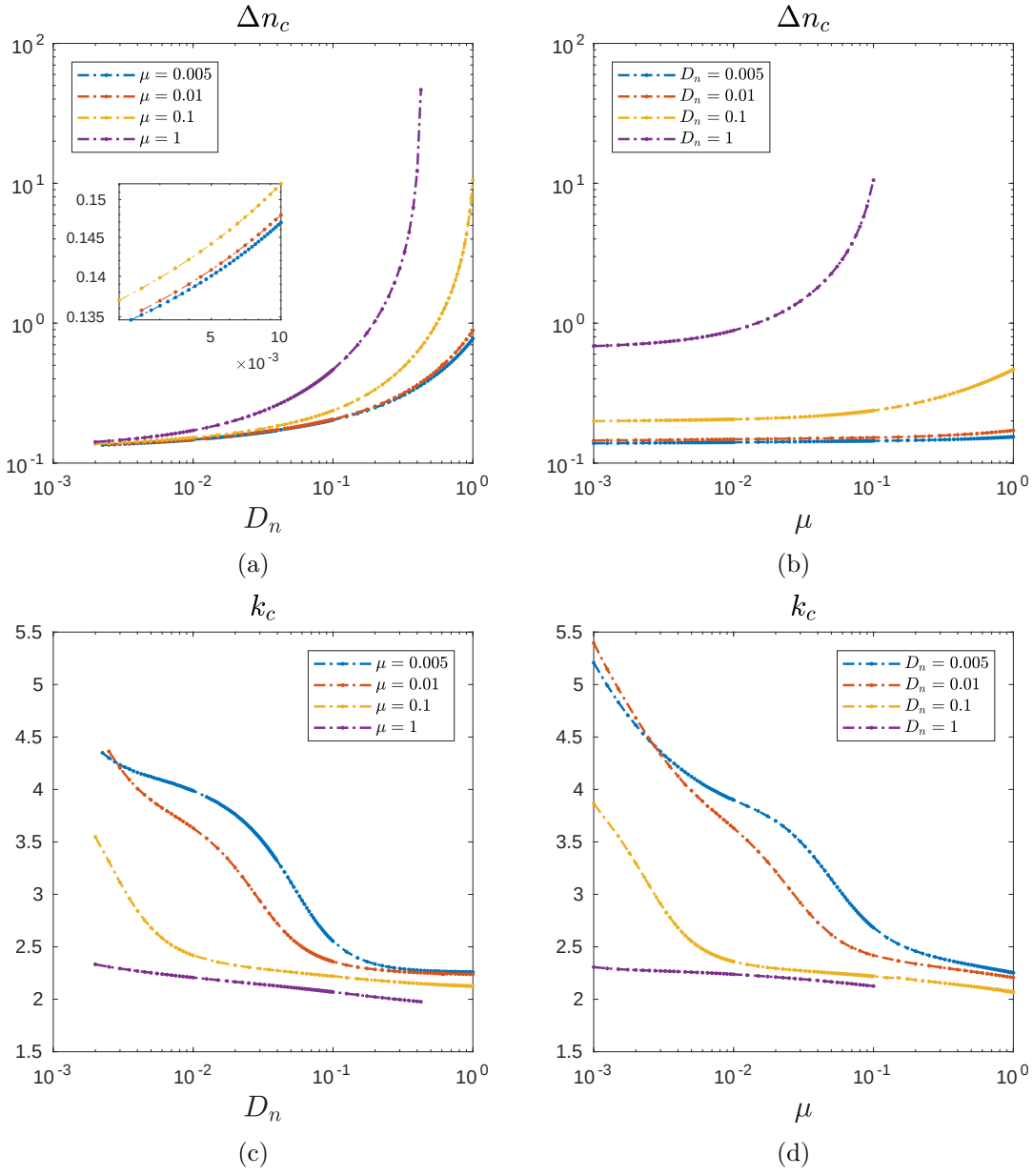

Figure 5.4: Variation of the critical density difference *(top row)*, and the corresponding critical wavenumber *(bottom row)* at the onset of instability with respect to the particle diffusivity D_n ((a) and (c)), and the ion viscosity μ ((b) and (d)).

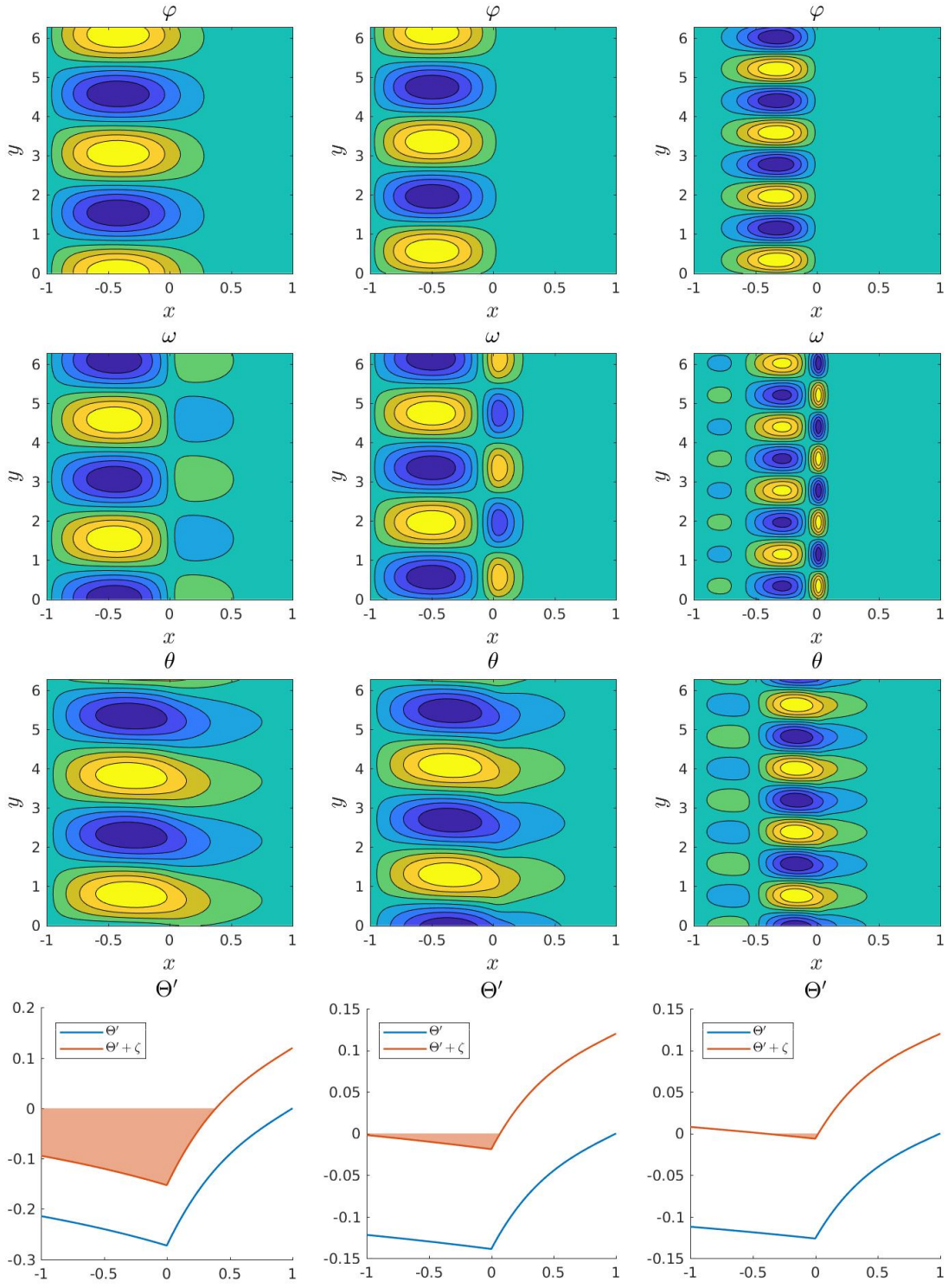

(a) $\mu = 1$ (b) $\mu = 0.05$ (c) $\mu = 10^{-3}$

Figure 5.5: From top to bottom: contours of potential φ, vorticity ω, log-density θ perturbations, and the underlying basic state log-density gradient Θ' profiles with the convectively unstable region highlighted. Particle diffusivity is fixed at $D_n = 0.1$, ion viscosity μ decreases from left to right.

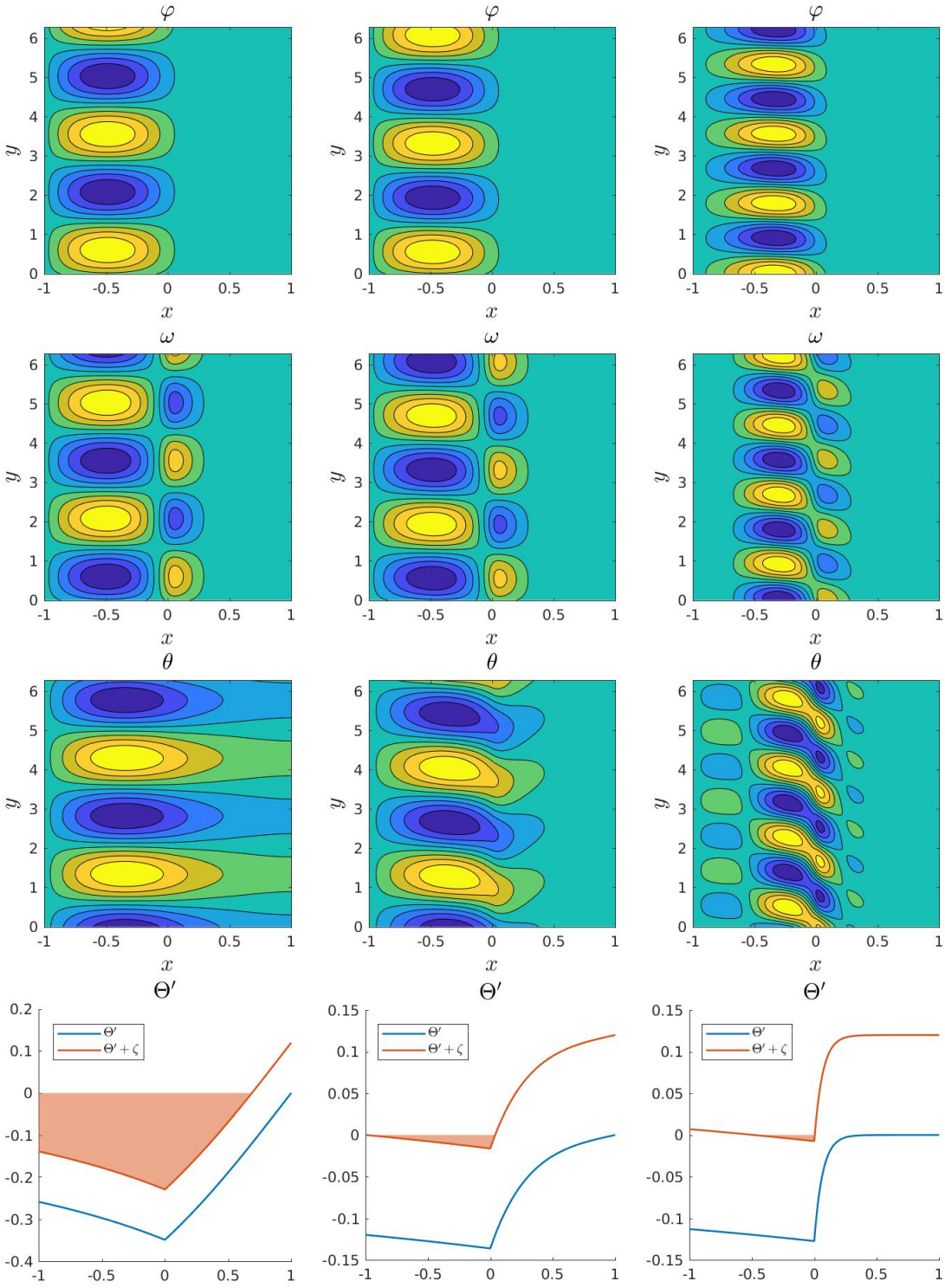

(a) $D_n = 1$ (b) $D_n = 0.04$ (c) $D_n = 2 \times 10^{-3}$

Figure 5.6: From top to bottom: contours of potential φ, vorticity ω, log-density θ perturbations, and the underlying basic state log-density gradient Θ' profiles with the convectively unstable region highlighted. Ion viscosity is fixed at $\mu = 0.1$, particle diffusivity D_n decreases from left to right.

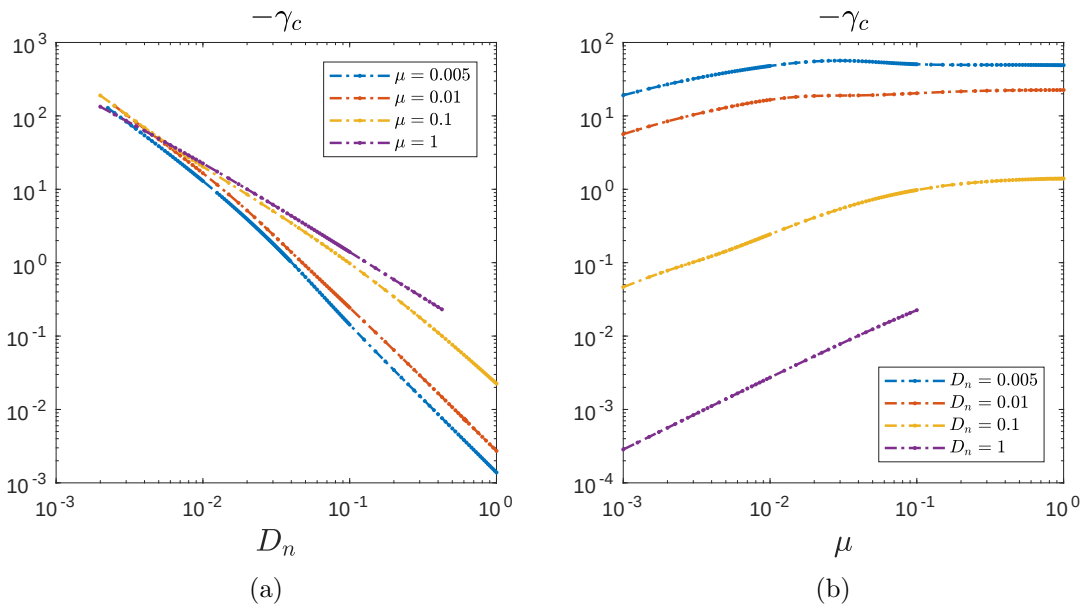

Figure 5.7: Variation of the frequency of oscillation associated with the critical mode with respect to the particle diffusivity D_n (a), and ion viscosity μ (b).

3.3.3), where we found that the frequency at the onset of instability varies roughly like $\gamma \sim -\mu D_n^{-2}$. Following this we would expect the magnitude of the frequency to decrease as μ is decreased. This indeed seems to be the overall trend, although for small D_n (e.g. $D_n = 0.005$) this decrease is not monotonic.

5.4.2 The case of unequal region widths ($\delta \neq 1$)

We now consider the case where the two regions are of different width. Figure 5.8 shows the variation of the critical density difference Δn_c, critical wavenumber k_c, and frequency γ_c at the onset with respect to δ, for a few select (D_n, μ) parameter cases. Evidently Δn_c is decreasing with δ (Figure 5.8a). Furthermore, as δ is decreased toward 0, we expect Δn_c to increase without limit. From equation (5.19) we see that as $\delta \to 0$, $A_1 \to 0$, and

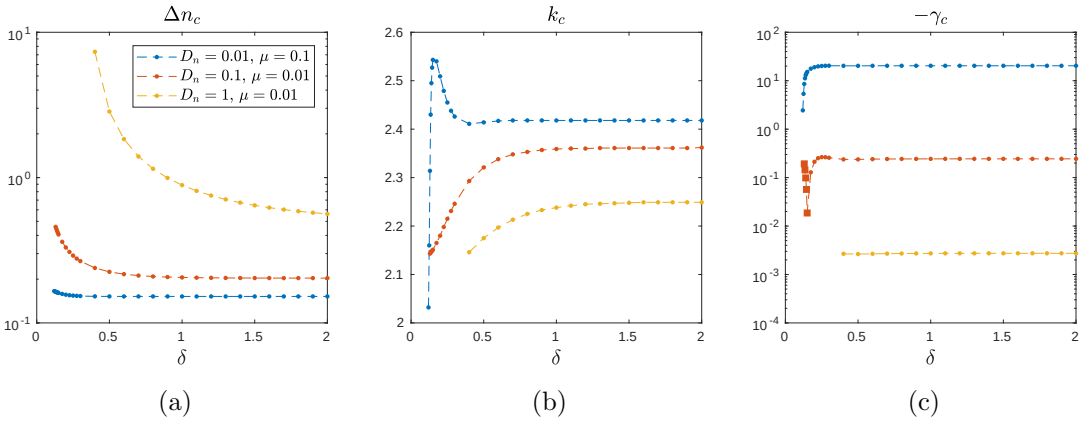

Figure 5.8: Variation of (a) the critical density difference, (b) the corresponding critical wavenumber, and (c) the frequency at the onset of instability with respect to the width ratio δ. In (c) square markers indicate positive frequency, i.e. $-\gamma < 0$.

the basic state density tends to a uniform distribution $N_1 \to n_0 + \Delta n$. In the absence of an adverse basic state density gradient the necessary condition for instability cannot be satisfied, and the system is linearly stable for arbitrarily large Δn. The frequency γ_c of the critical mode increases rapidly as $\delta \to 0$. In particular, note that in the case with $D_n = 0.1$, $\mu = 0.01$ the frequency changes sign, from negative to positive, as δ is decreased. This implies a reversal in the direction of propagation of perturbations. It also implies that there exists (at least for this case) a value of δ where the instability is non-oscillatory i.e. $\gamma = 0$.

As δ is decreased from 1 we also observe a tendency of the instability to favour perturbations with larger wavelength, as evidenced by decreasing critical wavenumber for sufficiently small δ (Figure 5.8b). In two of the cases ($D_n = 0.1$, $\mu = 0.01$ and $D_n = 1$, $\mu = 0.01$) this decrease in the critical wavenumber is monotonic, in the other ($D_n = 0.01$, $\mu = 0.1$) it is preceded by a small increase in k_c. In the two former cases, this change in the preferred length scale could again be tied to the extent of the convectively unstable region. Figure 5.9 shows contour plots of potential φ, vorticity ω, and log-density θ perturbations, along with the underlying basic state log-density gradient Θ' profiles for $D_n = 1$, $\mu = 0.01$ and decreasing values of δ. As seen in the bottom two rows of Figure 5.9, as δ is decreased, the extent of the convectively unstable region grows in proportion to the total width of the domain, thus favouring perturbations with larger wavelength.

Contour plots of the critical mode for the case that exhibits non-monotonic variation of k_c with respect to δ are show in Figure 5.10. Clearly, the structure of the solutions in this case is markedly different to that described immediately above. For a start, the underlying basic state density is such that the convectively unstable region is localised near the separatrix, sandwiched between two stable regions on either side (see bottom row of Figure 5.10). For $\delta = 0.6$ (before the peak in Figure 5.8b) the fluid motion is confined in the core region and the density perturbations are localised near the separarix, as seen in the contours of φ and θ in Figure 5.10a. Recall from Figure 5.8b that as δ is decreased, the critical wavenumber increases initially to a maximum, beyond which further decrease in δ leads to an abrupt decrease in k_c. Contour plots of the critical modes near the maximum of k_c ($\delta = 0.15$) and beyond ($\delta = 0.12$) are shown in Figures 5.10b and 5.10c respectively. There, we observe the fluid motion is no longer confined to the core region, but instead extends over the whole width of the domain. Moreover, the critical mode is now characterised by non-zero flow velocities on the right boundary. The peak of the density perturbation is no longer in the region where the basic state is convectively unstable, but instead is localised to the thin SOL.

Finally, we observe that as δ is increased, the critical density difference, the critical wavenumber and the frequency quickly tend toward asymptotic values associated with the limit of $\delta \to \infty$. In this limit the problem reduces to something akin to convection in a layer of fluid bounded from one side by an infinite expanse of stably stratified fluid.

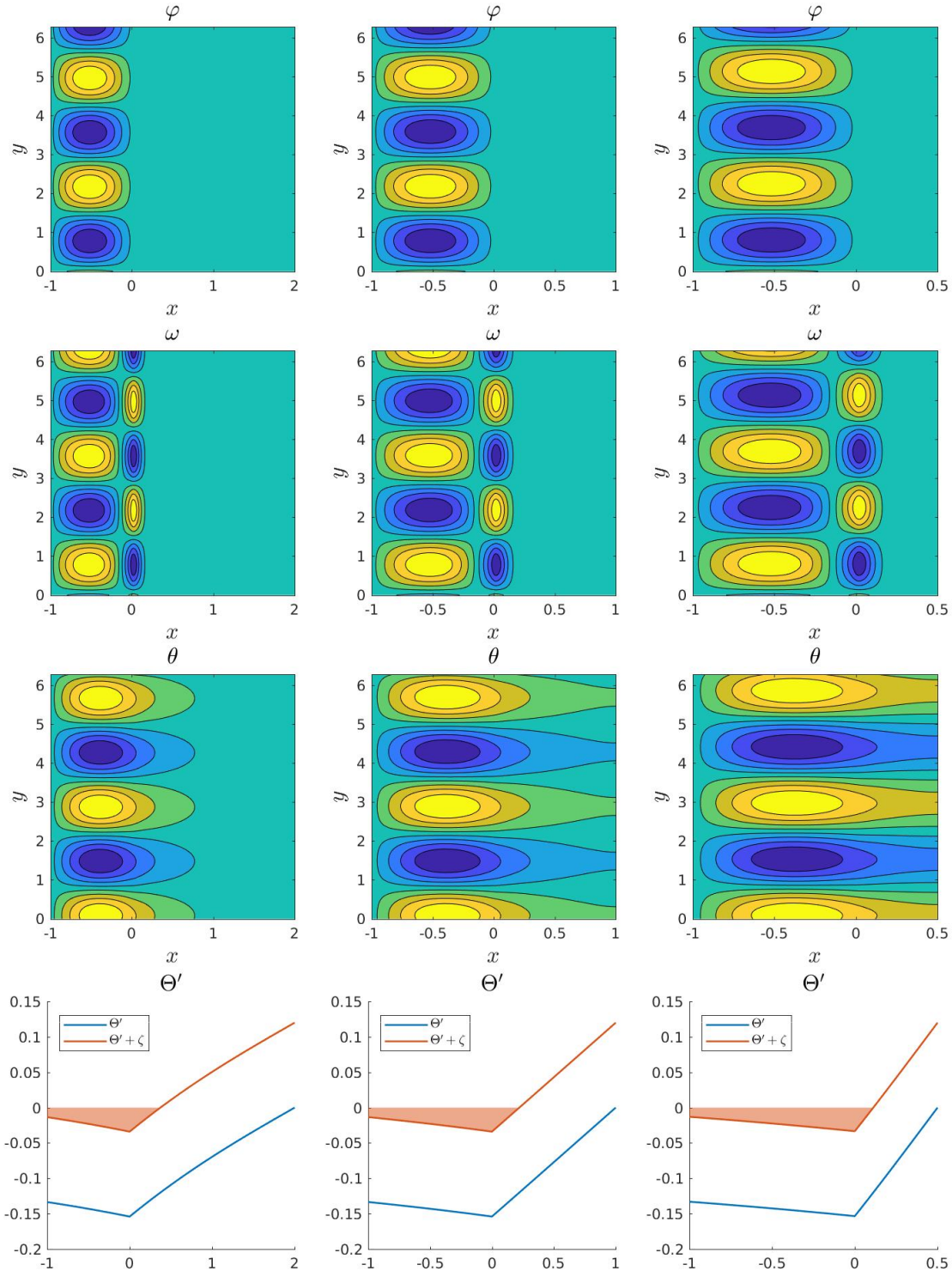

(a) $\delta = 2$ (b) $\delta = 1$ (c) $\delta = 0.5$

Figure 5.9: From top to bottom: contours of potential φ, vorticity ω, log-density θ perturbations, and the underlying basic state log-density gradient Θ' profiles with the convectively unstable region highlighted. Ion viscosity and particle diffusivity are fixed at $D_n = 1$, $\mu = 0.01$, width ratio δ decreases from left to right.

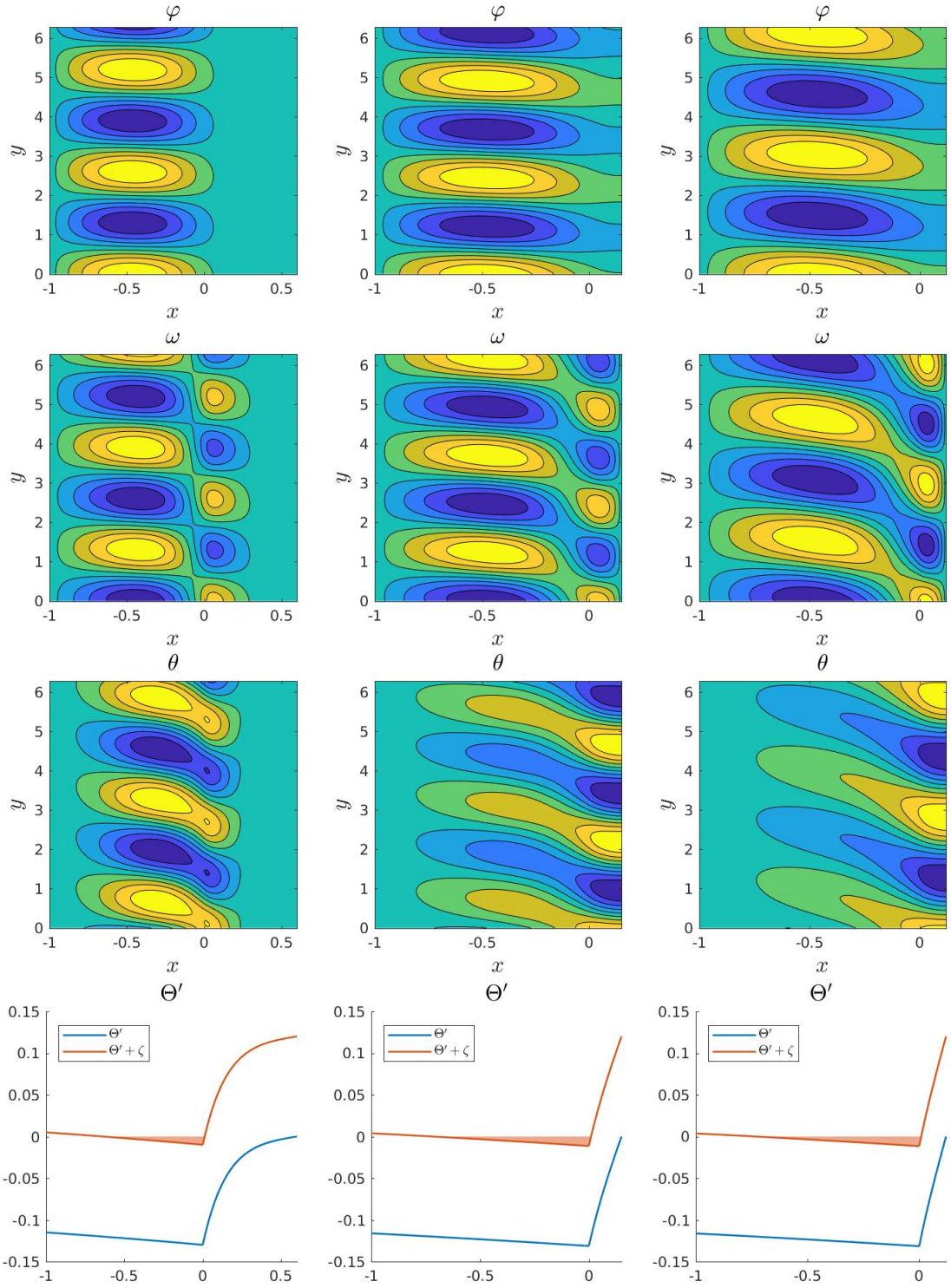

(a) $\delta = 0.6$ (b) $\delta = 0.15$ (c) $\delta = 0.12$

Figure 5.10: From top to bottom: contours of potential φ, vorticity ω, log-density θ perturbations, and the underlying basic state log-density gradient Θ' profiles with the convectively unstable region highlighted. Ion viscosity and particle diffusivity are fixed at $D_n = 0.01$, $\mu = 0.1$, width ratio δ decreases from left to right.

5.5 Discussion

In this chapter we have studied the linear stability of a simple two-region model of interchange motions in the plasma edge of magnetic confinement devices. We have investigated the onset of instability as a function of particle diffusivity, ion viscosity, and the ratio of the widths of the two regions.

Perhaps unsurprisingly, we found that decreasing the values of diffusion parameters D_n and μ lowers the critical density difference at the onset of instability. As seen in Figures 5.4c,d, the dependence of the critical wavenumber on the values of diffusion parameters is not straightforward, although, in general, decreasing D_n or μ leads to an increase in k_c. The structure of the most unstable mode is tied closely to the underlying basic state density gradient. In particular, the critical wavenumber appears to be representative of the extent of the convectively unstable part of the basic state: when the width of this region narrows, the critical wavelength becomes smaller. The nature of the basic state density gradient changes depending on D_n and μ, leading to two distinct types of behaviour at the onset of instability. In one of them the basic state is such that the domain is effectively split into two parts: a convectively unstable part and a convectively stable part; in the other, the domain is split into three parts, with the convectively unstable region sandwiched from both sides by convectively stable regions. The first case occurs when neither the ion viscosity, nor particle diffusivity, are too small. The critical mode is characterised by the convection cells and the density perturbation being largely confined to the convectively unstable core region, only slightly penetrating the stable SOL owing to diffusion — an example of such a mode is plotted in Figure 5.5b. In the second case — which occurs when either the ion viscosity, or particle diffusivity, or both, are sufficiently small — the critical mode is characterised by convection cells and density perturbation being localised to a thin region near the separatrix, sandwiched from both sides by convectively stable regions. Examples of such modes are seen in Figures 5.5c and 5.6c.

We have found that as the width ratio of the two regions δ is increased from unity the stability threshold quickly becomes independent of δ. On the other hand, decreasing δ from unity significantly affects both the onset of instability and the structure of the most unstable mode. Specifically, as δ is decreased, the system becomes increasingly more stable. This is expected, since in the limit of $\delta \to 0$ the basic state density gradient vanishes, and thus the necessary condition for instability cannot be satisfied.

The analysis included in this chapter opens up a number of avenues for further investigation. A natural extension of this work is to explore the implications of variation in the values of the diffusion coefficients between the core and SOL, i.e. extending the analysis of the idealised problem from Chapter 4 to the full two-region plasma problem. Another aspect worth investigating in the linear regime is the asymptotic behaviour of the system in the limit of vanishing diffusion, i.e. $D_n \to 0$, $\mu \to 0$. Since $D_n \sim \mu \sim T_e^{-3/2}$, this limit is potentially relevant for future fusion machines, which will operate at substantially higher temperatures than current devices. Numerical modelling of systems with very small diffusion coefficients is extremely challenging even in the case of simple fluid problems. It is thus of value to develop a firm analytical understanding of the properties of the system

in this limit. Finally, beyond the linear analysis, it is of interest to study the nonlinear evolution of the linear solutions described above in order to investigate whether the distinct behaviour at the onset of instability has consequences on the particle flux in the SOL when the system is driven to a turbulent state.

Chapter 6

Summary and future work

The quest for nuclear fusion is a worldwide enterprise, with tremendous challenges spanning the fields of physics, engineering, material science and many more. In particular, one of the challenges is to confine hot fusion plasma – by magnetic fields – so that fusion reactions can occur and the process can become self-sustaining. However, various plasma phenomena cause instabilities and confinement losses. The stability problem is most severe at the plasma edge, causing hot, dense filamentary structures to strike the material surfaces of the fusion device, thus potentially inflicting damage and shortening the lifetime of the device.

Understanding filamentary formation plays a vital role in the successful operation of future, more powerful fusion reactors, like ITER, which are perhaps mankind's best hope for sustainable clean energy. As the fusion power increases, so does the erosive potential of filaments. Furthermore, energy losses associated with the ejection of filaments inhibit fusion reactions in the core. Therefore, although the filament problem is just one component in a massive world wide project, it is an important one, as it compromises the viability of fusion as a sustainable energy source.

It is widely recognized that turbulence in the SOL is driven by interchange instability, due to pressure gradients and magnetic field curvature. Over the years, numerous interchange models, of various complexity, have been developed, which successfully capture several experimentally measured features of the midplane SOL plasma. Yet despite their acclaim and extensive use, the analysis of their fundamental stability characteristics is limited.

In this thesis we have studied the onset of instability in the interchange models of the plasma edge. In Chapter 1 we provided an introduction to the problem of filamentary transport in the scrape-off layer of plasma fusion devices. In Chapter 2 we described the fundamentals of plasma physics, and introduced a two-dimensional fluid model used to study the plasma dynamics in the scrape-off layer of tokamaks. The model equations are based on the Braginskii fluid equations under the assumptions of drift ordering and electrostatic plasma. The model also employs the commonly used slab geometry approximation, whereby the magnetic field is assumed constant and straight, with the effects of curvature reintroduced as effective gravitational terms.

In Chapter 3 we performed an extensive linear stability analysis of the model intro-

duced in Chapter 2, restricting our attention to the dynamics in the SOL only. We studied the linear instability in the system by solving a boundary value problem, thereby extending previous studies, which focused on a local analysis. Furthermore, we demonstrated that the governing plasma equations for the SOL can be viewed as describing a thermal convection problem with additional effects. The new features include a non-uniform basic state gradient, linear damping terms, and additional advective terms. We characterised the conditions at the onset of instability and performed an extensive parameter scan to describe how the stability threshold varies as a function of plasma parameters. Owing to the spatial dependence of the basic state gradient, it is impossible to extract an analytical expression for the marginal stability threshold; in general, the problem has to be tackled numerically. To make progress analytically, we constructed a reduced problem, which could be solved in exactly the same way as the classical Rayleigh-Bénard convection problem. Numerical results of the full problem were compared with an analytical solution of the reduced system, thus providing solid ground for the interpretation of the observed trends. Furthermore, we identified an approximate range in parameter space for which there is good quantitative agreement between the full and reduced systems. Additionally, we commented on the complex behaviour of the solutions to the full problem outside this region of agreement. In particular, we demonstrated that the radial structure of the solutions of the linear system can become highly localised, to the point of developing a boundary layer.

In Chapter 4, motivated by the possibility that the core and the scrape-off layer may have different diffusion properties, and exploiting the analogy between the equations governing plasma interchange dynamics and those of classical Rayleigh-Bénard convection, we considered the linear stability of two-dimensional, two-layer miscible convection. We focused specifically on the influence of three particular parameters: the ratio of the viscosities in the two layers, the ratio of the thermal diffusivities, and the ratio of the depths of the two layers. The key result is that, depending on the parameters of the problem, the most unstable mode can take one of three quite distinct forms: whole layer solutions, in which the eigenfunctions of the stream function and temperature extend over both layers of fluid; localised solutions, with the velocity cells or the temperature perturbation (or both) confined to just one of the layers; and segregated solutions, in which the fluid motion and temperature perturbation are confined to different fluid layers. It is conceivable that the distinct regimes will be characterised by different heat transport properties. In terms of the plasma problem this would translate to different properties of the particle flux in the SOL, with consequences for the resulting plasma-wall interaction. It would therefore be of interest to investigate whether the contrast in diffusion coefficients in the full two-region plasma problem can lead to similar behaviour.

In Chapter 5 we studied the linear stability of the plasma interchange model in a configuration encompassing both the core and the SOL. We investigated how varying the particle diffusivity and the ion viscosity affects the stability threshold and the structure of the critical mode. We found that decreasing the values of the diffusion parameters lowers the critical density difference at the onset of instability, thus leading to a more unstable

system. Furthermore, we identified two distinct regimes at the onset of instability: one where the critical modes span the entire core region, and even extend into the scrape-off layer; and the other where the critical modes are localised in a thin region at the separatrix. The emergence of these two regimes is linked to the nature of the underlying basic state density gradient. In the first — which occurs when neither the ion viscosity nor particle diffusivity are particularly small — the form of the basic state gradient results in the domain being divided into a convectively unstable region and a convectively stable region. The perturbations take the form of large cells whose radial extent, as well as poloidal wavelength, are comparable to the width of the unstable region. In the second regime, the basic state gradient splits the domain into three parts: a convectively unstable part in the vicinity of the separatrix, sandwiched from both ends by convectively stable regions. The second stable region appears when either the ion viscosity or the particle diffusivity are decreased below some critical values. The resulting drastic narrowing in the extent of the convectively unstable region leads to an increase in the critical wavenumber, which reflects a change to smaller cells localised near the separatrix.

There are plenty of opportunities for future work with this model both from a numerical and an analytical perspective. As mentioned in Section 5.5, it is of interest to investigate the asymptotic limit of vanishing diffusivity, which is relevant for more powerful future machines. To probe this limit, we envisage that it would be possible to construct a reduced system with constant coefficients — as in the case of the single region problem in Chapter 3, Section 3.3.3 — that is more amenable to thorough analysis.

Another aspect worth investigation in the linear limit is the relaxation of the Boussinessq assumption. While the impact of the Boussinesq approximation has been studied previously in the context of the nonlinear evolution of blobs (e.g. Angus and Umansky, 2014; Yu et al., 2006), we expect non-Boussinesq effects to enter the analysis even at the linear level, on account of the spatially dependent background plasma density profile.

Beyond the linear analysis, it is of interest to study the nonlinear evolution of the critical modes described in Chapter 5 at supercritical conditions. There are a number of questions open for investigation. For example: How do the properties of particle flux and turbulence vary as a function of supercriticality? Do the different regimes lead to different particle flux and turbulence properties, or is the underlying linear state irrelevant in strongly supercritical conditions, and instead does a universal scaling exist? How far above critical conditions do filaments emerge? How does the emergence of filaments affect the particle flux? How does the depth of penetration into the SOL depend on the driving? Nonlinear numerical work that will attempt to investigate some of these questions will be undertaken during the author's fellowship at the University of Leeds commencing in October 2019.

So far our analysis has been restricted to a two-field — density and vorticity — constant temperature model, in which instability is driven solely by the density gradient. In reality, the temperature varies significantly between the core and the SOL. Therefore, a natural extension of this work towards a more realistic model is to include the effects of temperature evolution, thereby introducing a second component contributing to the

instability. With the plasma density and the temperature diffusing at different rates, as well as complicated coupling between them, the resulting extended model is a complicated double-diffusive, two-layer convection problem.

Layered convective systems and double-diffusive convection are ubiquitous in planetary and astrophysical fluid dynamics. Studies of two-layer convection were originally motivated by its suggested occurrence in the Earth's mantle, and its applicability extends to other planetary and stellar cores, where the fluid interior can be segregated into layers with distinct characteristics. Similarly, examples of double-diffusive convection can be found in stellar cores, where buoyancy depends on both thermal and compositional gradients, or in the oceans, with competition between heat and salinity. Although much is known about layered convective systems, and double-diffusive convection separately, the two aspects have never been studied in conjunction. Thus making progress in this area is potentially of very high impact, with implications not only for plasma fusion physics, but also in astrophysical and geophysical fluid dynamics.

Appendix A

Plasma fluid equations

In this section we derive the two fluid plasma equations by taking moments of the Boltzmann equation. Recall the Boltzmann equation (2.18):

$$\frac{\partial f_\sigma}{\partial t} + (\boldsymbol{v} \cdot \nabla)\, f_\sigma + (\bar{\boldsymbol{a}} \cdot \nabla_v)\, f_\sigma = \mathcal{C}_\sigma\,(f)\,. \tag{A.1}$$

In the following, we suppress all ensemble-average over-bars for ease of notation. Since $\boldsymbol{x}$ and $\boldsymbol{v}$ are in independent quantities in phase space ($\boldsymbol{v} \cdot \nabla f = \nabla \cdot (\boldsymbol{v}\, f)$), and acceleration commutes with vector velocity derivative ($\boldsymbol{a} \cdot \nabla_v f = \nabla_v \cdot (\boldsymbol{a}\, f)$) Boltzmann equation (A.1) for species σ can be written as

$$\frac{\partial f_\sigma}{\partial t} + \nabla \cdot (\boldsymbol{v} f_\sigma) + \nabla_v \cdot (\boldsymbol{a} f_\sigma) = \mathcal{C}_\sigma(f) \tag{A.2}$$

0^{th} order moment Integrating (A.2) throughout the velocity space yields

$$\int \left[\frac{\partial f_\sigma}{\partial t} + \nabla \cdot (\boldsymbol{v} f_\sigma) + \nabla_v \cdot (\boldsymbol{a} f_\sigma)\right] \mathrm{d}\boldsymbol{v} = \int \mathcal{C}_\sigma(f)\, \mathrm{d}\boldsymbol{v} \tag{A.3}$$

$$\frac{\partial}{\partial t} \int f_\sigma \, \mathrm{d}\boldsymbol{v} + \nabla \cdot \int (\boldsymbol{v} f_\sigma)\, \mathrm{d}\boldsymbol{v} + \int \nabla_v \cdot (\boldsymbol{a} f_\sigma)\, \mathrm{d}\boldsymbol{v} = 0 \tag{A.4}$$

The velocity integral commutes with both the time and space derivatives on the left hand side because $\boldsymbol{x}$, $\boldsymbol{v}$, and t are independent variables. Applying Gauss' theorem on the third term on the left hand side gives a surface integral of f_σ on a surface of $v = \infty$. For a well–behaved distribution function $f_\sigma \to 0$ as $v \to \infty$, so this surface integral in velocity space vanishes. Using equations (2.27) and (2.28) as well as the constraint of collisional particle conservation (2.21), we obtain the species continuity equation

$$\frac{\partial n_\sigma}{\partial t} + \nabla \cdot (n_\sigma \boldsymbol{u}_\sigma) = 0. \tag{A.5}$$

1^{st} order moment Multiply (A.2) by $\boldsymbol{v}$ and integrate throughout the velocity space

$$\int \boldsymbol{v} \left[\frac{\partial f_\sigma}{\partial t} + \nabla \cdot (\boldsymbol{v} f_\sigma) + \nabla_v \cdot (\boldsymbol{a} f_\sigma)\right] \mathrm{d}\boldsymbol{v} = \int \boldsymbol{v} \mathcal{C}_\sigma(f)\, \mathrm{d}\boldsymbol{v} \tag{A.6}$$

Considering each term in turn, the first term on the left hand side gives

$$\int \boldsymbol{v}\frac{\partial f_\sigma}{\partial t}\,\mathrm{d}\boldsymbol{v} = \frac{\partial}{\partial t}\int \boldsymbol{v} f_\sigma\,\mathrm{d}\boldsymbol{v} = \frac{\partial}{\partial t}\left(n_\sigma \boldsymbol{u}_\sigma\right).$$

For the second term on the left hand side, let us write the velocity field as a sum of mean and fluctuating parts $\boldsymbol{v} = \boldsymbol{u}(\boldsymbol{x},t) + \boldsymbol{v}'(\boldsymbol{x},t)$, where $\boldsymbol{v}'(\boldsymbol{x},t)$ is the random part of a given velocity, so we have

$$\begin{aligned}\int \boldsymbol{v}\nabla\cdot(\boldsymbol{v}f_\sigma)\,\mathrm{d}\boldsymbol{v} &= \nabla\cdot\int \boldsymbol{v}\boldsymbol{v} f_\sigma\,\mathrm{d}\boldsymbol{v} = \nabla\cdot\int\left(\boldsymbol{v}'\boldsymbol{v}' + 2\boldsymbol{u}_\sigma\boldsymbol{v}' + \boldsymbol{u}_\sigma\boldsymbol{u}_\sigma\right) f_\sigma\,\mathrm{d}\boldsymbol{v}\\ &= \nabla\cdot\left(n_\sigma\boldsymbol{u}_\sigma\boldsymbol{u}_\sigma\right) + \nabla\cdot\int \boldsymbol{v}'\boldsymbol{v}' f_\sigma\,\mathrm{d}\boldsymbol{v}\\ &= \nabla\cdot\left(n_\sigma\boldsymbol{u}_\sigma\boldsymbol{u}_\sigma\right) + \frac{1}{m_\sigma}\boldsymbol{p}_\sigma.\end{aligned}$$

Here we've defined the pressure tensor, $\boldsymbol{p}_\sigma$,

$$\boldsymbol{p}_\sigma = m_\sigma\int \boldsymbol{v}'\boldsymbol{v}' f_\sigma\,\mathrm{d}\boldsymbol{v} \tag{A.7}$$

and note that the trace of the pressure tensor measures the ordinary (scalar) pressure

$$Np_\sigma \equiv \mathrm{Tr}(\boldsymbol{p}_\sigma) = m_\sigma\int v'v' f_\sigma\,\mathrm{d}\boldsymbol{v} \tag{A.8}$$

where N denotes the dimension of the velocity space.
The third term on the LHS:

$$\begin{aligned}\int \boldsymbol{v}\nabla_v\cdot(\boldsymbol{a}f_\sigma)\,\mathrm{d}\boldsymbol{v} &= \int \nabla_v\cdot(\boldsymbol{v}\boldsymbol{a}f_\sigma) - f_\sigma\boldsymbol{a}\nabla_v\cdot\boldsymbol{v}\,\mathrm{d}\boldsymbol{v} = -\int \boldsymbol{a}\,f_\sigma\,\mathrm{d}\boldsymbol{v}\\ &= -\int\frac{e_\sigma}{m_\sigma}\left(\boldsymbol{E}+\boldsymbol{v}\times\boldsymbol{B}\right)f_\sigma\,\mathrm{d}\boldsymbol{v} = -n_\sigma\frac{e_\sigma}{m_\sigma}\left(\boldsymbol{E}+\boldsymbol{u}_\sigma\times\boldsymbol{B}\right).\end{aligned}$$

Finally, the term on the right hand side of the equation gives

$$\int \boldsymbol{v}\mathcal{C}_\sigma(f)\,\mathrm{d}\boldsymbol{v} = \int \boldsymbol{v}\mathcal{C}_{\sigma\sigma}(f_\sigma)\,\mathrm{d}\boldsymbol{v} + \int \boldsymbol{v}\mathcal{C}_{\sigma\alpha}(f_\alpha)\,\mathrm{d}\boldsymbol{v} = \frac{1}{m_\sigma}\boldsymbol{F}_\sigma,$$

where the integral involving $\mathcal{C}_{\sigma\sigma}$ vanishes by (2.22) and $\boldsymbol{F}_\sigma$ is the net frictional drag force due to collisions of species σ with other species.

Collecting all the terms together, we obtain the momentum equation:

$$m_\sigma\left[\frac{\partial}{\partial t}\left(n_\sigma\boldsymbol{u}_\sigma\right) + \nabla\cdot\left(n_\sigma\boldsymbol{u}_\sigma\boldsymbol{u}_\sigma\right)\right] = e_\sigma n_\sigma\left(\boldsymbol{E}+\boldsymbol{u}_\sigma\times\boldsymbol{B}\right) - \nabla\cdot\boldsymbol{p}_\sigma + \boldsymbol{F}_\sigma. \tag{A.9}$$

2^{nd} order moment Multiply (A.2) by $\frac{1}{2}m_\sigma v^2$ and integrate throughout the velocity space:

$$\int\frac{m_\sigma v^2}{2}\left[\frac{\partial f_\sigma}{\partial t} + \nabla\cdot(\boldsymbol{v}f_\sigma) + \nabla_v\cdot(\boldsymbol{a}f_\sigma)\right]\mathrm{d}\boldsymbol{v} = \int\frac{m_\sigma v^2}{2}\mathcal{C}_\sigma(f)\,\mathrm{d}\boldsymbol{v}. \tag{A.10}$$

Evaluating each term in turn, the first term yields

$$\begin{aligned}\int \frac{m_\sigma v^2}{2}\frac{\partial f_\sigma}{\partial t}\,\mathrm{d}\boldsymbol{v} &= \int \frac{m_\sigma v^2}{2} f_\sigma\,\mathrm{d}\boldsymbol{v} = \frac{\partial}{\partial t}\int \frac{m_\sigma}{2}(\boldsymbol{u}_\sigma+\boldsymbol{v}')\cdot(\boldsymbol{u}_\sigma+\boldsymbol{v}')f_\sigma\,\mathrm{d}\boldsymbol{v} = \\ &= \frac{\partial}{\partial t}\int \frac{m_\sigma}{2}(u_\sigma^2+2\boldsymbol{u}_\sigma\cdot\boldsymbol{v}'+v'^2)f_\sigma\,\mathrm{d}\boldsymbol{v} = \\ &= \frac{\partial}{\partial t}\left(\frac{1}{2}m_\sigma n_\sigma u_\sigma^2\right)+\frac{\partial}{\partial t}\left(\frac{N}{2}p_\sigma\right),\end{aligned}$$

where we have utilised the definition of scalar pressure (A.8). The second term reads

$$\int \frac{m_\sigma v^2}{2}\nabla\cdot(\boldsymbol{v}f_\sigma)\,\mathrm{d}\boldsymbol{v} = \nabla\cdot\int \frac{m_\sigma v^2}{2}\boldsymbol{v}f_\sigma\,\mathrm{d}\boldsymbol{v} = \nabla\cdot\boldsymbol{Q}_\sigma,$$

where $\boldsymbol{Q}_\sigma$ is the energy flux as defined in (2.30). Separating velocity field into mean and fluctuating parts

$$\begin{aligned}\boldsymbol{Q}_\sigma &= \int \frac{1}{2}m_\sigma v^2\boldsymbol{v}f_\sigma\,\mathrm{d}\boldsymbol{v} = \int \frac{1}{2}m_\sigma(u_\sigma^2+2\boldsymbol{u}_\sigma\cdot\boldsymbol{v}'+v'^2)(\boldsymbol{u}_\sigma+\boldsymbol{v}')f_\sigma\,\mathrm{d}\boldsymbol{v} = \\ &= \int \frac{1}{2}m_\sigma\left(u_\sigma^2\boldsymbol{u}_\sigma+u_\sigma^2\boldsymbol{v}'+2(\boldsymbol{u}_\sigma\cdot\boldsymbol{v}')\boldsymbol{u}_\sigma+2(\boldsymbol{u}_\sigma\cdot\boldsymbol{v}')\boldsymbol{v}'+v'^2\boldsymbol{u}_\sigma+v'^2\boldsymbol{v}'\right)f_\sigma\,\mathrm{d}\boldsymbol{v} = \\ &= \frac{1}{2}m_\sigma n_\sigma u_\sigma^2\boldsymbol{u}_\sigma+\int m_\sigma(\boldsymbol{u}_\sigma\cdot\boldsymbol{v}')\boldsymbol{v}'f_\sigma\,\mathrm{d}\boldsymbol{v}+\frac{N}{2}p_\sigma\boldsymbol{u}_\sigma+\boldsymbol{q}_\sigma,\end{aligned}$$

with $\boldsymbol{q}_\sigma$ defined as

$$\boldsymbol{q}_\sigma = \int \frac{1}{2}m_\sigma v'^2\boldsymbol{v}'f_\sigma\,\mathrm{d}\boldsymbol{v}.$$

Note also that

$$\int m_\sigma(\boldsymbol{u}_\sigma\cdot\boldsymbol{v}')\boldsymbol{v}'f_\sigma\,\mathrm{d}\boldsymbol{v} = \boldsymbol{u}_\sigma\cdot\int m_\sigma\boldsymbol{v}'\boldsymbol{v}'f_\sigma\,\mathrm{d}\boldsymbol{v} = \boldsymbol{u}_\sigma\cdot\boldsymbol{p}_\sigma.$$

The third term yields

$$\begin{aligned}\int \frac{m_\sigma v^2}{2}\nabla_v\cdot(\boldsymbol{a}f_\sigma)\,\mathrm{d}\boldsymbol{v} &= \int \nabla_v\cdot\left(\frac{m_\sigma v^2}{2}\boldsymbol{a}f_\sigma\right)-\boldsymbol{a}f_\sigma\cdot\nabla_v\left(\frac{m_\sigma v^2}{2}\right)\mathrm{d}\boldsymbol{v} = \\ &= -\int e_\sigma\left(\boldsymbol{E}+\boldsymbol{v}\times\boldsymbol{B}\right)\cdot\nabla_v\left(\frac{v^2}{2}\right)f_\sigma\,\mathrm{d}\boldsymbol{v} = -e_\sigma\int \boldsymbol{E}\cdot\boldsymbol{v}f_\sigma\,\mathrm{d}\boldsymbol{v} \\ &= -e_\sigma n_\sigma\boldsymbol{u}_\sigma\cdot\boldsymbol{E}.\end{aligned}$$

And finally, the term on the right hand side gives

$$\begin{aligned}\int \frac{m_\sigma v^2}{2}\mathcal{C}_\sigma(f)\,\mathrm{d}\boldsymbol{v} &= \frac{m_\sigma u_\sigma^2}{2}\int \mathcal{C}_{\sigma\alpha}(f_\sigma)\,\mathrm{d}\boldsymbol{v}+\boldsymbol{u}_\sigma\cdot\int m_\sigma\boldsymbol{v}'\mathcal{C}_{\sigma\alpha}(f_\sigma)\,\mathrm{d}\boldsymbol{v}+\int \frac{m_\sigma v'^2}{2}\mathcal{C}_{\sigma\alpha}(f_\sigma)\,\mathrm{d}\boldsymbol{v} \\ &= \boldsymbol{u}_\sigma\cdot\boldsymbol{F}+\mathcal{W}_\sigma,\end{aligned}$$

where $\mathcal{W}_\sigma$ denotes the kinetic energy change due to collisions (frictional heating). Collecting above results, we obtain the energy conservation equation:

$$\frac{\partial}{\partial t}\left(\frac{Np_\sigma}{2}+\frac{1}{2}m_\sigma n_\sigma u_\sigma^2\right)+\nabla\cdot\left(\frac{1}{2}m_\sigma n_\sigma u_\sigma^2\boldsymbol{u}_\sigma+\boldsymbol{u}_\sigma\cdot\boldsymbol{p}_\sigma+\frac{N}{2}p_\sigma\boldsymbol{u}_\sigma+\boldsymbol{q}_\sigma\right)-e_\sigma n_\sigma\boldsymbol{u}_\sigma\cdot\boldsymbol{E}= \boldsymbol{u}_\sigma\cdot\boldsymbol{F}+\mathcal{W}_\sigma \quad \text{(A.11)}$$

Plasma fluid equations comprise of the three lowest moments of the Boltzmann equation, which respectively give equations of continuity, momentum and heat balance.

$$\frac{\partial n_\sigma}{\partial t}+\nabla\cdot(n_\sigma\boldsymbol{u}_\sigma)=0, \quad \text{(A.12)}$$

$$m_\sigma\left(\frac{\partial}{\partial t}(n_\sigma\boldsymbol{u}_\sigma)+\nabla\cdot(n_\sigma\boldsymbol{u}_\sigma\boldsymbol{u}_\sigma)\right)=e_\sigma n_\sigma\left(\boldsymbol{E}+\boldsymbol{u}_\sigma\times\boldsymbol{B}\right)-\nabla\cdot\boldsymbol{p}_\sigma+\boldsymbol{F}_\sigma, \quad \text{(A.13)}$$

$$\frac{\partial}{\partial t}\left(\frac{Np_\sigma}{2}+\frac{1}{2}m_\sigma n_\sigma u_\sigma^2\right)+\nabla\cdot\left(\frac{1}{2}m_\sigma n_\sigma u_\sigma^2\boldsymbol{u}_\sigma+\boldsymbol{u}_\sigma\cdot\boldsymbol{p}_\sigma+\frac{N}{2}p_\sigma\boldsymbol{u}_\sigma+\boldsymbol{q}_\sigma\right) = e_\sigma n_\sigma\boldsymbol{u}_\sigma\cdot\boldsymbol{E}+\boldsymbol{u}_\sigma\cdot\boldsymbol{F}+\mathcal{W}_\sigma. \quad \text{(A.14)}$$

A.1 Non-conservative form

Splitting the pressure tensor into a sum of the ordinary pressure and the generalised pressure tensor, $\boldsymbol{\pi_\sigma}$,

$$\boldsymbol{p}_\sigma=p_\sigma\boldsymbol{I}+\boldsymbol{\pi_\sigma},$$

where $\boldsymbol{I}$ is the identity tensor, equations (A.12)—(A.14) can be rewritten in their non-conservative form:

$$\frac{\partial n_\sigma}{\partial t}+\nabla\cdot(n_\sigma\boldsymbol{u}_\sigma)=0, \quad \text{(A.15)}$$

$$m_\sigma n_\sigma\frac{\mathrm{d}\boldsymbol{u}_\sigma}{\mathrm{d}t}=-\nabla p_\sigma-\nabla\cdot\boldsymbol{\pi_\sigma}+e_\sigma n_\sigma\left(\boldsymbol{E}+\boldsymbol{u}_\sigma\times\boldsymbol{B}\right)+\boldsymbol{F}_\sigma, \quad \text{(A.16)}$$

$$\frac{N}{2}\frac{\mathrm{d}p_\sigma}{\mathrm{d}t}+\left(\frac{N+2}{2}\right)p_\sigma\nabla\cdot u_\sigma+\boldsymbol{\pi_\sigma}:\nabla\boldsymbol{u}_\sigma+\nabla\cdot\boldsymbol{q_\sigma}=\mathcal{W}_\sigma. \quad \text{(A.17)}$$

Here, $\frac{\mathrm{d}}{\mathrm{d}t}$ denotes the material derivative and

$$\boldsymbol{\pi_\sigma}:\nabla\boldsymbol{u}_\sigma\equiv(\pi_\sigma)_{ij}\frac{\partial}{\partial x_i}(u_\sigma)_j\,. \quad \text{(A.18)}$$

Appendix B

Shear-Alfvén Law

Consider the plasma fluid momentum equation for the centre of mass velocity V:

$$\boldsymbol{f} = \rho \frac{\mathrm{d}\boldsymbol{V}}{\mathrm{d}t} + \boldsymbol{\nabla} \cdot \Pi = -\boldsymbol{\nabla} P + \boldsymbol{J} \times \boldsymbol{B}. \tag{B.1}$$

We eliminate the pressure gradient by taking the curl and then consider the parallel component of the resulting equation ($\boldsymbol{B} \cdot \boldsymbol{\nabla} \times$)

$$\boldsymbol{B} \cdot \boldsymbol{\nabla} \times \boldsymbol{f} = \boldsymbol{B} \cdot \boldsymbol{\nabla} \times (\boldsymbol{J} \times \boldsymbol{B}) \,. \tag{B.2}$$

We then introduce the curvature term $\boldsymbol{\kappa}$

$$\boldsymbol{\kappa} = \boldsymbol{b} \cdot \boldsymbol{\nabla} \boldsymbol{b} = \underbrace{\frac{1}{2} \nabla |\boldsymbol{b}|^2}_{=0, \text{ as } |\boldsymbol{b}|=1} - \boldsymbol{b} \times \boldsymbol{\nabla} \times \boldsymbol{b} = -\boldsymbol{b} \times \boldsymbol{\nabla} \times \boldsymbol{b}. \tag{B.3}$$

Note the following identities:

$$\begin{aligned} \boldsymbol{b} \times \boldsymbol{\nabla} \times \boldsymbol{b} &= \frac{\boldsymbol{B}}{B} \times \left(\boldsymbol{\nabla} \times \frac{\boldsymbol{B}}{B} \right) = \frac{\boldsymbol{B}}{B} \times \left(\frac{1}{B} \boldsymbol{\nabla} \times \boldsymbol{B} - \frac{\boldsymbol{\nabla} B}{B^2} \times \boldsymbol{B} \right) \\ &= \frac{\boldsymbol{B} \times (\boldsymbol{\nabla} \times \boldsymbol{B})}{B^2} - \frac{\boldsymbol{B} \times (\boldsymbol{\nabla} B \times \boldsymbol{B})}{B^3}, \end{aligned} \tag{B.4}$$

$$\begin{aligned} \boldsymbol{B} \times (\boldsymbol{\nabla} B \times \boldsymbol{B}) &= \boldsymbol{\nabla} B \, (\boldsymbol{B} \cdot \boldsymbol{B}) - \boldsymbol{B} \, (\boldsymbol{B} \cdot \boldsymbol{\nabla} \boldsymbol{B}) \\ &= B^2 \boldsymbol{\nabla} B - B^2 \boldsymbol{\nabla}_{\parallel} B = B^2 \boldsymbol{\nabla}_{\perp} B. \end{aligned} \tag{B.5}$$

Substituting (B.5) and Ampere's law, $\boldsymbol{\nabla} \times \boldsymbol{B} = \mu_0 \boldsymbol{J}$, into (B.4), the curvature (B.3) becomes

$$\boldsymbol{\kappa} = \frac{\mu_0 \boldsymbol{J} \times \boldsymbol{B}}{B^2} + \frac{\boldsymbol{\nabla}_{\perp} B}{B}. \tag{B.6}$$

Now consider the right hand side of (B.2):

$$\begin{aligned}
\boldsymbol{B}\cdot\boldsymbol{\nabla}\times(\boldsymbol{J}\times\boldsymbol{B}) &= \boldsymbol{\nabla}\cdot((\boldsymbol{J}\times\boldsymbol{B})\times\boldsymbol{B}) + \underbrace{(\boldsymbol{J}\times\boldsymbol{B})\cdot\boldsymbol{\nabla}\times\boldsymbol{B}}_{=0,\text{ as }\boldsymbol{\nabla}\times\boldsymbol{B}=\mu_0\boldsymbol{J}} \\
&= \boldsymbol{\nabla}\cdot\left(-\boldsymbol{J}_\perp B^2\right) \qquad\qquad \left[\boldsymbol{J}_\perp = \frac{\boldsymbol{B}\times(\boldsymbol{J}\times\boldsymbol{B})}{B^2}\right] \\
&= -\boldsymbol{J}_\perp\cdot\boldsymbol{\nabla}B^2 - B^2\boldsymbol{\nabla}\cdot\boldsymbol{J}_\perp \\
&= -\frac{1}{B^2}\boldsymbol{B}\times(\boldsymbol{J}\times\boldsymbol{B})\cdot\boldsymbol{\nabla}_\perp B^2 - B^2\left(\underbrace{\boldsymbol{\nabla}\cdot\boldsymbol{J}}_{=0} - \boldsymbol{\nabla}\cdot\left(J_\parallel\boldsymbol{b}\right)\right) \\
&= -\boldsymbol{B}\times\left(\frac{\boldsymbol{\kappa}}{\mu_0} - \frac{\boldsymbol{\nabla}_\perp B}{\mu_0 B}\right)\cdot\boldsymbol{\nabla}_\perp B^2 + B^2\boldsymbol{\nabla}\cdot\left(J_\parallel\frac{\boldsymbol{B}}{B}\right) \\
&= -\boldsymbol{B}\times\frac{\boldsymbol{\kappa}}{\mu_0}\cdot\boldsymbol{\nabla}_\perp B^2 + \underbrace{\boldsymbol{B}\times\frac{\boldsymbol{\nabla}_\perp B}{\mu_0 B}\cdot\boldsymbol{\nabla}_\perp B^2}_{=0} + B^2\boldsymbol{B}\cdot\boldsymbol{\nabla}\left(\frac{J_\parallel}{B}\right). \qquad \text{(B.7)}
\end{aligned}$$

Hence, (B.2) becomes

$$\boldsymbol{B}\cdot\boldsymbol{\nabla}\times\boldsymbol{f} = B^2\boldsymbol{B}\cdot\boldsymbol{\nabla}\left(\frac{J_\parallel}{B}\right) - \boldsymbol{B}\times\frac{\boldsymbol{\kappa}}{\mu_0}\cdot\boldsymbol{\nabla}_\perp B^2. \qquad \text{(B.8)}$$

Note from (B.1) that $\boldsymbol{J}\times\boldsymbol{B} = \boldsymbol{\nabla}P + \boldsymbol{f}$. Using this in (B.6) we obtain

$$\boldsymbol{\kappa} = \mu_0\frac{\boldsymbol{\nabla}P + \boldsymbol{f}}{B^2} + \frac{\boldsymbol{\nabla}_\perp B}{B}. \qquad \text{(B.9)}$$

Multiplying through by B^2 we obtain

$$\boldsymbol{\nabla}_\perp B^2 = 2B^2\boldsymbol{\kappa} - 2\mu_0\left(\boldsymbol{\nabla}P + \boldsymbol{f}\right). \qquad \text{(B.10)}$$

Finally, on substituting (B.10) into (B.8) we obtain the shear-Alfvén law:

$$\boldsymbol{B}\cdot\left(\boldsymbol{\nabla}\times\boldsymbol{f} - 2\boldsymbol{\kappa}\times\boldsymbol{f}\right) = B^2\boldsymbol{B}\cdot\boldsymbol{\nabla}\left(\frac{J_\parallel}{B}\right) + 2\boldsymbol{B}\times\boldsymbol{\kappa}\cdot\boldsymbol{\nabla}P. \qquad \text{(B.11)}$$

References

Angus, J. R. and Krasheninnikov, S. I. (2014). Inviscid evolution of large amplitude filaments in a uniform gravity field. *Physics of Plasmas*, 21(11):112504.

Angus, J. R., Krasheninnikov, S. I., and Umansky, M. V. (2012). Effects of parallel electron dynamics on plasma blob transport. *Physics of Plasmas*, 19(8):082312.

Angus, J. R. and Umansky, M. V. (2014). Modeling of large amplitude plasma blobs in three-dimensions. *Physics of Plasmas*, 21(1):012514.

Antar, G. Y., Counsell, G., Yu, Y., Labombard, B., and Devynck, P. (2003). Universality of intermittent convective transport in the scrape-off layer of magnetically confined devices. *Physics of Plasmas*, 10(2):419–428.

Aydemir, A. Y. (2005). Convective transport in the scrape-off layer of tokamaks. *Physics of Plasmas*, 12(6):062503.

Bellan, P. M. (2008). *Fundamentals of Plasma Physics*. Cambridge University Press.

Berning, M. and Spatschek, K. H. (2000). Bifurcations and transport barriers in the resistive-g paradigm. *Physical Review E*, 62(1):1162.

Bian, N., Benkadda, S., Paulsen, J. V., and Garcia, O. E. (2003). Blobs and front propagation in the scrape-off layer of magnetic confinement devices. *Physics of Plasmas*, 10(3):671–676.

Bisai, N., Das, A., Deshpande, S., Jha, R., Kaw, P., Sen, A., and Singh, R. (2004). Simulation of plasma transport by coherent structures in scrape-off-layer tokamak plasmas. *Physics of Plasmas*, 11(8):4018–4024.

Bisai, N., Das, A., Deshpande, S., Jha, R., Kaw, P., Sen, A., and Singh, R. (2005). Edge and scrape-off layer tokamak plasma turbulence simulation using two-field fluid model. *Physics of Plasmas*, 12(7):072520.

Booker, J. R. (1976). Thermal convection with strongly temperature-dependent viscosity. *Journal of Fluid Mechanics*, 76(4):741–754.

Braginskii, S. I. (1965). Transport processes in a plasma. *Reviews of Plasma Physics*, 1:205.

Busse, F. H. (1981). On the aspect ratios of two-layer mantle convection. *Physics of the Earth and Planetary Interiors*, 24(4):320–324.

Chandrasekhar, S. (1981). *Hydrodynamic and Hydromagnetic Stability*. Dover Publications, Inc., 3^{rd} edition.

Chen, F. F. (1984). *Introduction to Plasma Physics and Controlled Fusion*, volume 1. Plenum Press, New York, US, 2nd edition.

D'Ippolito, D. A., Myra, J. R., and Krasheninnikov, S. I. (2002). Cross-field blob transport in tokamak scrape-off-layer plasmas. *Physics of Plasmas*, 9(1):222–233.

D'Ippolito, D. A., Myra, J. R., and Zweben, S. J. (2011). Convective transport by intermittent blob-filaments: comparison of theory and experiment. *Physics of Plasmas*, 18(6):060501.

Diwakar, S. V., Tiwari, S., Das, S. K., and Sundararajan, T. (2014). Stability and resonant wave interactions of confined two-layer Rayleigh–Bénard systems. *Journal of Fluid Mechanics*, 754:415–455.

Drake, J. F. and Antonsen Jr, T. M. (1984). Nonlinear reduced fluid equations for toroidal plasmas. *Physics of Fluids*, 27(4):898–908.

Easy, L., Militello, F., Omotani, J., Dudson, B., Havlíčková, E., Tamain, P., Naulin, V., and Nielsen, A. H. (2014). Three dimensional simulations of plasma filaments in the scrape off layer: A comparison with models of reduced dimensionality. *Physics of Plasmas*, 21(12):122515.

Easy, L., Militello, F., Omotani, J., Walkden, N., and Dudson, B. (2016). Investigation of the effect of resistivity on scrape off layer filaments using three-dimensional simulations. *Physics of Plasmas*, 23(1):012512.

EUROfusion (2011). Tokamak principle. https://www.euro-fusion.org.

Fitzpatrick, R. (2014). *Plasma Physics: An Introduction*. CRC Press.

Fundamenski, W., Garcia, O. E., Naulin, V., Pitts, R. A., Nielsen, A. H., Rasmussen, J. J., Horacek, J., Graves, J. P., et al. (2007). Dissipative processes in interchange driven scrape-off layer turbulence. *Nuclear Fusion*, 47(5):417.

Garcia, O. E. (2001). Two-field transport models for magnetized plasmas. *Journal of Plasma Physics*, 65(2):81–96.

Garcia, O. E., Bian, N. H., and Fundamenski, W. (2006a). Radial interchange motions of plasma filaments. *Physics of Plasmas*, 13(8):082309.

Garcia, O. E., Bian, N. H., Naulin, V., Nielsen, A. H., and Rasmussen, J. J. (2005a). Mechanism and scaling for convection of isolated structures in nonuniformly magnetized plasmas. *Physics of Plasmas*, 12(9):090701.

Garcia, O. E., Bian, N. H., Naulin, V., Nielsen, A. H., and Rasmussen, J. J. (2006b). Two-dimensional convection and interchange motions in fluids and magnetized plasmas. *Physica Scripta*, 2006(T122):104.

Garcia, O. E., Horacek, J., Pitts, R., Nielsen, A. H., Fundamenski, W., Naulin, V., and Rasmussen, J. J. (2007). Fluctuations and transport in the tcv scrape-off layer. *Nuclear Fusion*, 47(7):667.

Garcia, O. E., Horacek, J., Pitts, R. A., Nielsen, A. H., Fundamenski, W., Graves, J. P., Naulin, V., and Rasmussen, J. J. (2005b). Interchange turbulence in the TCV scrape-off layer. *Plasma Physics and Controlled Fusion*, 48(1):L1–L10.

Garcia, O. E., Naulin, V., Nielsen, A. H., and Rasmussen, J. J. (2004). Computations of intermittent transport in scrape-off layer plasmas. *Physical Review Letters*, 92(16):165003.

Garcia, O. E., Naulin, V., Nielsen, A. H., and Rasmussen, J. J. (2005c). Turbulence and intermittent transport at the boundary of magnetized plasmas. *Physics of Plasmas*, 12(6):062309.

Garcia, O. E., Naulin, V., Nielsen, A. H., and Rasmussen, J. J. (2006c). Turbulence simulations of blob formation and radial propagation in toroidally magnetized plasmas. *Physica Scripta*, T122:89–103.

Ghendrih, P., Sarazin, Y., Attuel, G., Benkadda, S., Beyer, P., Darmet, G., Falchetto, G., Figarella, C., Garbet, X., Grandgirard, V., et al. (2005). Statistical analysis of turbulent front propagation in the scrape-off-layer. *Journal of Nuclear Materials*, 337:347–351.

Ghendrih, P., Sarazin, Y., Attuel, G., Benkadda, S., Beyer, P., Falchetto, G., Figarella, C., Garbet, X., Grandgirard, V., and Ottaviani, M. (2003). Theoretical analysis of the influence of external biasing on long range turbulent transport in the scrape-off layer. *Nuclear Fusion*, 43(10):1013.

Goldston, R. J. (1984). Energy confinement scaling in tokamaks: some implications of recent experiments with ohmic and strong auxiliary heating. *Plasma Physics and Controlled Fusion*, 26(1A):87.

Goldston, R. J. and Rutherford, P. H. (1995). *Introduction to Plasma Physics*. CRC Press.

Hazeltine, R. D., Kotschenreuther, M., and Morrison, P. J. (1985). A four-field model for tokamak plasma dynamics. *Physics of Fluids*, 28(8):2466.

Hazeltine, R. D. and Meiss, J. D. (2003). *Plasma Confinement*. Courier Corporation.

Hazeltine, R. D. and Waelbroeck, F. L. (2004). *The Framework of Plasma Physics*. Westview.

Hinton, F. L. and Horton Jr, C. W. (1971). Amplitude limitation of a collisional drift wave instability. *Physics of Fluids*, 14(1):116–123.

Huba, J. D. (2006). NRL plasma formulary. Technical report, Naval Research Laboratory Washington, DC.

Hurlburt, N. E., Toomre, J., and Massaguer, J. M. (1986). Nonlinear compressible convection penetrating into stable layers and producing internal gravity waves. *The Astrophysical Journal*, 311:563–577.

Krasheninnikov, S. I. (2001). On scrape off layer plasma transport. *Physical Letters A*, 283(5):368–370.

Krasheninnikov, S. I., D'Ippolito, D. A., and Myra, J. R. (2008). Recent theoretical progress in understanding coherent structures in edge and SOL turbulence. *Journal of Plasma Physics*, 74(5):679.

Le Bars, M. and Davaille, A. (2002). Stability of thermal convection in two superimposed miscible viscous fluids. *Journal of Fluid Mechanics*, 471:339–363.

Madsen, J., Naulin, V., Nielsen, A. H., and Rasmussen, J. J. (2016). Collisional transport across the magnetic field in drift-fluid models. *Physics of Plasmas*, 23(3):032306.

Maqueda, R. J., Stotler, D. P., Zweben, S. J., and the NSTX Team (2011). Intermittency in the scrape-off layer of the National Spherical Torus Experiment during H-mode confinement. *Journal of Nuclear Materials*, 415(1):S459–S462.

Mendes, R. V. and Bizarro, J. P. (2017). Analytical study of growth estimates, control of fluctuations, and conservative structures in a two-field model of the scrape-off layer. *Physics of Plasmas*, 24(1):012303.

Militello, F., Dudson, B., Easy, L., Kirk, A., and Naylor, P. (2017). On the interaction of scrape off layer filaments. *Plasma Physics and Controlled Fusion*, 59(12):125013.

Militello, F., Fundamenski, W., Naulin, V., and Nielsen, A. H. (2012). Simulations of edge and scrape off layer turbulence in Mega Ampere Spherical Tokamak plasmas. *Plasma Physics and Controlled Fusion*, 54(9):095011.

Militello, F., Tamain, P., Fundamenski, W., Kirk, A., Naulin, V., Nielsen, A. H., et al. (2013). Experimental and numerical characterization of the turbulence in the scrape-off layer of MAST. *Plasma Physics and Controlled Fusion*, 55(2):025005.

Militello, F., Walkden, N. R., Farley, T., Gracias, W. A., Olsen, J., Riva, F., Easy, L., Fedorczak, N., Lupelli, I., Madsen, J., et al. (2016). Multi-code analysis of scrape-off layer filament dynamics in MAST. *Plasma Physics and Controlled Fusion*, 58(10):105002.

Myra, J. R., D'Ippolito, D. A., Stotler, D. P., Zweben, S. J., LeBlanc, B. P., Menard, J. E., Maqueda, R. J., and Boedo, J. (2006). Blob birth and transport in the tokamak edge plasma: Analysis of imaging data. *Physics of Plasmas*, 13(9).

Nield, D. A. (1968). The Rayleigh–Jeffreys problem with boundary slab of finite conductivity. *Journal of Fluid Mechanics*, 32(2):393–398.

Nielsen, A. H., Xu, G. S., Madsen, J., Naulin, V., Rasmussen, J. J., and Wan, B. N. (2015). Simulation of transition dynamics to high confinement in fusion plasmas. *Physical Letters A*, 379(47):3097–3101.

Olsen, J., Madsen, J., Nielsen, A. H., Rasmussen, J. J., and Naulin, V. (2016). Temperature dynamics and velocity scaling laws for interchange driven, warm ion plasma filaments. *Plasma Physics and Controlled Fusion*, 58(4):044011.

Omotani, J. T., Militello, F., Easy, L., and Walkden, N. R. (2015). The effects of shape and amplitude on the velocity of scrape-off layer filaments. *Plasma Physics and Controlled Fusion*, 58(1):014030.

Pellew, A. and Southwell, R. V. (1940). On maintained convective motion in a fluid heated from below. *Proc. R. Soc. Lond. A*, 176(966):312–343.

Rasenat, S., Busse, F. H., and Rehberg, I. (1989). A theoretical and experimental study of double-layer convection. *Journal of Fluid Mechanics*, 199:519–540.

Ricci, P., Halpern, F. D., Jolliet, S., Loizu, J., Mosetto, A., Fasoli, A., Furno, I., and Theiler, C. (2012). Simulation of plasma turbulence in scrape-off layer conditions: the gbs code, simulation results and code validation. *Plasma Physics and Controlled Fusion*, 54(12):124047.

Richter, F. M. and Johnson, C. E. (1974). Stability of a chemically layered mantle. *Journal of Geophysical Research*, 79(11):1635–1639.

Richter, F. M., Nataf, H.-C., and Daly, S. F. (1983). Heat transfer and horizontally averaged temperature of convection with large viscosity variations. *Journal of Fluid Mechanics*, 129:173–192.

Riva, F., Colin, C., Denis, J., Easy, L., Furno, I., Madsen, J., Militello, F., Naulin, V., Nielsen, A. H., Olsen, J. M. B., et al. (2016). Blob dynamics in the TORPEX experiment: a multi-code validation. *Plasma Physics and Controlled Fusion*, 58(4):044005.

Riva, F., Militello, F., Elmore, S., Omotani, J., Dudson, B. D., and Walkden, N. (2019). Three-dimensional plasma edge turbulence simulations of mast and comparison with experimental measurements. *Plasma Physics and Controlled Fusion*.

Russell, D. A., Myra, J. R., and D'Ippolito, D. A. (2009). Saturation mechanisms for edge turbulence. *Physics of Plasmas*, 16(12):122304.

Sarazin, Y. and Ghendrih, P. (1998). Intermittent particle transport in two-dimensional edge turbulence. *Physics of Plasmas*, 5(12):4214–4228.

Saslaw, W. C. and Schwarzschild, M. (1965). Overshooting from stellar convective cores. *The Astrophysical Journal*, 142:1468.

Simakov, A. N. and Catto, P. J. (2003). Drift-ordered fluid equations for field-aligned modes in low-β collisional plasma with equilibrium pressure pedestals. *Physics of Plasmas*, 10(12):4744–4757.

Stoer, J. and Bulirsch, R. (2013). *Introduction to Numerical Analysis*, volume 12. Springer Science & Business Media.

Tamain, P., Ghendrih, P., Tsitrone, E., Grandgirard, V., Garbet, X., Sarazin, Y., Serre, E., Ciraolo, G., and Chiavassa, G. (2010). TOKAM-3D: A 3d fluid code for transport and turbulence in the edge plasma of tokamaks. *Journal of Computational Physics*, 229(2):361–378.

Tritton, D. J. (2011). *Physical Fluid Dynamics*. Oxford University Press, 2^{nd} edition.

Umansky, M. V., Krasheninnikov, S. I., LaBombard, B., and Terry, J. L. (1998). Comments on particle and energy balance in the edge plasma of Alcator C-Mod. *Physics of Plasmas*, 5(9):3373–3376.

Veronis, G. (1963). Penetrative convection. *The Astrophysical Journal*, 137:641.

Walkden, N., Dudson, B., and Fishpool, G. (2013). Characterization of 3d filament dynamics in a mast sol flux tube geometry. *Plasma Physics and Controlled Fusion*, 55(10):105005.

Wilczynski, F. and Hughes, D. W. (2019). Stability of two-layer miscible convection. *Physical Review Fluids*, 4(10):103502.

Wilczynski, F., Hughes, D. W., Van Loo, S., Arter, W., and Militello, F. (2019). Stability of scrape-off layer plasma: A modified Rayleigh–Bénard problem. *Physics of Plasmas*, 26(2):022510.

Yan, N., Nielsen, A. H., Xu, G., Naulin, V., Rasmussen, J. J., Madsen, J., Wang, H., Liu, S., Zhang, W., Wang, L., et al. (2013). Statistical characterization of turbulence in the boundary plasma of east. *Plasma Physics and Controlled Fusion*, 55(11):115007.

Yu, G. Q., Krasheninnikov, S. I., and Guzdar, P. N. (2006). Two-dimensional modelling of blob dynamics in tokamak edge plasmas. *Physics of Plasmas*, 13(4):042508.

Zeiler, A., Drake, J. F., and Rogers, B. (1997). Nonlinear reduced braginskii equations with ion thermal dynamics in toroidal plasma. *Physics of Plasmas*, 4(6):2134–2138.

Zeren, R. W. and Reynolds, W. C. (1972). Thermal instabilities in two-fluid horizontal layers. *Journal of Fluid Mechanics*, 53(2):305–327.